Dynamic wetting of viscoelastic substrates

Mathieu Oléron

Université Paris Cité

Université Paris Cité

École doctorale n° 564 : Physique en île-de-France

Laboratoire Matière et Systèmes Complexes

Dynamic wetting of viscoelastic substrates

Par Mathieu Oléron

Thèse de doctorat de Physique

Dirigée par Laurent Limat

Présentée et soutenue publiquement le 10 février 2022

Devant un jury composé de :

M. Laurent Limat, CNRS/Université de Paris, Directeur de thèse
M. Thomas Salez, CNRS/Université de Bordeaux, Rapporteur
M. Robert Style, ETH Zürich, Rapporteur
Mme. Catherine Barentin, CNRS/Université Claude Bernard Lyon 1, Examinatrice
Mme. Cécile Monteux, CNRS/Université PSL, Présidente du jury
M. Matthieu Roché, CNRS/Université de Paris, Invité
M. Julien Dervaux, CNRS/Université de Paris, Invité

Contents

Remerciements

Ce manuscrit présente 3 ans de travaux réalisés au Laboraoire Matière et Systèmes Complexes. Evidemment, il ne résulte pas du travail d'un seul homme, mais est plutôt l'aboutissement d'une aventure collective. Ainsi, avant de rentrer dans le vif du sujet et de répéter allègrement les mots "viscoélastiques", "mouillage", "angle de contact" ou encore "ligne de contact", je tiens à remercier chaleureusement toutes les personnes ayant participé de près ou de loin à ce travail. Ce dernier ne serait pas le même sans vous.

Je tiens à remercier tous les membres du jury pour le temps qu'ils ont consacré à mon travail, la relecture de mon manuscrit et leurs remarques instructives. Merci donc à Thomas Salez, Robert Style, Cécile Monteux et Catherine Barentin.

Je remercie aussi tous mes collègues à MSC, et en particulier les permanents des salles 777 et 790: Adrian (merci pour ton agréable compagnie en salle de manip), Phillipe (un grand merci pour le prêt de la manip de "dip coating"), Michel et Christophe (toujours prêts à ramener un bon gâteau) ou encore Chi-Tuong (aka l'organisateur des évènements en 777). Je remercie aussi l'équipe de soutien à la recherche. Que ce soit pour un appui informatique (l'ordinateur de secours a sauvé la soutenance), administratif, en chimie (merci Véronique pour ta patience et tes conseils à l'égard des produits que j'utilisais) ou encore technique (merci à tous les membres de l'atelier qui m'ont aidé à concevoir les manips et ont partagé leur bonne humeur avec moi), ils ont toujours répondu présent. Un petit mot pour l'équipe "de la 513", qui aura bien voulu partager la "paillase PDMS" dont j'étais très demandeur, ainsi que pour Jean-Baptiste, qui aura effectué la dernière relecture de ce manuscrit en un temps record.

Je remercie aussi nos collaborateurs "hors MSC". Je pense notamment à Tetsuharu Narita (qui m'a initié à la synthèse d'hydrogels pendant mon stage), à Hélène Montes (qui a effectué les mesures de rhéologie de nos gels de silicone) ainsi qu'à Laurence Talini (qui a eu la patience et la gentillesse de m'accueillir au sein du SIMM pour un projet dont je ne parle pas ici).

La thèse n'est pas toujours un long fleuve tranquille, et pour ma part, les eaux se seront agitées avant même son commencement. Heureusement, j'ai pu compter sur quelques personnes qui m'auront permis de tenir la barre en fin de M2. Je tiens donc à remercier Frédéric Restagno: sans son soutien et ses conseils, la thèse ne se serait tout simplement pas faite. Je n'oublie pas non plus Manon et Marine, qui m'auront apporté leur soutien pendant cette période difficile.

Je tiens aussi à remercier Valentin Leroy et François Boulogne d'avoir bien voulu faire partie de mon comité de thèse. Ils auront su régler certains détails pour que la thèse se passe pour le mieux, et apporter à mon travail un regard extérieur très précieux (oui, je pense qu'on peut dire que les comités de thèse auront fait office de conférences pendant la pandémie).

Enfin, ces remerciements ne seraient pas complets sans mentionner ceux qui m'ont encadrés, guidés et ont fait en sorte que ce travail aboutisse. Laurent, ta porte est toujours restée ouverte malgré tes fonctions de directeur du laboratoire. Tu as aussi toujours été bienveillant et encourageant, pour tout cela je te remercie. Julien, tu as toujours été super encourageant, à coup de "trop cool" et "nickel" pour caractériser les données. Garde cette bonne humeur qui te caractérise. Je tiens aussi à remercier Menghua pour m'avoir patiemment encadré pendant mon stage. Et enfin Matthieu. C'est toi qui m'as véritablement encadré au quotidien. Tu as eu la lourde tâche d'affronter ma remise en question perpétuelle des données, et tu auras su m'inculquer le juste milieu dans la critique des données. Tu as géré les péripéties quotidiennes d'échantillons qui vieillissent, de projets qui sautent car

Covid et j'en passe... Mais plus encore, c'est surtout toi qui m'as fait confiance le premier en me prenant en stage puis en thèse par la suite. Pour ça je ne te remercierai jamais assez. Tous le trois, vous m'avez aidé à garder le cap sur le fleuve "Thèse", j'ai énormément appris à votre contact. Au moment où j'écris ces lignes, je ne sais pas encore de quoi l'avenir sera fait, mais je suis sûr que tout ce que vous m'avez appris me sera très utile. Je garde un très bon souvenir de ces trois ans passés à vos côtés.

Cette thèse aura aussi été l'occasion d'encadrer pour la première fois une stagiaire, ce qui aura été une expérience enrichissante. Je remercie donc Lisa, dont le travail sur les expériences de "dip coating" apparait sous forme d'ouverture dans ce manuscrit. Ça aura été un réel plaisir de travailler ensemble. Je pense évidemment aux autres stagiaires du groupe (Alicia, Grégoire, Marie, Dario, Louis, Camille) qui auront contribué à la bonne ambiance du groupe.

En parlant de bonne ambiance, je tiens évidemment à remercier mes amis de la "team 777", qui ont grandement contribué à rendre cette aventure agréable. Que ce soit pour les barbecues, les goûters (quand tout cela était permis bien sûr), les blagues toujours subtiles et délicates, ou encore la semaine exceptionnelle au ski !! Darius, Gabriel^2, Alice^2, Aina, Johann : merci ! Je n'oublie pas non plus "les anciens" de la salle (Rémy, Robin, Chuanyu, Julien, Amandine), "la relève" (Weiyuan, Ma, Geyu), ou encore les thésards "des bureaux d'à côté". Plus que de simples collègues, ces personnes auront su se montrer des amis précieux dans les moments difficiles de la thèse.

Je remercie par ailleurs mes amis "hors du labo" : Quentin, Aurélie, Manon, Marina, Marine, Vincent, Fabien, Théophile, Marion, Insa, Rayan (+ tout ceux que je vais oublier de citer, pardon d'avance!).

Je remercie aussi ma famille, pour qui il était parfois difficile de comprendre ce que je faisais avec "ma goutte d'eau". Sans rentrer dans les détails trop personnels, je me contenterai de dire qu'ils ont su m'apporter un soutien sans faille durant toute cette aventure, couronné par leur présence "en force" le jour J.

Arigato gozaimasu !!!

Résumé

Cette thèse étudie l'élastomouillage dynamique, c'est-à-dire le déplacement d'un liquide sur un substrat déformable. Un liquide dissipe son énergie motrice par viscosité lorsqu'il se déplace sur une surface solide. Cependant, les substrats viscoélastiques comme les gels de polymères dissipent aussi de l'énergie : l'interface liquide/vapeur tire sur le substrat ; la déformation qui en résulte dissipe de l'énergie lorsqu'elle suit le déplacement de la ligne de contact. Un modèle récent, basé sur la théorie de l'élasticité non linéaire, soutient que le rapport de ces deux sources de dissipation est un paramètre crucial du système. Plus ce rapport est grand, plus la dissipation dans le substrat est importante par rapport à celle dans le liquide. Cette thèse met en valeur le rôle clé de ce rapport de dissipation, jusque-là inexploré. Nous avons fait dévaler des gouttes sur des gels de silicone, ce qui permet d'étudier à la fois le mouvement d'avancée et de reculée du liquide. Le rapport des dissipations des systèmes choisis varie sur quatre ordres de grandeurs. La forme des gouttes dépend fortement de ce paramètre. Lorsque le liquide dissipe autant d'énergie que le solide, on retrouve des formes proches du cas où le substrat est rigide : la goutte forme un coin arrière à mesure que sa vitesse augmente. Les coins sont cependant plus arrondis que dans le cas rigide. Lorsque le solide dissipe beaucoup plus que le liquide, les gouttes sont plus allongées et ne présentent plus de coin. La mesure de la vitesse des gouttes en fonction de leur poids retrouve ces deux cas de figures. Dans le premier cas, la vitesse augmente linéairement avec le poids, comme si le substrat ne jouait pas de rôle. Dans le second cas, la vitesse augmente toujours avec le poids, mais cette fois-ci la rhéologie du solide régit la dynamique. Nous avons aussi mesuré les angles de contact entre la goutte et le substrat en fonction de la vitesse. Augmenter le rapport de dissipation modifie progressivement la relation entre l'angle et la vitesse. Lorsque ce dernier est faible, on retrouve une courbe proche de celle de Cox-Voinov, largement utilisée pour décrire le mouillage sur un substrat rigide. Mais lorsque celui-ci augmente, la courbe adopte une pente de plus en plus forte à basse vitesse, et des plateaux de plus en plus en plus marqués à haute vitesse (en valeur absolue). Ceci explique l'allongement des gouttes à mesure que le substrat dissipe de plus en plus. Le modèle susnommé, en excellent accord avec nos résultats, prédit cette « hystérèse molle ». Cette mesure plus locale complète l'interprétation des mesures de pesée. En effet, les propriétés viscoélastiques du substrat affectent la dynamique de la goutte même lorsque celle-ci dissipe autant dans le liquide que dans le substrat. Malgré de fortes ressemblances avec le cas rigide, où seul le liquide dissipe, une simple approche « comme si » le substrat ne dissipait pas ne suffit plus à décrire les données. Dans tous les cas, la goutte laisse des gouttes derrière elle au-delà d'une certaine vitesse - c'est l'instabilité de perlage. Nos expériences vérifient la tendance prédite par le modèle : le seuil d'instabilité décroît avec le rapport de dissipation à angle d'équilibre constant. Le présent travail apporte aussi un nouvel éclairage sur l'échelle à laquelle les gouttes en coin s'arrondissent. Les mesures sur des lames de verre suggèrent des échelles moléculaires. Or, la longueur élastocapillaire, taille caractéristique de la déformation au niveau de la ligne de contact, semble se coupler avec l'échelle moléculaire pour définir la courbure du coin dans nos systèmes : plus celle-ci est petite, plus le coin est « pointu ». Ceci explique pourquoi les coins sont plus arrondis quand le substrat est viscoélastique. Une étude plus poussée est nécessaire afin de comprendre en détail le rôle de la longueur élastocapillaire.

Mots-clés : mouillage, élasto-mouillage, viscoélasticité

Abstract

This work focuses on dynamical elastowetting, which means it investigates the motion of a liquid onto a deformable substrate. However, viscoelastic substrates such as polymeric gels also dissipate energy: the liquid/vapor interface pulls the substrate; the resulting wetting ridge dissipates energy when the contact line carries it along. Recent theoretical predictions use nonlinear elasticity and suggest that the ratio of these two dissipation sources rules the dynamics of elastowetting systems. The bigger the ratio, the more the substrate dissipates. This thesis probes the so far uncharted implications of this dissipation ratio. Drops slide onto inclined silicon gels, and the dissipation ratio spans four orders of magnitude. We then study both advancing and receding contact lines. This parameter sets the shape of the drops. When the viscoelastic solid dissipates as much energy as the viscous liquid, we observe shapes akin to the rigid case. The drop forms a corner at the rear - the faster, the sharper. We observe rounder corners than the case where the substrate is rigid though. When the viscoelastic solid dissipates much more energy than the viscous liquid, we observe longer and corner-free drops. The relation between the weight and the running speed of the drops confirms the stark difference between systems where the liquid dissipate as much as the solid and systems that mostly dissipate in the substrate. In the first case, the speed increases linearly with the weight, just like the rigid case. In the second case, the rheology of the substrate rules the dynamics. We also mesured the dynamic contact angles between the drop and its substrate. The dissipation ratio strongly modifies the relation between those two parameters. At low dissipation ratio, the curve and the Cox-Voinov relation, that well describes the rigid case, look alike. At high dissipation ratio, the curve steepens at low speed and exhibits two plateaus at large speed (in absolute value). Longer drops stem from this "S"-like curve, called soft hysteresis. The aforementioned model predicts this phenomenon and is in excellent agreement with our experimental data. Local measurements such as dynamic contact angles highlight subtle effects that weighing measurements miss. Viscoelasticity does impact the dynamic of the drop even when the dissipation ratio is close to unity. Despite strong similarities with the rigid case, simply neglecting the dissipation inside the liquid is inapropriate to describe our data. In any case, the drop leaves pearls behind its trail above a certain speed - it's the pearling instability. Our experiments and the nonlinear theory exhibit the same trend: the instability threshold decreases with increasing dissipation ratio at fixed equilibrium contact angle. This work also opens prospective as regards the curvature at the tip of cornered drops just below the instability threshold. Measurements in the rigid case suggest that nanometric scales regularize the corner. Yet, the characteristic size of the wetting ridge, called the elastocapillary length, impacts the rear curvature in our systems. The smaller the elastocapillary length, the sharper the corner, in agreement with the observed shapes. Further investigation should unveil how does this micrometric length scale couple with the molecular length scale to regularize the corner.

Keywords: wetting, elastowetting, viscoelasticity

Part I

Introduction

Chapter 1

General Introduction

Cover picture taken from [1]

It is the matter of a simple walk through Jardin des Plantes in Paris to stand in awe in front of lotus leaves over which droplets of water jiggle as though they were beads (Fig. **1.1**a). This sight is an occurence of a peculiar state of contact between water and the leaf, where the liquid does not wet at all the surface it lies on.

Scientists in the field of interface science now understand how to tailor artificial surfaces that mimick this state of wetting, using patterned surfaces akin to that of the lotus leaf on which droplets sit with the smallest contact possible (Fig. **1.1**b,c and c). This engineering feat is one example among many others of the achievements that the study of the contact of liquids with other materials, be they solid or liquid, has allowed.

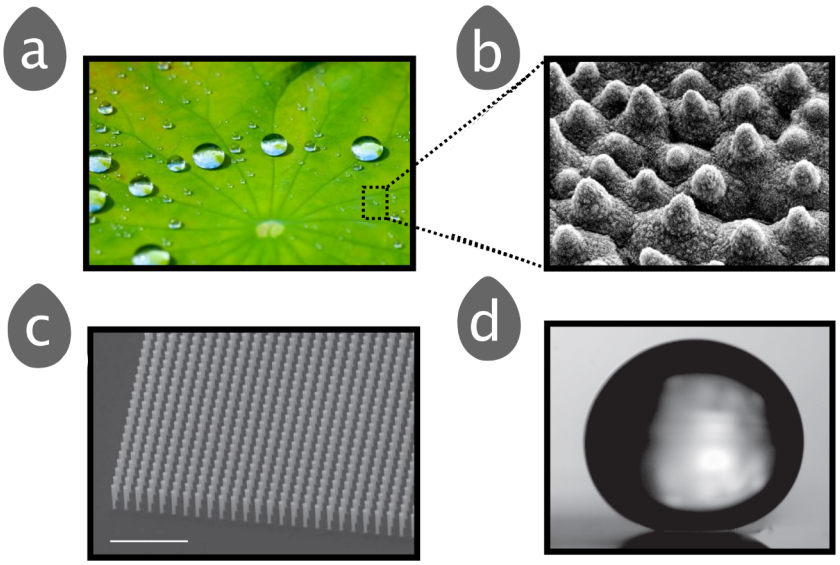

Figure 1.1: **Lotus effect.** A lotus leaf at different scales. (a) Drops do not spread on lotus leaves and remain almost spherical [2]. (b) Microscopic roughness gives lotus leaves their super-hydrophobic properties [3]. Super-hydrophobicity in the lab. (c) Forest of micro-pillars. Scale bar: 50 µm. [4]. (d) A liquid drop rests on the micro-pillars, akin to a fakir on an acupressure mat [4].

The study is relevant across all fields of fundamental science, and it is at the heart of innumerable processes and devices. From the standpoint of physics, wetting is a formidable door to all scales ranging from the nanometer to the millimeter. Its understanding requires that concepts from hydrodynamics, statistical mechanics, and surface science be combined. In biology, key processes such as protein folding rely on the details of the contact between water and organic molecules. Chemists and surface engineers synthesize and design new molecules that can be coated on the surface of glass and other materials so that the surface attracts or repels contact with liquids. Industrial sectors such as the aircraft industry or clothing rely on these advances to design anti-icing wings and rainproof coats (Fig.1.2).

In most of these cases, the liquid of interest wets a rigid surface. The material supporting the liquid, called the substrate, could however be a liquid or a deformable solid. The latter system has attracted a lot of attention over the years, and this manuscript describes recent advances that I have achieved during my PhD on this topic.

The behavior of a liquid in contact with a surface depends on the surface itself: chemistry, roughness, and geometry impact wetting. The compliance of the substrate is also a critical parameter. If the solid is compliant enough, forces that apply at the line of contact between a droplet, the substrate, and the surrounding fluid can deform the substrate, forming a so-called wetting ridge. Specific wetting phenomena arise in these configurations.

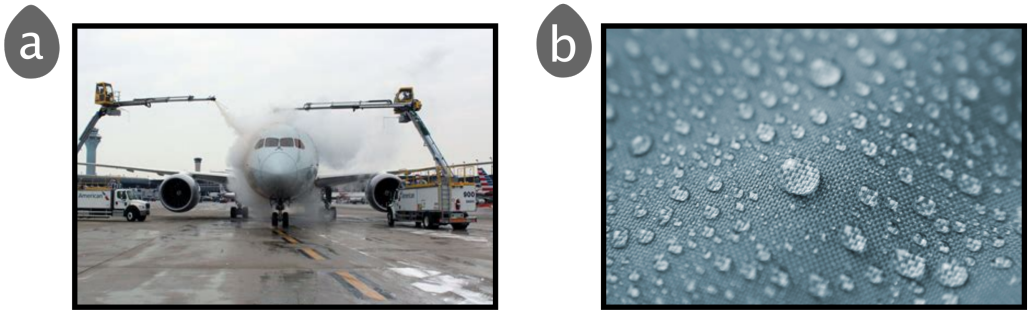

Figure 1.2: **Superhydrophobicity: from cars to clothes.** (a) Anti-icing treatment of planes [5]. The plane is sprayed with a hydrophobic coating so ice cannot form. (c) Water-repelent textile [6].

Surfaces coated with soft layers are known to be better dew collectors [7]. The softness of the silicon gel boosted both the nucleation rate and density of dew droplets (Fig. 1.3). The authors suggest that the deformable properties of the substrate reduce the free energy of a condensing drop (at a given liquid volume, the solid/vapor interface increases with the softness). Wetting ridges prevent merging with another drop. There are however issues to be solved with respect to water drainage, and circumventing these problems requires that we understand the dynamics of wetting on soft layers more thoroughly.

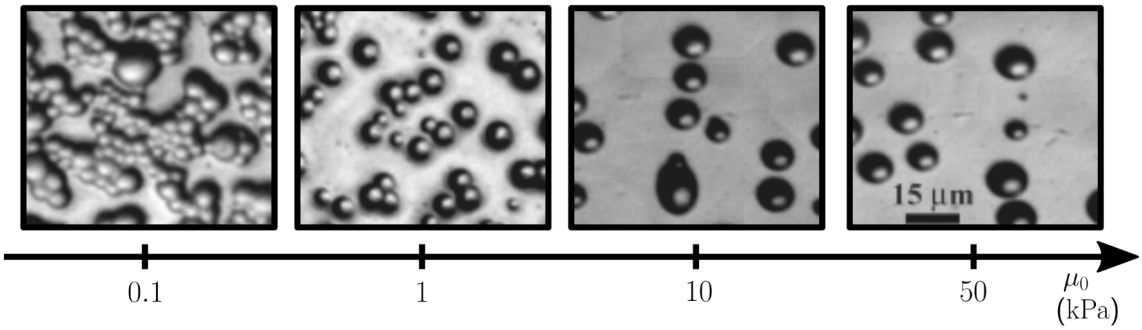

Figure 1.3: **Soft substrates enhance water condensation**Water drops condensate onto silicon gels with increasing stiffness (characterized by the elastic shear moulus μ_0, to be defined later). Experimental conditions are identical. The softest substrate collects the most water. Adapted from [7]. Scalebar: 15 µm

Despite decades of effort towards building an understanding of wetting for soft substrates (aka elastowetting), we still do not have a widely accepted description of the problem. The present work intends to test a recent model that the group of Julien Dervaux, Laurent Limat, and Matthieu Roché proposed a few years ago against experiments. The purpose is not so much to provide a definitive framework for the description of elastowetting as to discuss the insights we gain by using this model.

This manuscript is divided into three parts. The first part introduces the reader to wetting. Chap. **2** introduces the basics of wetting physics, both in the rigid and soft case, and Chap. **3** justifies our choice to perform sliding droplet experiments. The second part details our materials and methods. Chap. **4** describes the liquids and gels used in our experiments, while Chap. **5** focuses on the experimental protocol. The third part presents our observa-

tions and results, and discusses the ability of the model to capture them. Chap. **6** describes how the shape of droplets depends on the properties of the liquid-solid system, with a focus on the effect of dissipation. Chap. **7** focuses on the characterization of droplet motion. We discuss our results in the light of the model that the group proposed a few years ago in Chap. 8 and we highlight some interesting insights that we gain from this comparison. Finally, we conclude with some perspectives in Chap. 9, introducing experimental work that still needs effort and discussing how the elastocapillary length may play a role in setting the shape of droplets and their dynamics. We provide a general conclusion in Chap. 10.

Chapter 2

From rigid to soft wetting

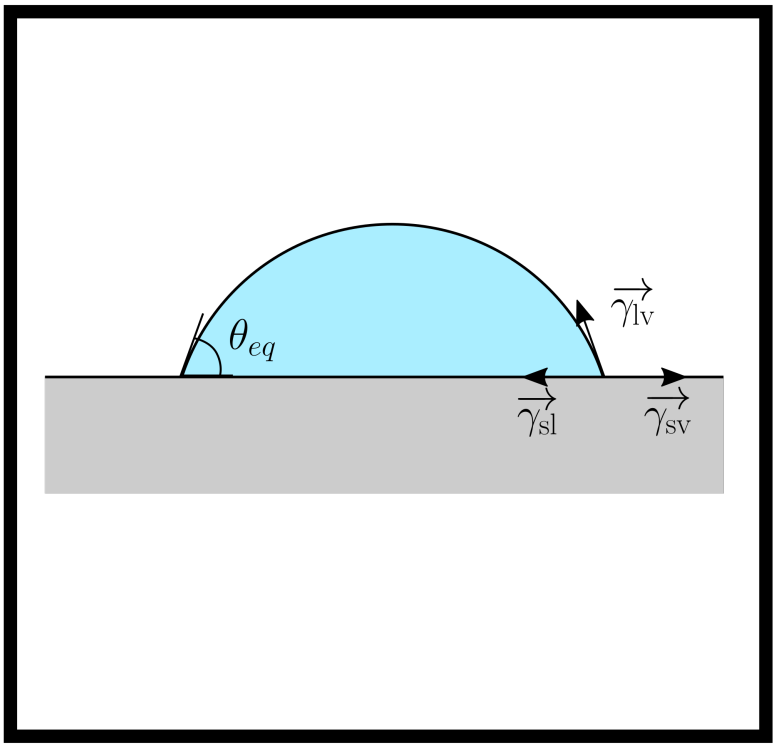

We provide here the fundamental physical concepts that are necessary to describe wetting situations. In particular, we discuss how the compliance of the solid and its rheology plays a role in wetting.

2.1 A primer on capillarity

2.1.1 Surface energy

Wetting consists in bringing a liquid in contact with a substrate (another liquid, a solid ...), sometimes in a surrounding fluid. This contact involves interfaces between each couple of media. Describing wetting requires that we understand the physics of interfaces.

One of the simplest systems to understand this physics is a horizontal soap film formed in a frame. A wire, free to move, lies in the film and is wetted by the fluid. If we puncture the soap film on one side of the wire, the remaining soap film pulls on the wire so that the area of the film interface with air goes down to zero (Fig. **2.1**). Thus, a work $d\mathrm{W}$ is associated with the area change $d\mathrm{A}$:

$$d\mathrm{W} = 2\gamma d\mathrm{A} \tag{2.1}$$

where γ is in units of energy per unit area[1]. The latter quantity is usually referred to as the surface energy. Systems will try to minimize the areas of the interfaces they encompass to reduce their energy.

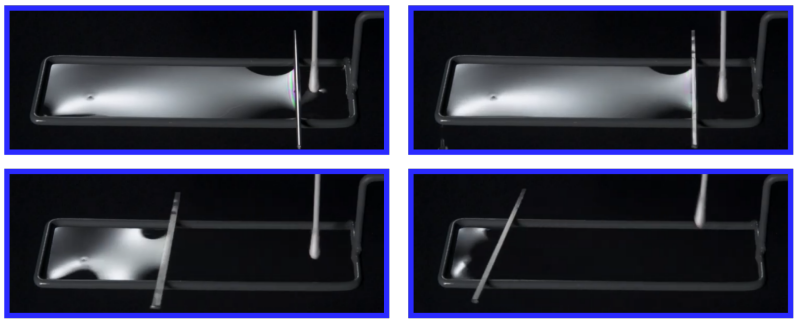

Figure 2.1: **The surface tension of a soap film drags a wire.** A wire, free to move, lies in a soap film. The soap film drags the wire when a cotton bud bursts one side of the film (time increases from left to right then from top to bottom) [8].

From the molecular point of view, a change in the area of an interface can be obtained by two non-exclusive processes [9]. In the first one, the bulk of both media exchanges molecules with the interface. This process involves breaking intermolecular bonds. In the case of liquids, the relation between bond breaking and surface energy (usually named surface tension) allows us to provide an estimate of the latter. For example, the typical energy associated with a bond in non-polar liquids is of the order of 25 meV [10]. Taking the square of the intermolecular distance a as the unit area, and setting $a \sim 0.2$ nm, we obtain $\gamma \sim 10$ $\mathrm{mN\,m^{-1}}$, in good agreement with the order of magnitude of experimentally determined surface tensions. In the second surface-creating process, the number of molecules at the interface remains constant but the average intermolecular distance changes. This dependence of

[1] The factor 2 comes from the fact that there are two interfaces between air and soap.

surface energy on strain is documented experimentally for enthalpic crystalline and amorphous solids [9, 11], *i.e.* solids whose elasticity results from the reaction of intermolecular bonds to strain [12], and it is known as the Shuttleworth effect in the literature [13]. This effect disappears for liquids, as they flow under strain. It is debated for polymer gels (that we use in our experiments). For instance, nuclear magnetic resonance measurements showed that such materials behave like a liquid at molecular scales [14].

2.1.2 Curved interfaces: Laplace pressure

Let us consider a curved droplet surrounded by an atmosphere at pressure P_{atm}. Besides the two aforementioned subsystems, the atmosphere-droplet system contains a third element: the curved air-interface. We impose that temperature and the number of molecules of each subsystem remain constant. Then, if we change the volume of the droplet by an amount dV_d, the atmosphere experiences work and we have [9]:

$$-P_{atm} dV_{atm} = -P_d dV_d + \gamma dA \tag{2.2}$$

Now, we note that $dV_{atm} = dV_d$. Besides, we know from differential geometry that:

$$\frac{dA}{dV} = \frac{1}{R_1} + \frac{1}{R_2}. \tag{2.3}$$

After rearrangement, we obtain:

$$\Delta P = P_d - P_{atm} = \gamma \left(\frac{1}{R_1} + \frac{1}{R_2} \right) \tag{2.4}$$

where R_1 and R_2 are the local radius of curvature in two perpendicular directions at a given point (Fig. 2.2b). Equation **2.4** simplifies for a spherical droplet of radius R:

$$\Delta P = P_d - P_{atm} = \frac{2\gamma}{R}. \tag{2.5}$$

We see that surface tension induces a pressure jump inside the droplet, called *Laplace pressure* [15].

2.1.3 Capillary length

On Earth, droplets experience gravity. In general, the pressure balance inside the droplet should involve a hydrostatic contribution besides the capillary one. Now, we can focus on a droplet for which these pressures are equal:

$$\frac{\gamma}{R} = \rho g R \tag{2.6}$$

We see that this balance defines a length scale known as the capillary length:

$$R = \lambda_c = \sqrt{\frac{\gamma}{\rho g}}. \tag{2.7}$$

This length scale sets the separation between droplets and puddles in wetting. If the characteristic size of the drop is below λ_c, capillarity minimizes the energy cost of the liquid/air interface, and the droplet is a spherical cap (Fig. **2.3**b). Otherwise, gravity flattens the interface, at distances farther than λ_c : we have a puddle (Fig. **2.3**c).

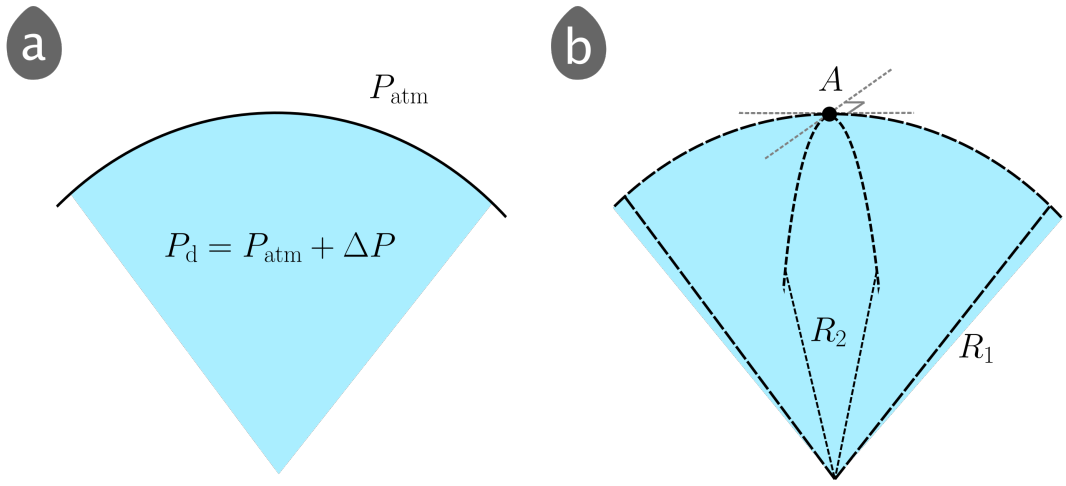

Figure 2.2: **Laplace pressure for a curved interface.** (a) The concave part is under overpressure ΔP = $\gamma(R_1^{-1} + R_2^{-1})$ (b) R_1 and R_2 are the local radius of curvature at point A, in two orthogonal directions (grey dashed lines).

2.2 Statics of wetting

In this section, we remind the reader of the basic notions describing the wetting of a substrate by a liquid. We restrict our discussion to the case of a solid on which the liquid forms droplets. We also introduce the concepts allowing to describe wetting of deformable solids.

2.2.1 Spreading parameter

As we have seen in section **2.1**, interfaces have an energetic cost. In the light of this result, the shape of a droplet sitting on the surface of a substrate will depend on whether the substrate prefers to remain dry or wet [16]. This tendency is captured by the spreading parameter $S = \gamma_{sv} - \gamma_{sl} - \gamma$, with γ_{sv}, γ_{sl}, γ respectively the surface energies of the solid/vapor, solid/liquid and liquid/vapor interfaces. When $S > 0$, energy is minimal when the liquid coats the solid: the system is in a state of total wetting (Fig. **2.3**a). On the contrary, when $S < 0$, the liquid finds a compromise between the three surface tensions and forms a droplet or a puddle. Wetting is then partial (Fig. 2.3b). In this case, the liquid, vapor and solid phases meet at the *contact line* (also called triple line or wetting line), and the liquid/vapor interface forms an angle θ_{eq} with the solid at equilibrium. The puddle is observed when the size of the droplet is greater than the capillary length λ_c (Fig. 2.3c).

2.2.2 Shape of the droplet at equilibrium: from rigid to soft substrates

Young-Dupré relation

In the case of partial wetting, the liquid-vapor interface is inclined with respect to the solid-liquid interface by an (equilibrium) angle θ_{eq}. *Young* was the first to understand that the energies associated with the three interfaces (e.g. γ, γ_{sv} and γ_{sl}) set θ_{eq} [17]. *Dupré* formalized this idea and came up with the famous *Young-Dupré* relation [18]:

$$\boxed{\cos\theta_{eq} = \frac{\gamma_{sv} - \gamma_{sl}}{\gamma}.} \tag{2.8}$$

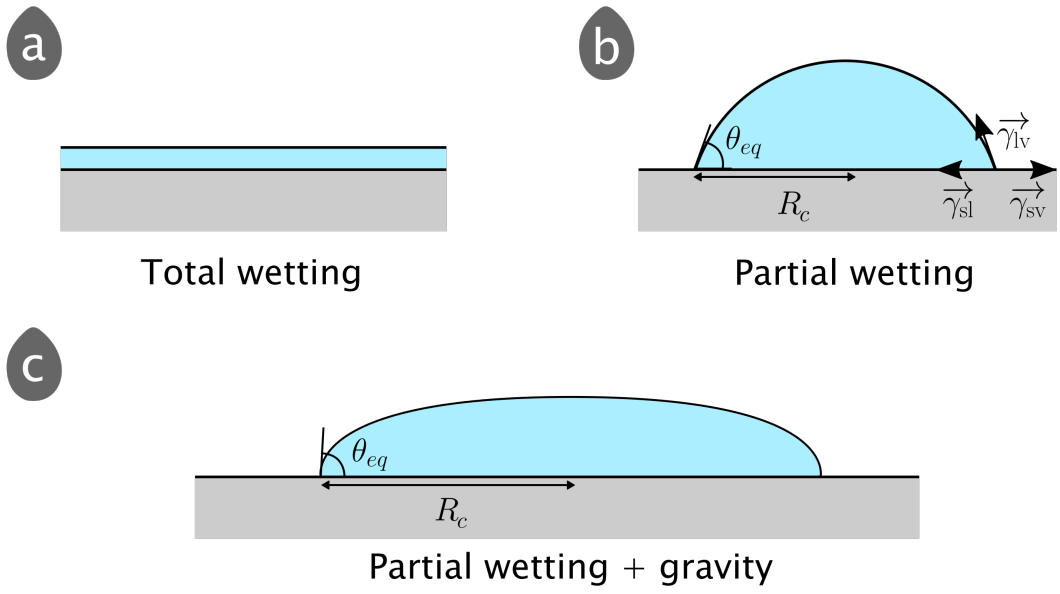

Figure 2.3: **Wetting on a rigid plate.** (a) Total wetting (b) Partial wetting. (c) Gravity flattens drops whose characteristic size exceeds the capillary length λ_c. R_c is the contact radius between the drop and the solid. The surface tensions of the three interfaces $\overrightarrow{\gamma_{sl}}$, $\overrightarrow{\gamma_{sv}}$ and $\overrightarrow{\gamma}$ set the contact angle θ_{eq} according to the *Young-Dupré* relation.

Equation **2.8** is established assuming that the substrate is rigid and ideal. These assumptions lead to puzzling issues when compared to real systems. First, measurement of the surface energies involving the solid, γ_{sv} and γ_{sl}, is challenging in practice. Scientists bypass this issue by measuring γ and θ_{eq} first. Second, Young-Dupré's law suggests that the equilibrium contact angle is single-valued. As a consequence, we expect that the contact line moves as soon as the angle departs from θ_{eq}. In most practical instances, the contact line is pinned by surface defects (surface roughness, chemical impurities...). Its motion occurs only if the contact angle reaches a threshold value. This value differs whether we consider forward or backward motion. These threshold angles are known as the advancing and receding contact angles $\theta_{s,a}$ and $\theta_{s,r}$ [19]. Their difference $\Delta\theta$ is the *contact angle hysteresis*. Thus, the equilibrium contact angle is often ill-defined: a range of values is observed. Next section deals with the remaining issue, a puzzling one that has to do with the actual force balance.

Deformable substrates : the surface-normal force balance

The last issue with the assumption of an ideal non-deformable substrate is that young-Dupré's relation is established forgetting the components of the force balance directed normal to the surface of the substrate, which seems to remain unbalanced in Fig 2.3b. To the best of our knowledge, *Bikerman* was the first to discuss the problem. He carried out experiments in which he dipped a gelatin bar into a bath of mercury, and reported deformations of the surface of the bar of the order of several tens of micrometers [20, 21]. His observations questioned the validity of Young-Dupré's relation. A long debate ensued, and studies of the wetting of soft materials, or *soft wetting*, started to appear.

Lester performed a theoretical analysis that would be the first step in setting the debate around the validity of Eq. **2.8** [22,23]. He investigated how Laplace pressure deformed a compliant substrate when a droplet sits on its surface. The force balance he sets up involves also

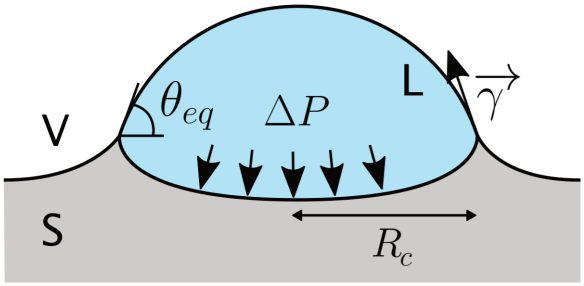

Figure 2.4: **Wetting on a soft substrate.** A drop rests on a compliant solid with contact radius R_c and equilibrium contact angle θ_{eq}. Laplace pressure ΔP pushes on the substrate (downwards arrows) while surface tension $\vec{\gamma}$ pulls the contact line upwards. A wedge-like deformation known as the ridge arises.

bulk elastic stresses (Fig. 2.4). The way he builds his model imposes that he attributes a width w to the liquid-vapor interface. His conundrum leads him to identify a length scale that is intrinsic to the three-phase system [22]:

$$\ell \sim \gamma/E, \tag{2.9}$$

where γ is the liquid/vapor surface tension and E is the Young modulus of the solid. Setting $w = 10^{-9}$ m, *Lester* concludes that the Young-Dupré relation suits the description of equilibrium contact angles when $\ell/w << 1$, *i.e.* when E ~ 1 GPa). In contrast, ℓ reaches mesoscopic scales for an elastomer ($\ell \sim 10^{-5} - 10^{-4}$ m when E ~ 1 MPa): Young-Dupré's relation cannot be applied safely in this case. An alternative description must be used, reminiscent of Neumann's construction for liquids. In the latter case, *Lester* predicts a wedge-like deformation. The vertical displacement of the solid around the contact line proportional to $\log(R_c/w)$, where R_c is the contact radius of the drop. Hence, strain diverges as the interface becomes infinitely thin [24]: a singularity arises at the tip of the ridge. It took a while however to test Lester's predictions for the shape of the ridge.

Shape of a static ridge

Experimentalists have attempted to image the wetting ridge as close as possible to its apex. For instance, *Extrand & al.* [25] used optical microscopy to spot the wetting ridge after drop removal (Fig. 2.5a), while *Andrade & al.* [26] used scanning electron microscopy to image the contact line between octane drops or air bubbles and a water-immersed polymer gel. However, none of these study quantifies the deformation profile [24].

Carré & al. imaged the solid/vapor side of the wetting ridge using scanning white-light interferometric microscopy (Fig. 2.5b) [27]. They could test the logarithmic height profile predicted by theory [27, 28]:

$$u_z(x) \simeq \frac{\gamma \sin\theta_{eq}}{2\pi\mu_0} \log\left(\frac{L}{x}\right), \qquad x > \epsilon, \tag{2.10}$$

where $u_z(x)$ is the height of the solid/vapor interface at a distance x from the contact line, L a macroscopic cutoff distance and μ_0 the elastic shear modulus of the material. Their treatment holds for x farther from a microscopic cutoff ϵ, below which the theoretical prediction becomes unphysical [27, 28].

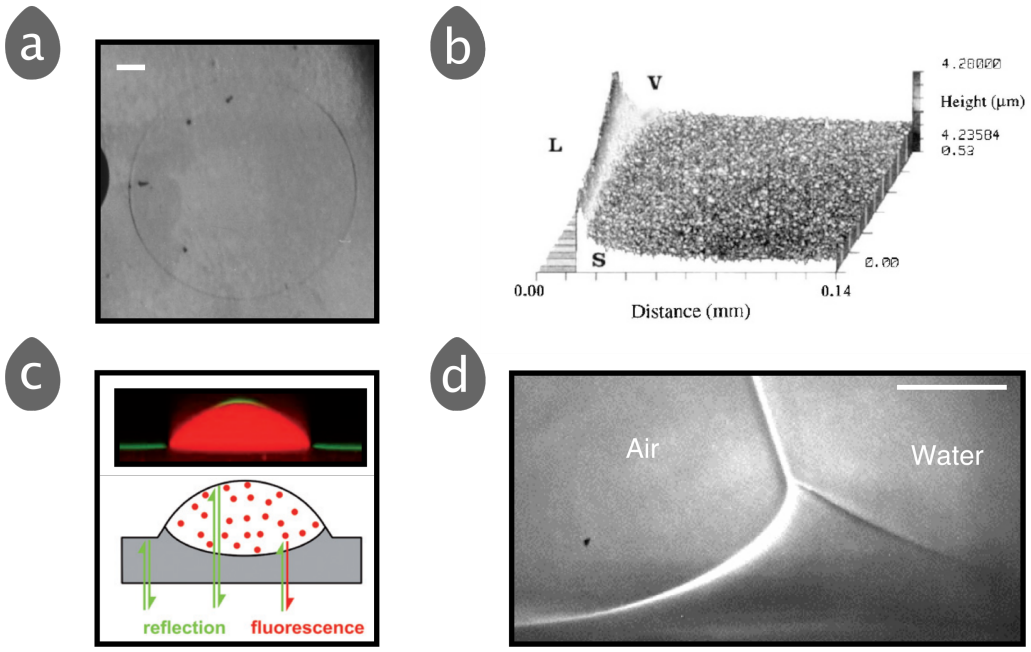

Figure 2.5: **Imaging the wetting ridge.** (a) Top view of a relaxing ridge after drop removal. The ridge already started to relax. The photograph is taken from [25]. Scale bar: ~ 1 mm. (b) White-light interferometric microscopy imaged the solid/vapor interface [27]. The ridge rises by ≃ 30 nm. (c) Imaging both sides of the wetting ridge with laser scanning confocal microscopy. Typical image (top) and the principle of measurement (bottom). Laser scanning confocal microscopy unveils the solid/vapor and liquid/vapor interfaces (green lines), while the fluorescent dye dissolved in the drop unveils the solid/liquid interface (red patch). Adapted from [29]. (d) X-ray microscopy pushed the boundaries of resolution (~ 50 nm px^{-1}) and imaged an asymmetrical deformation. A water drop rests on a silicone gel (E = 3 kPa) and lifts a ridge by 8.3 µm. Scale bar: 5 µm. Adapted from [30].

Measuring the profile of the ridge is a challenge to experimentalists. For instance, optical profilometry offers good precision but misses the wet side of the ridge under the droplet. Attempts relying on the fact that the ridge does not relax immediately after droplet removal was carried out [31–33], but the ridge flattens rather fast in most cases [24,34,35]. The breakthrough came from the use of laser scanning confocal microscopy. By dying the droplet with a fluorescent species, displacements on both sides of the contact line could be measured (Fig. 2.5c and Fig. 2.6a) [29, 36, 37]. This technique provided key insights into the shape of the ridge and the force balance at the tip. The shape was shown to be universal in a domain around the contact line the extent of which is of the order of the length scale ℓ identified by Lester [37]. Reexamination of these results in the light of papers by *Ajdari & al.* and *Limat* [38–42] suggests that the extent of the universal domain compares well with the intrinsic elasto-capillary length of the substrate:

$$\ell_s \sim \frac{\gamma_s}{\mu_0} \tag{2.11}$$

where γ_s is the surface energy of the substrate[2]. For distances to the contact line smaller than l_s, solid surface tension resists vertical displacement. Beyond l_s, bulk elasticity resists

[2] In wetting problems, the authors assume that γ_s is uniform on both sides of the ridge [42].

vertical displacement. From now on, we define l_s as follows:

$$l_s = \frac{\gamma_s}{2\mu_0}. \tag{2.12}$$

Besides the universal features of the ridge, confocal microscopy images also highlighted that the ridge is sensitive to finite-depth effects (Fig. 2.6a) [29]. While the surface of the solid remains flat away from the contact line for thicknesses beyond the millimeter, a dimple surrounds the ridge when the thickness is sub-millimetric. The depth of the dimple increases with decreasing thickness (Fig. 2.6b) [43, 44].

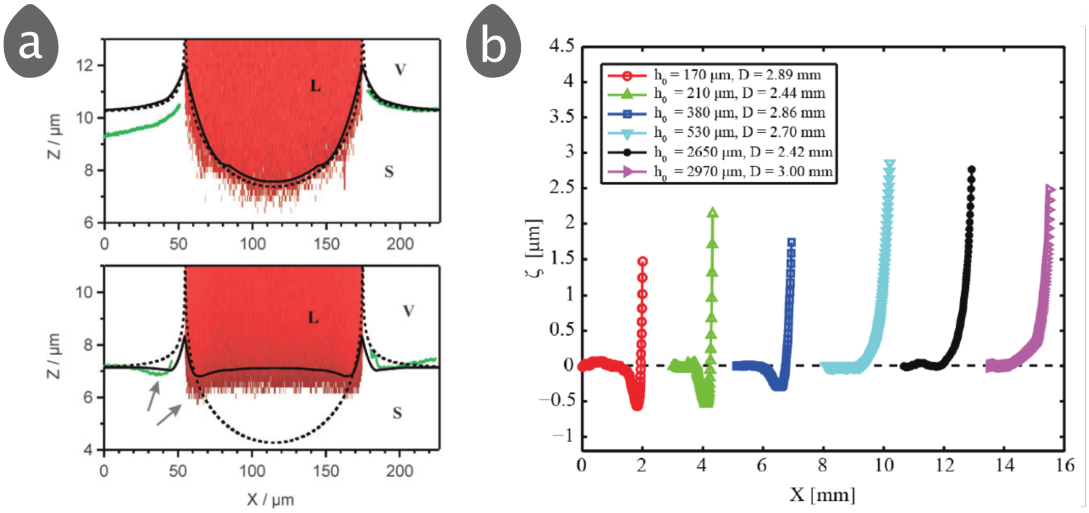

Figure 2.6: **Thickness effects on the wetting ridge.** A dimple arises from the incompressibility of the gel when the thickness of the layer h_s decreases. (a) Typical images obtained by laser scanning confocal microscopy when h_s = 104 µm (top) and h_s = 8.5 µm (bottom) [29]. The green line is the solid/vapor interface, the red patch is the fluorescent drop. Dotted and solid lines are theoretical and numerically simulated profiles. The gel has a Young modulus E = 25 kPa. (b) Solid/vapor deformation profile with increasing thickness obtained by optical interferometry. In [43], h_0 is the thickness of the viscoelastic layer, D the diameter of the drop). The gel has a shear modulus μ_0 = 1.2 kPa. A dimple appears when the thickness of the gel h_s reaches (a) h_s = 8.5 µm and (b) h_s = 380 µm.

Further progress in imaging techniques refined the resolution of the profile well below the elastocapillary length. For example, X-ray microscopy visualizations of the ridge challenged the proposed theoretical profiles. Up to then, models mainly considered symmetric ridges: the surface tension of the solid is identical on both sides of the contact line and the equilibrium contact angle is then $\theta_{eq} = \pi/2$. The resulting capillary force at the contact line is normal to the surface [40–42, 45]. *Park & al.* observed asymmetric ridges when a water drop rests on a silicone gel [30] that models at the time had difficulties to describe (Fig. 2.5d). These authors also showed that the ridge slowly grows at a constant rate $U_g \sim 7$ nm s^{-1} and opening angle at the apex $\theta_s = 56.3 \pm 5.1°$. This latter dynamical feature is accounted for in only a few models that aim at describing how a liquid wets a gel containing a solvent using a poroelastic framework [35].

2.2.3 Boundary condition at the contact line : the need for non-linearities

Visualization of the apex of the ridge opens the possibility to discuss its shape and the force balance that sets it. This discussion is mentioned early on in the literature. As we have seen in

Sec. 2.2.2, the first predictions for the shape of the ridge indicate that displacements diverge around the apex of the ridge. This divergence is obviously regularized in the physical system, but what is behind this regularization?

Even at the best available spatial resolution (~ 50 nm px^{-1} [30] with X-ray microscopy), the apex of the ridge appears sharp. The length scale that regularizes it remains uncharted experimentally, and the force balance at the very tip remains unclear.

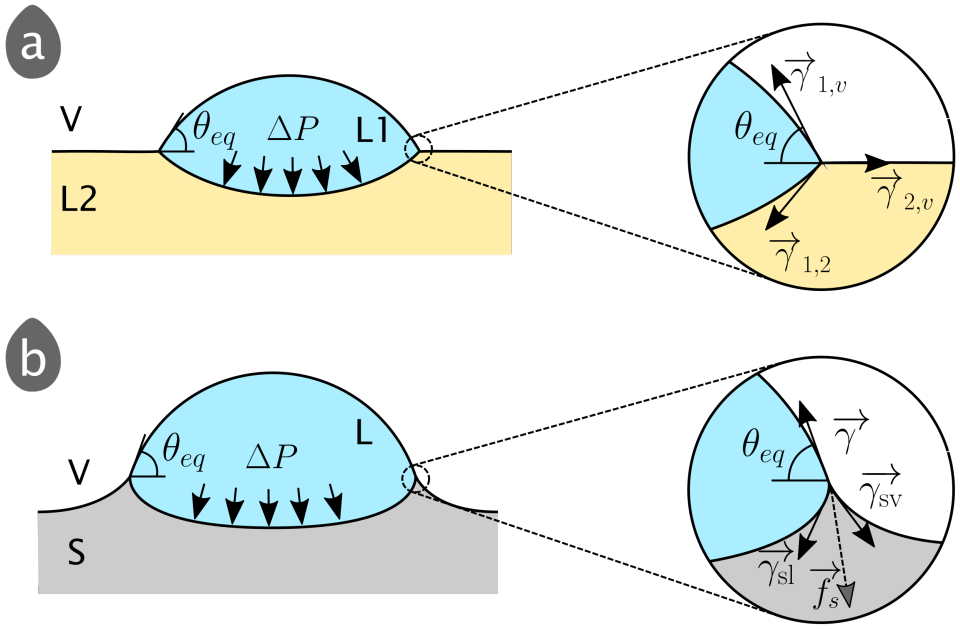

Figure 2.7: **Force balance at the contact line for a deformable substrate.** The surface tension $\vec{\gamma}$ pulls the contact line and the Laplace pressure ΔP pushes on the substrate. (a) Neumann's condition sets the contact angle when the substrate is a liquid bath. The three surface tensions balance themselves. (b) A compliant solid might apply a force $\vec{f_s}$ coming from its bulk rheology (here we do not represent $\vec{f_{ext}}$). Some models include this possibility, others state that Neumann's condition holds for soft solids as well.

Given the arrangement of capillary forces at the contact line, it is tempting to describe the system following the rationale used to establish force balance at a three-phase contact line when all phases are fluids. This force balance, known as Neumann's construct, sets the equilibrium contact angle between a liquid drop resting on a non-miscible liquid bath [46] (Fig. 2.7a). The liquid/vapor surface tension of the drop pulls on the liquid bath, while the surface tensions of the interfaces of the latter with the droplet and vapor surface resist this traction. This balance is thus summed up by ():

$$\vec{\gamma}_{1,2} + \vec{\gamma}_{1,v} + \vec{\gamma}_{2,v} = \vec{0} \tag{2.13}$$

Most theoretical analyses of the wetting of substrates assume that Eq. 2.13 is valid, at least for soft substrates [42, 47–50]. However, questions arose when Neumann's construct was used to obtain values for the surface tension of the solid γ_s [37, 51–54]: the values were much greater than those of silicone oil, the polymeric liquid used as a base to obtain the elastomers used by most experimentalists. Past literature suggested caveats that could lead to a possible misinterpretation of this balance. For example, Shanahan and De Gennes [55] indicate that non-linear processes such as plasticity may play a role in the vicinity of the contact line. A discussion started in the community.

The linearity of the models used to describe soft wetting was soon identified as a potential issue. Various ways to extend the models were proposed such as an analogue of the Shuttleworth effect for soft materials, the existence of a skin layer at the surface,etc... Confirming the existence of these effects is difficult. The skin effect was tested with success on plasma-treated silicone samples [56]. The Shuttleworth effect was shown very recently to be of small amplitude [57], even more so when compared to the prediction of the linear theory [51].

The other direction some authors have explored is to develop a model where the description of the elasticity of the solid includes terms of order greater than 1 in strain [56, 58–61]. Indeed, linear models indicate that the slope ζ' of the substrate surface follows [62]:

$$\zeta' \propto \frac{\gamma}{\gamma_s}. \tag{2.14}$$

They are only valid when $\zeta' \ll 1$. However, elastowetting experiments never verify the condition $\gamma/\gamma_s \ll 1$. On the contrary, this term is of order 1. Hence, strains are finite rather than vanishing, and a non-linear theory of elasticity should be used in place of the linear one. Our group proposed such a model recently [59] in which surface tension of the substrate is considered independent of strain. Moreover, the authors assume that a singularity in the strain field of the solid exists at the apex of the ridge. As a consequence, the solid exerts a force $\vec{f}_s$ at the apex of the ridge:

$$\vec{\gamma} + \vec{\gamma}_{sl} + \vec{\gamma}_{sv} + \vec{f}_{ext} = \vec{f_s} \tag{2.15}$$

where $\vec{f}_{ext}$ is an external force applied to the substrate. The latter could be a hydrodynamic force exerted by a moving drop for example. In this case, the model can describe quite well experimental data relating the opening angle at the apex of the ridge to stretch [51], and it returns values for the surface tension of the solid that are close to that of silicone oil, $24\,\mathrm{mN\,m^{-1}}$ compared to the expected value of $21\,\mathrm{mN\,m^{-1}}$.

2.3 Dynamics of wetting

To the best of our knowledge, dynamic contact lines have been under study since *Ablett*'s work in 1923 [63]. The author remarked that the contact angle between a rotating parrafin-wax-coated cylinder and a water bath decreases (respectively increases) as the cylinder accelerates clockwise (respectively anticlockwise). This observation has been confirmed extensively since then, and several models attempt to describe how the contact-line velocity U sets the dynamic contact angle θ_d [64, 65]. We provide here an overview of the literature on the dynamics of wetting and introduce recent work focused on soft substrates.

2.3.1 Flow with vanishing height: stress divergence at the contact line

The flow produced by a droplet spreading on a solid substrate is peculiar in that its size goes to zero as we move closer and closer to the contact line. Let us analyse this situation (Fig. **2.8**). Focus on the contact line immediately brings forth an issue with boundary conditions. We expect that the liquid in contact with the solid flows at a velocity U_L identical to that of the solid. Hence, if the solid remains still, we expect $U_L = 0$ at the solid-liquid interface. Viscous stresses, which hinder motion, then diverge:

$$\sigma = \eta \partial_z U \sim \eta \frac{U}{h} \to \infty \text{ when } h \to 0 \tag{2.16}$$

Eq. **2.16** states that the contact line requires an infinite amount of energy to move, which strongly disagrees with everyday's experience – drops do spread on surfaces. Huh and Scriven were the first to highlight this puzzling paradox [66].

Theoretical models circumvent this paradox in various ways. For example, a common assumption is that the liquid slips onto the solid. Models account for this by the introduction of a slip length λ that corresponds to the depth at which the speed should vanish below the solid-liquid interface [67, 68]. In the case of complete wetting, a thin film forms at the front of the macroscopic contact line. Then, disjoining pressure regularizes stress divergence [69]. Finally, kinetics at the molecular scale have also been investigated, leading to the MKT framework in which stochastic hopping of molecules along the surface drives contact line motion [70]. Each approach has its own pros and cons, and none perfectly describes experimental data [71] – how microscopic scales regularize the aforementioned divergence remains an open question.

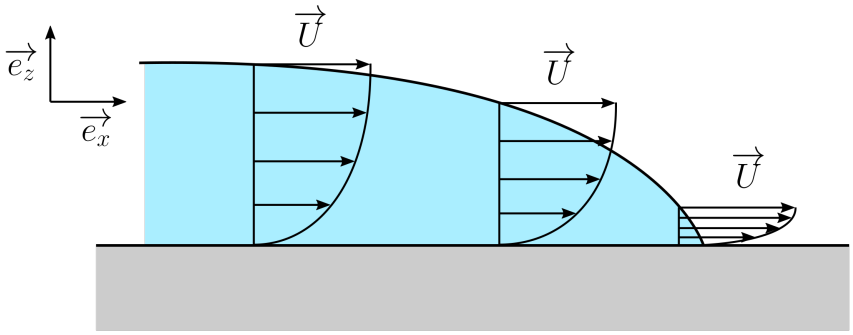

Figure 2.8: **Viscous stresses rocket near the contact line.** Velocity field for a a drop moving to the right. The liquid/vapor interface moves to the right at speed $\vec{U}$, and there is no slip onto the solid. The vertical velocity gradient explodes as we draw near to the contact line.

In the following section, we only present the Cox-Voinov model [67, 72]. The reader interested in other models shall look at simplified derivations in [73–75] and references therein.

2.3.2 Cox-Voinov model

We consider a two-dimension curved contact line moving on a rigid plate (Fig. 2.9a). Variation of the curvature along the liquid/air interface (and hence of Laplace pressure) sets motion in, and viscous dissipation hinders it. We assume that the flow is stationary and we neglect convective terms; Navier-Stokes equation reduces to Stokes equation. We assume that the liquid/air interface, described by its height $h(x)$, has small slopes. We adopt the lubrication approximation and assume that fluid velocity is directed parallel to the solid surface:

$$\vec{\mathrm{U}}(x,z) = \mathrm{U}_x(x,z)\vec{e_x}. \tag{2.17}$$

Altogether, we obtain:

$$-\frac{\partial \mathrm{P}}{\partial x} + \eta \frac{\partial^2 \mathrm{U}_x(x,z)}{\partial z^2} = 0 \tag{2.18}$$

Capillary and viscous stresses dominate close enough to the contact line. The pressure P inside the liquid reduces to the capillary pressures:

$$\mathrm{P}_{\mathrm{int}} = \mathrm{P}_{\mathrm{out}} - \gamma \frac{\partial^2 h(x)}{\partial x^2}, \tag{2.19}$$

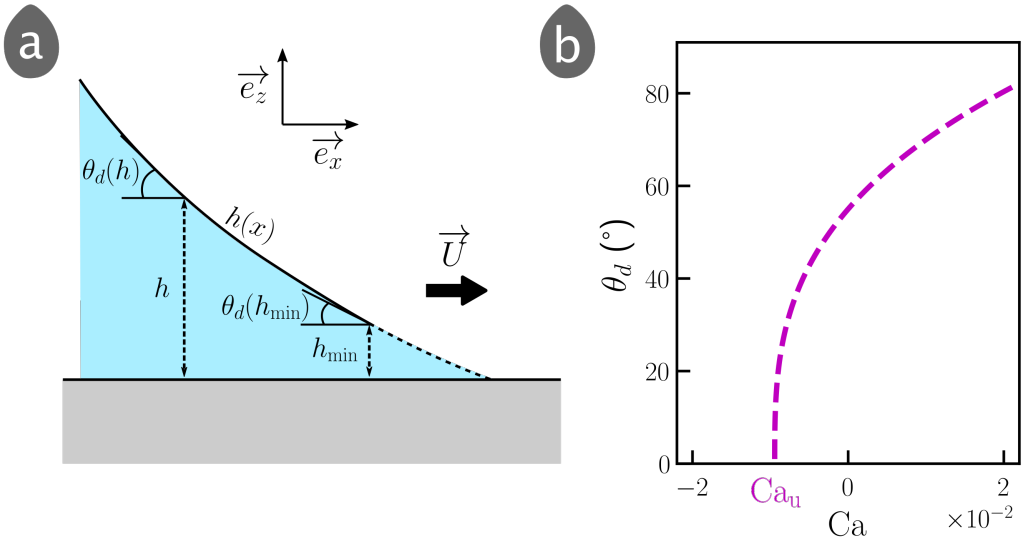

Figure 2.9: **Cox-Voinov model.** (a) Schematic of a curved triple line advancing onto a rigid plate. The gradient of capillary pressure drives the motion, viscosity hinders it. The profile $h(x)$ of the liquid air/interface advances at a speed $\vec{U}$. The dynamic contact angle θ_d depends on the height $h(x)$ at which it is measured. The cutoff length $h_{\min}$ circumvents the divergence of viscous stresses. (b) plot of the simplified Cox-Voinov law, for $h_{\min} = 3$ nm, $h = 100$ µm and $\theta_d(h_{\min}) = 55°$. It predicts a dewetting transition at zero receding contact angle.

where $-\partial^2 h(x)/\partial x^2$ stands for the curvature of a convex interface. Hence:

$$\frac{\partial^3 h}{\partial x^3} + \eta \frac{\partial^2 U_x(x,z)}{\partial z^2} = 0 \tag{2.20}$$

We can integrate twice over the vertical coordinate z, using the continuity of viscous stresses at the free surface and the no-slip boundary condition:

$$\partial U_x(x,z)/\partial z|_{z=h} = 0 \tag{2.21}$$

$$U_x(x, z=0) = 0 \tag{2.22}$$

We then retrieve a half-Poiseuille flow:

$$U_x(x,z) = \frac{\gamma}{\eta}\frac{\partial^3 h}{\partial x^3}\left(hz - \frac{z^2}{2}\right). \tag{2.23}$$

We define the liquid capillary number Ca as the speed of the liquid / air interface $U_x(x, z = h) = \|\vec{U}\| = U$ relative to the viscocapillary velocity $U_l = \gamma/\eta$ of the liquid. The following obtains:

$$Ca = \frac{h^2}{2}\left(\frac{\partial^3 h}{\partial x^3}\right). \tag{2.24}$$

The solution to Eq. 2.24 takes the form [72]:

$$\boxed{\theta_d(h)^3 - \theta_d(h_{\min})^3 = 9\,Ca \log\left(\frac{h}{h_{\min}}\right)}. \tag{2.25}$$

Here, $\theta_d(h)$ is the dynamic contact angle measured at height h. Below $h_{\min}$, additional physical ingredients must be introduced that will regularize the divergence of viscous stresses. Typically, $h_{\min}$ is a molecular scale.

The derivation above is valid at small slopes. In all generality, the relation between the angle and the capillary number writes [64, 67, 72]:

$$g(\theta_d(h)) - g(\theta_d(h_{\min})) = \mathrm{Ca} \ln\left(\frac{h}{h_{\min}}\right) \tag{2.26}$$

where

$$g(\theta) = \int_0^\theta \frac{\beta - \cos\beta \sin\beta}{\sin\beta} d\beta. \tag{2.27}$$

However, Eq. 2.25 is in good agreement with experimental data for angles up to $3\pi/4$ (135°!) [72], which may be surprising. Snoeijer actually showed that a law similar to Eq. 2.25 can be derived in the limit of stiff slope provided the slope of the liquid-vapor interface is slowly varying [76].

Fig. **2.9**b plots Eq. **2.25**. Negative and positive Ca respectively correspond to the receding and advancing branches. Eq. **2.25** describes experimental data well [71, 73, 74, 77]. It also constrains the values that the receding capillary numbers can take: below Ca_u, the receding contact angle vanishes and the liquid is expected to coat the substrate. As we will see later, experimental results question this prediction [77, 78].

2.3.3 Dynamics of soft wetting: dissipation everywhere

Replacement of the rigid substrate by a deformable one usually implies that the material used as the solid is a gel or an elastomer. However, gels and elastomers respond to mechanical solicitations as both an elastic solid and a viscous liquid. From the structural standpoint, this response is the result of the existence of a connected ("cross-linked") matrix of polymeric chains that can support stress like a solid. Its relaxation will not be immediate in general, as polymer chains rub on each other during this process, leading to viscous dissipation. On top of that, if a solvent is present in which the cross-linked matrix floats, the former may rearrange and lead to a so-called poroelastic response [35]. Thus, whereas the liquid was the sole dissipative medium when describing wetting of rigid surfaces, the substrate can dissipate energy in the case of soft substrates, eventually modifying the dynamics of the contact line. Experimental evidence for this modification exist and are summarized below.

Viscoelastic braking

Many studies performed at the turn of the 20th century highlighted that rubbers hinder spreading or sliding drops [27, 79–82]. The authors report that the substrate dissipates a fraction of the work done by the contact line to lift the ridge [79]. In this paper, they consider a liquid drop sliding onto an inclined rubber by the action of gravity. They build a scaling approach which consists in comparing power injected in the system by gravity to that dissipated. Injected power scales as:

$$\mathscr{P}_{in} \sim \rho g V U \tag{2.28}$$

with V the volume of the droplet. The expression of the scaling for dissipated power depends on where dissipation takes place. If the droplet dissipates the energy, we have:

$$\mathscr{P}_{diss} \sim \eta R U^2. \tag{2.29}$$

Equating $\mathscr{P}_{in}$ and $\mathscr{P}_{diss}$, we obtain:

$$\rho g R^2 \sim \eta U. \tag{2.30}$$

Dividing both sides by the surface tension of the liquid, we obtain:

$$\mathrm{Bo} \propto \mathrm{Ca} \tag{2.31}$$

where the Bond number $\mathrm{Bo} = \rho g R^2/\gamma$ and the capillary number $\mathrm{Ca} = \eta U/\gamma$ of the experiment have been introduced. This result will appear again later in this document when dealing with sliding drops. However, these authors observed trends closer to power-law behavior (Fig. 2.10). Attributing dissipation to the solid, they suggest that it scales as $(U/U_0)^m$, where U_0 and exponent m are intrinsic to rubber. Typically, m is below unity and comes from the dependence of losses in the material on the typical frequency at which it is excited. Their model was at least able to account for the power-law dependence. As motion hindrance was due to the viscoelastic solid, they named this phenomenon "viscoelastic braking".

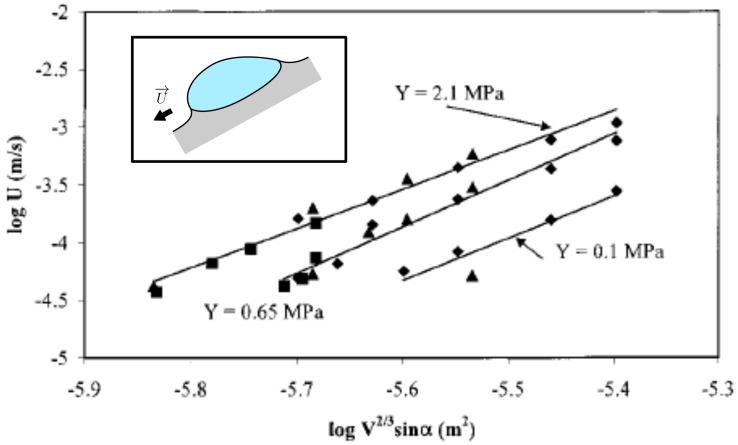

Figure 2.10: **Viscoelastic braking.** A *o*-tricresyl phosphate drops slide onto softer and softer silicon elastomers (inset). The Young modulii are E = 2.1 MPa, E = 0.65 MPa and E = 0.1 MPa. V is the volume of the drop, U its running speed and α is the inclination of the rubber. At a given product $V^{2/3}\sin\alpha$ (accounts for the "weight"), the running speed increases with the Young modulus. The three rubbers exhibit a power law with an exponent $m = 0.248 - 0.294$. Adapted from [79].

As far as we know, *Long & al.* were the first to identify the origin of the aforementioned speed U_0 from basic principles. They compare how much power P_{film} is dissipated inside a viscoelastic film when a contact line moves onto it. A key simplifying assumption in their model is that of equal magnitude for the surface energies of the solid with liquid and vapor, $\gamma_{sv} = \gamma_{sl} \equiv \gamma_s$. Many models since then use this hypothesis [44, 49, 62, 83]. Viscoelastic materials such as gels and elastomers often contain ill-connected polymer chains. These chains may be dangling if they are connected to the network only by one of their ends, and free if they are not connected at all. Both of these chain classes contribute to energy dissipation. *Long et al.* assume that the rheology of their materials is described by the empirical Chasset-Thirion relation [84, 85]:

$$G(\omega) = \mu_0(1 + (i\omega\tau)^m) \tag{2.32}$$

where τ accounts for polymer relaxation inside the material, μ_0 is the elastic shear modulus and m characterizes the energy loss inside the solid. Then the expression for dissipated power, per unit length of the contact line, is:

$$P_{film} = \frac{f_0^2}{\gamma_s}\left(\frac{\mu_0\tau U}{\gamma_s}\right)^m U \tag{2.33}$$

If we express $\mathscr{P}_{in}$ per unit length too and replace $f_0 = \gamma \sin(\theta_d)$, we obtain the following scaling:

$$Bo = \frac{\gamma}{\gamma_s} \sin(\theta_d)^2 \left(\frac{U}{U_0}\right)^m \tag{2.34}$$

that is in good agreement with data in Fig. 2.10. This relation stresses the key role of solid surface tension γ_s that resists the pulling force (per unit length) f_0. They also provide an expression, confirmed extensively since then, for U_0:

$$U_0 \sim \frac{\gamma_s}{\mu_0 \tau}. \tag{2.35}$$

As a last remark, we note that the case $\gamma_{sv} \neq \gamma_{sl}$ still challenges theoreticians.

Rotation of the ridge

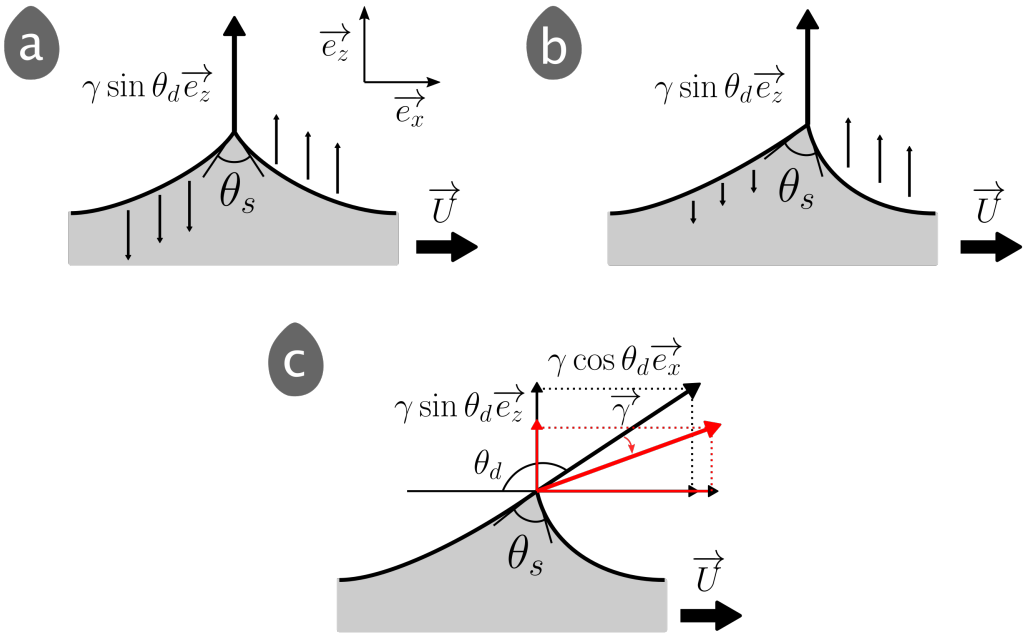

Figure 2.11: **Rotation of the ridge.**Schematic of a wetting ridge, with aperture angle θ_s, moving to the right at a speed $\vec{U}$. We did not represent the liquid/vapor interface. (a) The vertical component of the resulting capillary force pulls the wetting ridge upwards. The left side of the ridge has time to relax if the speed is much slower than the relaxation time of polymers inside the material. The ridge then stays symmetrical. (b) For larger velocities, the ridge starts to rotate. The left side still relaxes as the contact line moves on, albeit not completely. (c) The vertical component of the pulling capillary force $\vec{\gamma}$ decreases when the dynamical contact angle θ_d increases, and so does the height of the ridge.

Recent experiments show that Eq. 2.34 holds at low contact line velocity only. *Karpitschka & al.* [83] measured the dynamic contact angle as a liquid drop spreads on a viscoelastic solid. At low speed, the contact angle does increase with velocity as $\theta_d \propto (U/U_0)^m$. However, θ_d does not follow this scaling as velocity is increased further. The authors attribute this saturation to a maximum rotation of the ridge.

Figure 2.11 provides a tentative explanation for ridge rotation. The key idea is that deformations of a viscoelastic material relax with a delay after stress release. For a moving contact line, the point of application of the pulling force moves with the line. If the line

moves slowly, displacements of the surface behind and in front of the contact line are symmetric (Fig.2.11a), because the trailing part has time to relax completely to its rest state. If the contact line velocity increases (Fig.2.11b), the relaxation of the trailing part is incomplete. Asymmetry in the surface profile appear along the contact line, and the ridge rotates to accommodate these different slopes. Another consequence of ridge rotation is that the surface-normal component of the resulting capillary forces weakens (Fig.2.11c). As a consequence, ridge height is expected to decrease with velocity. Recent measurements confirmed with direct visualization that a dynamic wetting ridge tilts with increasing velocity [86, 87]. However, a thorough experimental investigation of the link between ridge rotation, contact line velocity and contact angle is missing.

Stick-slip

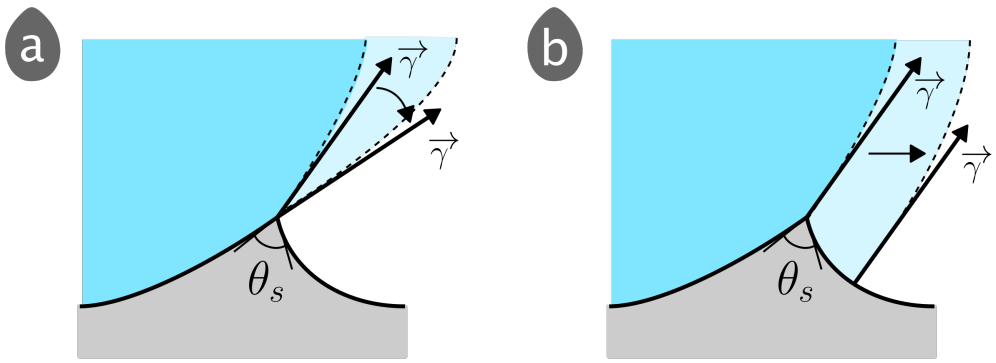

Figure 2.12: ***Stick-slip* motion of an advancing contact line.** (a) "Stick" phase: the ridge pins the contact line and the contact angle increases. (b) "Slip" phase: the contact line depins and slides onto the ridge.

The contact line may also pin and unpin from the solid surface. Several substrates exhibit such irregular motion, despite different rheologies: paraffin gels [88, 89], silicone gels [86] or even thermoplastics [31, 32], to name a few. The contact line carries along the wetting ridge when polymer chains relax faster than the rate at which the liquid spreads, but it pins and depins when these two timescales have similar magnitude. *Kajiya & al.* even propose a regime where the contact line moves so fast that the ridge is mechanically analogue to a pure elastic deformation [88, 89].

X-ray measurements show that pinning intensifies as the ridge grows [86]: a fully-grown ridge bends more and sticks to the contact line for longer times. *Stick-slip* motion highlights that the substrate tunes its response to the rate at which a liquid moves onto it.

Force balance at the tip of the wetting ridge

So far, the results we have presented were obtained under the assumption that the substrate dissipates energy much more than the liquid [27, 30, 44, 53, 54, 79, 81, 83, 86, 87, 90–94]. However, both media dissipate energy in the most general case. A recent theoretical study [62] suggests that the way energy dissipation is distributed between the two phases controls contact line motion in drastic ways.

The description of soft wetting used in ref. [62] is similar to that of ref. [59] in that the surface energy of the substrate is supposed independent of strains and the apex of the ridge is

the locus of a singularity in the strain field. As this model is at the heart of the work presented in this manuscript, we shall describe its fundamental concepts in the following.

We consider a contact line moving on a viscoelastic substrate at speed U, and present a nonlinear theory that describes this situation. As slopes are proportional to $\gamma/2\gamma_s \simeq 1$ in most elastowetting experiments, we need to account for geometric non-linearities. Nonlinear elasticity describes the mechanics behind the transformation of a so-called *reference* configuration into a *deformed* configuration [49, 59, 62]. Coordinates in the deformed state, $\vec{x'} = (x', y')$, depend on coordinates in the reference state, $\vec{x} = (x, y)$, through the displacement field $\vec{u} = (u_x(x, y, t), u_y(x, y, t))$:

$$\vec{x'} = \vec{x} + \vec{u}\,. \tag{2.36}$$

We consider an incompressible linearly viscoelastic material. If we define the stress $\sigma(\vec{x}, t)$ and strain $\epsilon(\vec{x}, t)$ tensors, we have:

$$\sigma(\vec{x}, t) = \int_0^t \mu(t - t')\frac{\partial \epsilon}{\partial t'}\mathrm{d}t' - p(\vec{x}, t)\mathbf{I}. \tag{2.37}$$

Here, the integral over time accounts for memory effects in the material, $p(\vec{x}, t)$ is the pressure field and $\mathbf{I}$ is the identity matrix[3]. $\mu(t)$ is a constitutive law that describes the rheology of the material.

At equilibrium, we have:

$$\nabla \cdot \sigma = \vec{0} \tag{2.38}$$

Incompressibility imposes that:

$$\nabla \cdot \vec{u} = 0. \tag{2.39}$$

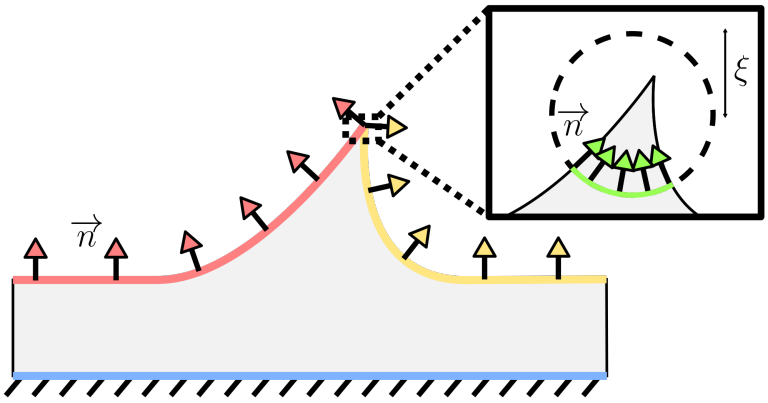

Figure 2.13: **Boundary conditions of a wetting ridge.** The substrate is fixed on a glass slide, the displacement field vanishes (bottom blue interface). The bulk elasticity balances the Laplace pressure at the free surface (red and yellow interfaces). The orientation of the unit vector $\vec{n}$ normal to the solid interface at the tip of the ridge depends on which side we look at. The nonlinear theory in [62] considers a circular arc with radius ξ that encloses the apex of the ridge (inset). The limit $\xi \longrightarrow 0$ regularizes the singularity.

In experiments, the soft sample is bound to a more rigid substrate. Thus, the displacement field vanishes at the layer-substrate interface $y = -H$, represented as the blue interface in Fig. 2.13:

$$\vec{u}\,(x, -H, t) = \vec{0}\,. \tag{2.40}$$

[3] the term $-p(\vec{x}, t)\mathbf{I}$ ensures the incompressibility constraint.

The normal projection of bulk viscoelastic stress balances Laplace pressure at the free surface. Thus we write:

$$\sigma \cdot \vec{n} = \gamma_{sl}\, \vec{n} \cdot (\nabla \vec{n}) \tag{2.41}$$

for the wet (red) interface in Fig. 2.13 and:

$$\sigma \cdot \vec{n} = \gamma_{sv}\, \vec{n} \cdot (\nabla \vec{n}) \tag{2.42}$$

for the dry (yellow) interface. For the sake of simplicity, we assume that the surface tension of the solid has the same magnitude on both sides of the contact line ($\gamma_{sv} = \gamma_{sl} = \gamma_s$). Finally, the boundary condition at the free surface writes:

$$\sigma \cdot \vec{n} = \gamma_s\, \vec{n} \cdot (\nabla \vec{n}). \tag{2.43}$$

Fig. 2.13 highlights that we cannot define a normal vector $\vec{n}$ at the contact line: Eq. 2.43 does not hold anymore, yet the solid might still exert a force at this very point! To calculate it, *Dervaux & al.* sum viscoelastic stresses on the contour of a circular arc that encloses the singular ridge (green line in the inset of Fig. 2.13) and look at the limit of vanishing arc radius ξ. (see inset in Fig. 2.13). We can define a normal vector on this contour without ambiguity, and an infinitesimal length element along the contour of the arc writes:

$$d\ell = \xi d\phi \tag{2.44}$$

in classical polar coordinates (r, ϕ). The corresponding force per unit length exerted by the solid on the apex of the ridge is:

$$\vec{f_s} = \lim_{\xi \to 0} \int_{\xi} \sigma \cdot \vec{n}\, \xi d\phi. \tag{2.45}$$

It remains finite[4] [59, 62].

The force balance right at the contact line then writes:

$$\vec{\gamma} + \vec{\gamma_{sv}} + \vec{\gamma_{sl}} = \vec{f_s} \tag{2.46}$$

where we neglected possible external forces $\vec{f_{ext}}$. When $\vec{f_s} = \vec{0}$, one retrieve the Young-Dupré relation for infinitely rigid substrates, as well as the Neumann condition valid for a liquid substrate (the shear modulus then vanishes). However, both capillarity and viscoelastic stresses contribute to the force balance in general.

General case: both solid and liquid dissipate energy

At order two in $\gamma/2\gamma_s$, and under the assumption $\theta_{eq} = \pi/2$[5], the boundary condition 2.46 writes [62]:

$$-\gamma \cos(\theta_d) = \frac{\gamma^2 \sin^2(\theta_d)}{\gamma_s} (\mathscr{F}_{cap} + \mathscr{F}_{ve}) \tag{2.47}$$

$$-\frac{\cos(\theta_d)}{\sin^2(\theta_d)} = \frac{\gamma}{\gamma_s} (\mathscr{F}_{cap} + \mathscr{F}_{ve}) \equiv \mathscr{A}. \tag{2.48}$$

[4] We should point out that $\vec{f_s}$ depends on the considered situation: at order two in $\gamma/2\gamma_s$, it is purely vertical when a static drop rests on a pre-stretched elastomer [59] and purely horizontal for a moving contact line [62].

[5] This assumption stems from that of equal solid surface tensions on both sides of the contact line, $\gamma_{sv} = \gamma_{sl} = \gamma_s$ [62].

Equation 2.48 balances two restoring forces per unit length of capillary and viscoelastic origin, $\mathscr{F}_{cap}$ and $\mathscr{F}_{ve}$ with the capillary driving force $-\gamma\cos\theta_d$. $\mathscr{F}_{ve}$ represents the force exerted by the solid on the contact line due to the presence of the strain singularity. Both (dimensionless) restoring forces $\mathscr{F}_{\text{cap}}$ and $\mathscr{F}_{\text{ve}}$ depend on the solid capillary number **R**Ca and the ratio between the thickness of the sample and the elasto-capillary length $\Lambda = H/l_s$. In our experiments, $\Lambda \longrightarrow \infty$.

In the general case, the model retrieves the Cox-Voinov law:

$$\text{Ca}\log\left(\frac{x}{x_{\text{min}}}\right) = g(\theta_d(x)) - g(\theta_d(x_{\text{min}})) \tag{2.49}$$

and assumes that the microscopic cutoff angle $\theta_d(x_{\text{min}})$ obeys Eq. 2.48. Capillary and viscoelastic effects set the slope of the liquid/vapor interface below this microscopic cutoff. The model provides the following prediction for the relation between the macroscopic dynamic contact angle and velocity:

$$\boxed{g(\theta_d) = g\left(\frac{\pi}{2} + \arctan\left[\left(\frac{\sqrt{1+\mathscr{A}^2(\mathbf{R}\text{Ca},\Lambda)}-1}{2}\right)^{1/2}\right]\right) + \text{Ca}\log\left(\frac{x}{x_{\text{min}}}\right).} \tag{2.50}$$

The model indicates that a non-dimensional quantity, **R**, describes how dissipation is split between the substrate and the liquid:

$$\boxed{\mathbf{R} \sim \frac{2\mu_0\gamma\tau}{\eta\gamma_s} \sim \frac{\gamma\tau}{\eta l_s}.} \tag{2.51}$$

If we define a capillary number for the solid $\text{Ca}_s = U\tau/\ell_s$ (a definition that slightly differs from that proposed in earlier studies [40, 44, 83]), we have:

$$\text{Ca}_s = \mathbf{R}\text{Ca} \tag{2.52}$$

Here, velocity $U_s \sim l_s/\tau$ describes the velocity associated with viscous relaxation of a soft substrate experiencing capillary forces.

Extreme values of **R** relate to situations in which energy dissipation occurs in a single medium. When $\mathbf{R} \to \infty$, the liquid relaxes much faster than the solid: dissipation takes place in the substrate. On the contrary, when $\mathbf{R} \to 0$, energy is dissipated by the droplet, a situation akin to the case of a rigid substrate.

Figure 2.14a shows the predictions obtained from Eq. 2.50 for different values of **R**. We obtain a Cox-Voinov-like relation at $\mathbf{R} = 0$. Then, increases in **R** lead to curves characterized by a pseudo-plateau for the advancing branch and a short receding branch, that almost disappears at $\mathbf{R} = 10^5$. The latter is reminiscent of $\theta_{dyn}(\text{Ca})$ curves measured on rigid surfaces with defects, when two *a priori* different thresholds in contact angle θ_a and θ_r must be overcome before the contact line either moves or recedes. The difference between these two angles is the contact angle hysteresis. By analogy, we refer to the steepening of the slope around $\text{Ca} = 0$ as soft hysteresis.

A close-up on the region around $\text{Ca} = 0$ shows that this hysteretic response is only apparent (Fig. 2.14b). Contact angles are in fact always varying with Ca. To date, the existence of this apparent soft hysteresis has not been reported. This task is the purpose of the work presented in this manuscript. To do so, we are going to introduce in the next chapter a system based on droplets sliding down an inclined plane. We will highlight how this system should be able to give us the bits of information we hope to obtain.

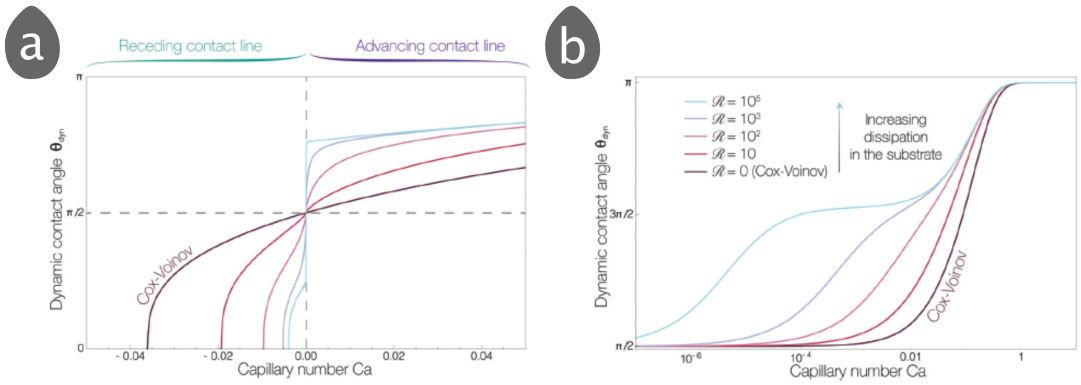

Figure 2.14: **A nonlinear theory predicts soft hysteresis.** (a) Relation between the dynamic contact angle θ_{dyn} and the capillary number Ca as a function of **R** (Eq. 2.51). When the dissipation inside the solid increases (compared with that of the liquid), the slope of the curve steepens. When $\mathbf{R} = 10^5$, the slope is almost vertical, and the curve looks like that of a rigid substrate with a huge hysteresis. The authors call this phenomenon *soft hysteresis*. (b) Close-up on the same curves around the Ca = 0 region. The contact angle at Ca = 0 remains single-valued. Adapted from [62].

Other models

Other descriptions of the wetting ridge exist and lead to a different interpretation of available data. For the sake of completeness, we describe these approaches here. This subsection does not settle which model should be used. Rather, we highlight differences.

Pandey & al. propose another nonlinear elasticity model [49]. This paper accounts for both geometrical and material nonlinearities (they consider a neo-hookean solid just as [59]). However, the key difference is their treatment of the singular ridge: they assume that the stress singularity at the ridge is always weak enough so that the solid contribution $\overrightarrow{f_s}$ vanishes. As a result, the force balance at the tip of the ridge reduces to Neumann's law, e.g. an equilibrium between the surface tensions $\overrightarrow{\gamma_{sv}}$, $\overrightarrow{\gamma_{sl}}$ and $\overrightarrow{\gamma}$.

This different boundary condition leads to a radically different interpretation of the data presented in [51]. This paper considers a drop that rests on a stretched silicone gel, and reports that increasing stretch opens the angle of the ridge θ_s. According to Eq. 2.46, restoring capillary forces (red arrows in Fig. 2.15) and solid contribution (blue arrow) balance the pulling liquid/vapor surface tension (orange arrow). Stretching the gel opens the ridge and reduces the vertical projections of restoring surface tensions. Yet, the force exerted by the solid on the ridge depends on the stretch and compensates for this decrease (Fig. 2.46a). However, without the force of the solid, the only way to balance the pulling force when the ridge opens is to allow a strain dependant solid surface tension: the norm of the restoring capillary forces varies sufficiently with the stretch so the vertical projections balance the pulling force (Fig. 2.15b).

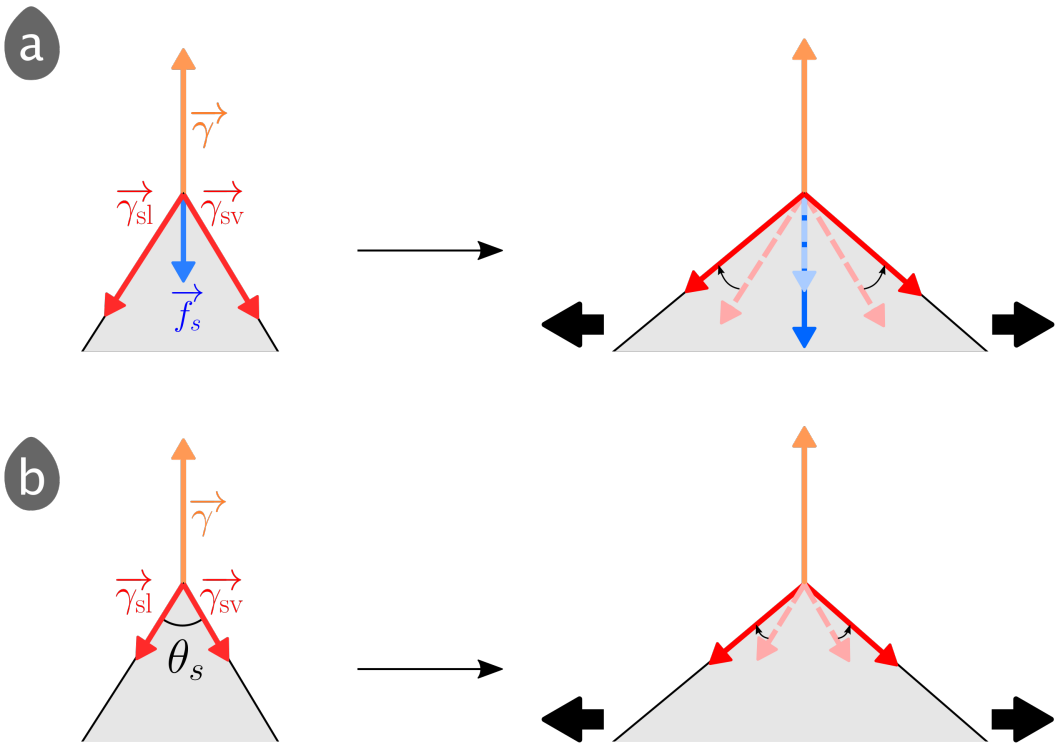

Figure 2.15: **Different interpretations of the opening angle of the ridge θ_s upon stretch.** Stretching a silicone gel widens the wetting ridge [51]. The interpretation of this result depends on the boundary condition at the apex of the ridge. Left: no stretch configuration. Right: stretched configuration. Each time, we display the no stretch state (dashed arrows) on the stretched configuration. (a) The surface tensions of the solid $\overrightarrow{\gamma_{sv}}$ and $\overrightarrow{\gamma_{sl}}$ (red arrows) resist the pulling surface tension $\overrightarrow{\gamma}$ (orange arrow). The vertical component of the resisting surface tensions diminishes as the ridge opens upon stretch. The bulk properties of the substrate (namely elasticity or viscoelasticity) also exert a force $\overrightarrow{f_s}$ at the tip of the ridge (blue arrow). This force depends on the stretch and compensates for the rotation of solid surface tensions. (b) Neumann's condition: only capillary forces balance themselves at the tip of the ridge. Without the bulk solid force, the surface tensions of the solid have to depend on stretch to compensate for the opening of the ridge (the norm of the red vectors increases upon stretch), akin to the Shuttleworth effect.

Chapter 3

How to probe soft hysteresis? Droplets sliding down an incline

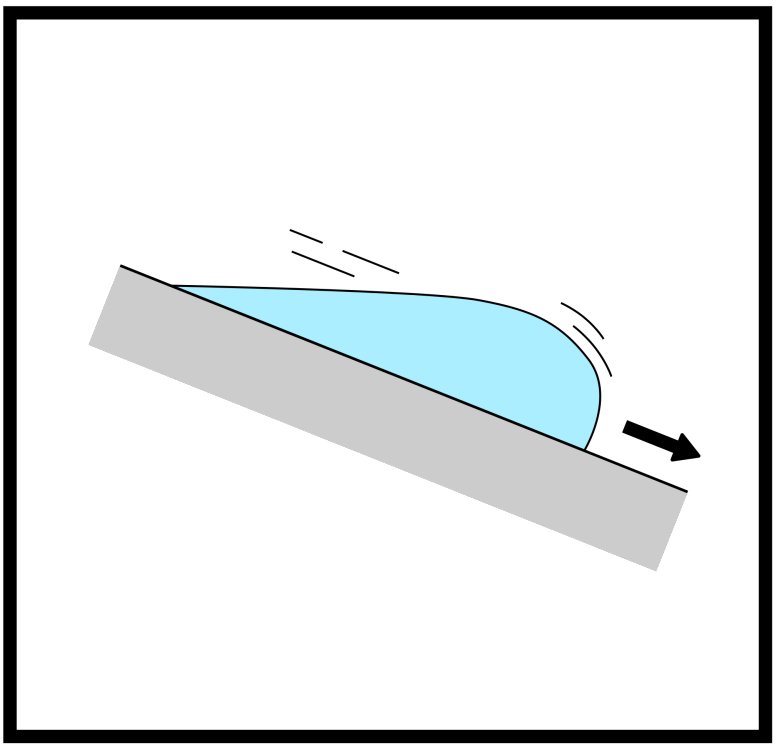

In this chapter, we provide a brief overview of existing literature dealing with droplets sliding on rigid substrates. We highlight the reasons why this system is a good choice to address the question that we intend to deal with.

3.1 Dynamics of sliding drops

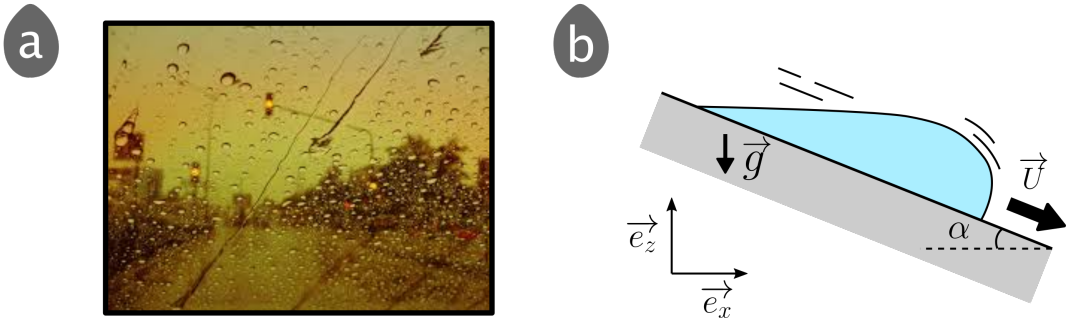

Figure 3.1: **Sliding drops.** (a) Droplets sliding on a windscreen while driving on a rainy day [95]. (b) A schematic of the simplest experiment to study sliding droplets. Gravity $\vec{g}$ sets the drop in motion. The latter slides at speed $\vec{U}$ onto a rigid substrate, inclined with an angle α.

A common occurrence of sliding droplets is observed driving in rainy weather. Rain drops hit the windscreen, and adhere to it. They are then sheared by air flowing around the vehicle. Shear can be strong enough that droplets will start to move (Fig. 3.1a). Here, we will not focus on droplets moving under shear. Rather, we will describe what is known up to now when a droplet runs down an inclined plane under its own weight (Fig. 3.1b).

The fact that the droplet exists on the inclined surface indicates that the liquid partially wets the solid. Wetting is thus characterized by a finite equilibrium contact angle. When a droplet moves down an inclined plane, this contact angle has to adapt following Cox-Voinov's equation (Eq. 2.25). As droplet velocity increases with the inclination angle α, we expect that deviations of the contact angle away from its equilibrium value increase as α increases. Moreover, the angle between the contact line around the droplet and the direction of droplet motion varies with the position along the perimeter of the droplet, and part of the contact line is advancing while the other is receding with respect to the substrate. All in all, we can expect a rich shape diagram as well as interesting dynamics.

Podgorski et al. were the first to study systematically droplets running down an inclined plane [96]. Since then, the topic has received constant attention [71,73,74,77,96–98], in part because of its relevance to water drainage during dew collection and also because some of its features such as the shape of the trailing edge of the droplet puzzled scientists. In these studies, the authors investigate how silicon oils slide on a fluoropolymer-coated glass slide. We refer to their system as {FC725; silicon oil} (FC725 is the name of the fluoropolymer). The equilibrium contact angle in their system is roughly 45°, and recent work has shown that the fluoropolymer coating they use does not add dissipation to the system [99]. These studies document the phase diagram of sliding droplets with volumes ranging from 2 to 20 µL and indeed show that shape is dependent on velocity U (Fig. 3.2a). The droplet is axisymmetric at low velocity. As velocity increases, the trailing edge of the droplet takes the shape of a corner that becomes narrower as U increases. Beyond a critical velocity, the droplet leaves tiny droplets, referred to as pearls, in its path. The properties of the pearl pattern depend

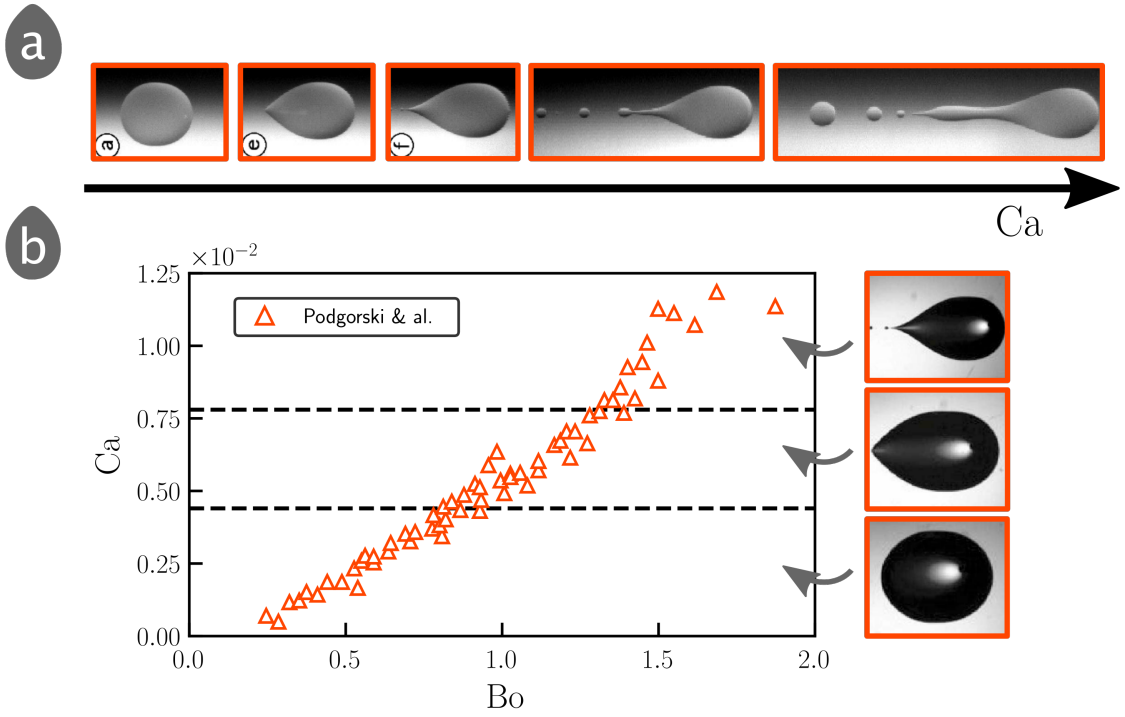

Figure 3.2: **Drops sliding onto a rigid substrate: shape diagram.** (a)Rounds, corners then pearls: the drop becomes asymetric with increasing speed. (b) Bo and Ca describes the linear relationship between the weight and the running speed. Here we kept their definition for the Bond number: $\mathrm{Bo} = ((\mathrm{V}^{\frac{1}{3}}/\lambda_c)^2 \sin\alpha$ where V is the volume of the drop. Data taken from [96, 97], pictures taken from [74].

on U: just above the instability threshold, we observe single-sized and evenly-spaced pearls, while the pattern becomes more intricate as U increases further (two last pictures in Fig. 3.2a).

The balance between injected and dissipated power in this system should be captured by Eq. 2.31 that predicts that the capillary number of the experiment is proportional to its Bond number. This prediction is supported by experimental data (Fig. 3.2b). One interesting aspect of this plot is that we observe a threshold value for the Bond number that must be overcome to set the droplet in motion. This threshold value is a consequence of contact angle hysteresis $\Delta\theta$, suggesting that Eq. 2.31 should be rewritten [97]:

$$\mathrm{Ca} \sim \mathrm{Bo}\sin(\alpha) + \mathrm{Bo}_m \tag{3.1}$$

with $\mathrm{Bo}_m = -\Delta\theta$.

An investigation of the flow inside a running droplet provides interesting insights into the mechanism behind corner formation. Figure 3.3a highlights that the velocity field inside a droplet is oriented normal to the contact line as liquid approaches it and moves away from it to reconnect to the flow in the center of the droplet that is directed along the symmetry axis of the droplet [73]. This feature holds for cornered drops (Fig. 3.3b). [100] and helps to understand the appearance of the corner. The trailing-edge contact line makes an angle with the direction of motion so that it can move at a slower velocity. This idea was initially formulated in the context of dip-coating[1] by Blake and Ruschak [101]. Eventually, velocity becomes too high and the droplet leaves the pearls we mentioned earlier in its trail.

[1]Dip-coating allows to coat a solid with a thin liquid layer by moving the plate out of the liquid bath very

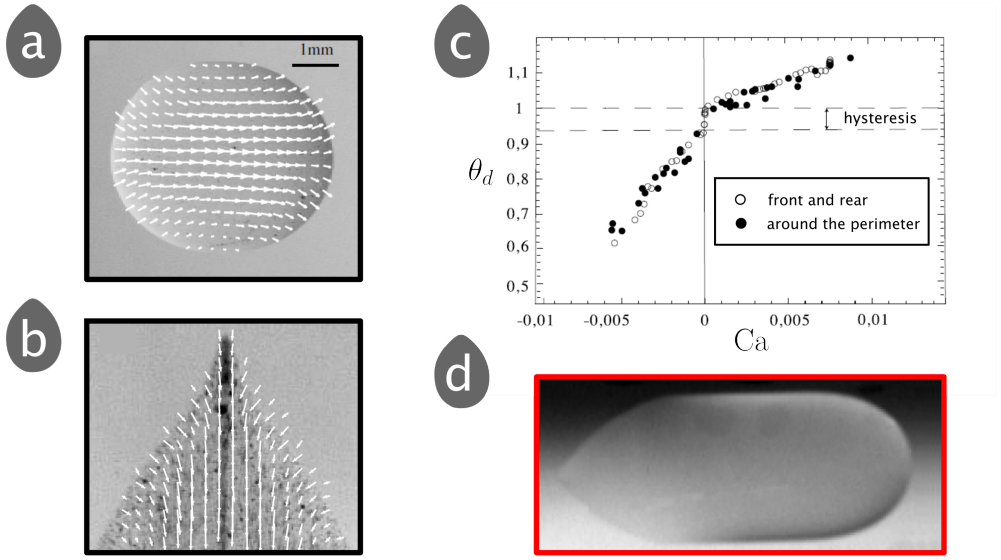

Figure 3.3: **The speed normal to the contact line matters.**Velocity field for a (a) round and (b) corner-shaped drop. Pictures taken from [73] In both cases, the flow stays normal to the contact line. (c) The relationship between dynamic contact angles θ_d and the capillary number Ca holds all along the drop if we consider the speed normal to the contact line $\overrightarrow{U_\perp}$. Data taken from [73]. (d) Water drop sliding onto a plastic sheet [96]. Zero-speed contact lines are parallel to the motion of a sliding drop. Very long drops (the field of the camera is about 3 cm) stem from huge hysteresis (70° here).

Accounting for the fact that flow is oriented normal to the contact line everywhere, we expect Cox-Voinov's relation (Eq. 2.25) to hold provided we correct the velocity with a function of the angle the contact line makes at the point of measurement with overall droplet motion. Figure 3.3c confirms that measurements of contact angles all along a single drop and measurements at the front and the rear of several drops collapse on a master curve. It implies that you can deduce the contact angle distribution all along a drop from this law by taking the angle value corresponding to the local projection of the overall speed normal to the contact line. The agreement with Eq. 2.25 is more difficult to ascertain due to the significant influence of contact angle hysteresis. Indeed, the latter separates the advancing contact angle branch from the receding one by a gap (Fig. 3.3c). In this gap, the contact line is static. The contour of the droplet forms a straight line where contact angles fall in the hysteresis, the larger the gap, the longer the drop. A spectacular example of this effect can be found in T. Podgorski's PhD manuscript (p. 92 in ref. [96], reproduced in Fig. 3.3d).

3.2 The corner: a probe for molecular scales?

The formation of corners at the trailing edge of the droplets is one of the most striking results of the study of sliding droplets. As we have just seen, we can understand why the receding contact line makes an angle with the direction of motion. This rationale does not provide a full understanding of the physics behind the properties of the corner. In particular, curvature selection at the tip of the corner has attracted attention as it seems to be related to molecular length scales.

fast.

A zoom on the trailing edge of the drop (Fig. 3.4a and b) indicates that the radius of the curvature R_{curv} of the corner is small, of the order of a few tens of micrometers. A plot of R_{curv} against the capillary number Ca (or its inverse, as we do here for a reason that will become clear soon) shows that the radius of curvature diverges as the droplet approaches the pearling instability threshold, *i.e.* for small values of Ca^{-1}. Thus, cornered droplets seem to combine two singularities at their trailing edge, one related to stresses and another one related to geometry.

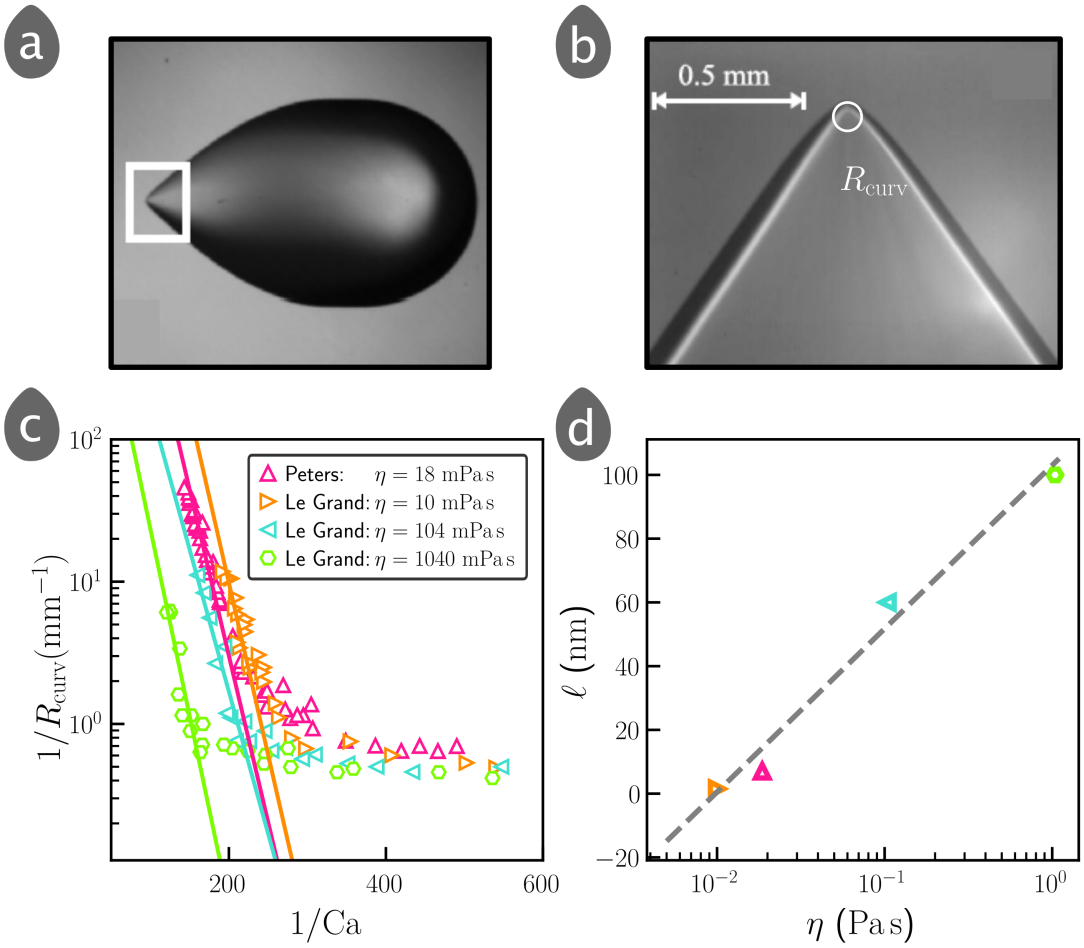

Figure 3.4: **Sharpness of the tip.** (a) Corner-shaped drop. (b) The tip becomes round at an appropriate zoom (white circle). R_{curv} is the corresponding radius of curvature. (c) The rear curvature increases exponentially close to pearling. The exponential fit according to Eq. **3.2** (solid lines) gives a cutoff length ℓ that regularizes the corner. (d) This microscopic cutoff increases logarithmically with dynamic viscosity η. Data from [71, 74, 98], pictures from [98].

Peters & al. investigated how the radius of the apex R_{curv} decreases when Ca increases [98]. Balancing capillarity versus viscosity and assuming that the dynamic contact angle at the receding contact line is equal to the static receding contact angle $\theta_{s,r}$, they propose the following scaling to describe their experimental data [102]:

$$\boxed{R_{curv} \sim \ell \exp\left(\frac{\theta_{s,r}^3}{Ca}\right),} \tag{3.2}$$

where the microscopic cutoff length scale ℓ regularizes the divergence of the curvature at the

tip. Their data suggest that regularization occurs at the molecular scale, $\ell = 8$ nm. They liken ℓ to the microscopic cut-off length that appears in the Cox-Voinov relation to avoid stress divergence.

Equation 3.2 is really tested on a single dataset. We can try to apply it to other datasets that exist in the literature. For example, the same approach on *Le Grand & al.*'s data [71, 74] questions the nature of ℓ. These authors used the same physico-chemical system ({FC725; silicon oil}) as *Peters et al.*, and they investigated different viscosities. Length scale ℓ increases with η up to 100 nm (Fig. 3.4d). If we still assume that this length scale is of molecular origin, its order of magnitude is compatible with the length of extended polymer chains. However, this interpretation has two issues. First, stretched polymer chains want to return to their equilibrium state. Hence, stress should appear in a fluid near the contact line that should modify the stress balance and possibly the shape of the droplet there. However, as we have seen, dynamic contact angles are well described by the Cox-Voinov relation [71]. Besides, experiments comparing different kinds of polymer melts during the spreading of droplets found that the shape of PDMS droplets is described by the Cox-Voinov relation while the same relation cannot capture the shape of droplets of other polymeric liquids [103]. Thus the physics involved in setting the properties of sharp-cornered drops remains to be identified and it is an open question up to now.

3.3 Motivation of our study

We have indicated at the end of chapter 2 that a model developed recently suggests that the relation between the dynamic contact angle measured at a contact line and its velocity depends on the partition of dissipation between the solid and the liquid. Testing this prediction would benefit from the use of a system where dynamic contact angles can be measured in the receding and advancing regimes at the same time. We have just seen that droplets sliding down an inclined plane provide such a solution. Not only would they allow us to gain insight in the ability of our model to predict the dynamics of wetting on soft substrates, but the fact that these systems have not been explored in the context of soft wetting is expected to bring new insights into other issues such as curvature selection at the trailing edges of cornered drops.

In the following part, we describe the materials and methods that we relied on to carry out our study. Chap. 4 details the fabrication of silicone gels. Also, we explain how we rely on **R** to pick out an elastowetting system. We provide a description of both the setup and the protocol we use to study sliding drops experiments in Chap. 5. The third part describes our results and observations.

Chap. 6 provides the shape diagram of several elastowetting systems and highlights that the dissipation ratio impacts the observed shapes. Chap. 7 investigates to what extent **R** impacts the dynamics. First, it tackles the problem at the scale of the drop and looks for the relation between the weight of the drop and its running speed. Then, it tackles the problem at the scale of the contact line and look for the relation between the dynamic contact angle and the speed. We compare quantitatively our results with the nonlinear theory in Chap. 8. Finally, Chap 9 provides preliminary results and suggests that the shape of the drop depends also on the elastocapillary length.

Part II

Materials and Methods

Chapter 4

Materials

Before introducing the materials we used to perform our experiments, we provide the reader with a quick reminder of polymer physics. Then we will also introduce the liquids we used and justify their choice based on the requirements we need to fulfil to test the prediction described at the end of Chap. 2.

4.1 Polymer physics: a reminder

In this section, we describe the properties of polymeric materials that will be useful to us for the analysis of our results. The reader interested in a more complete description may look at refs. [104–107].

4.1.1 Polymers are macromolecules

Identical subunits, called monomers, can be bound together and form a much longer macromolecule (Fig. 4.1a). If the macromolecule is long enough, its properties result from the statistical arrangement of monomers in space with respect to each other, and the macromolecule is then a polymer. These macromolecules are ubiquitous: plastics as much as DNA are polymers.

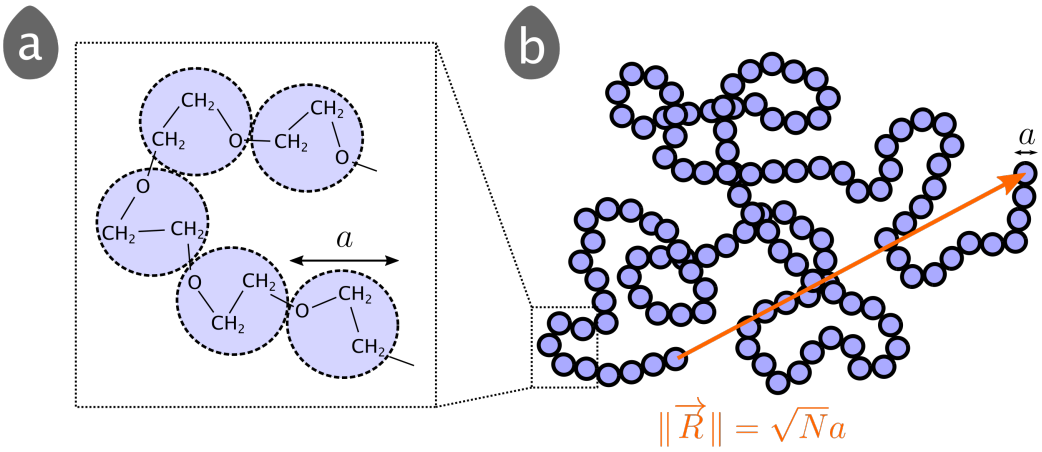

Figure 4.1: **An ideal polymer molecule.** (a) The succession of N identical molecular patterns of length a, called monomers, forms a polymer chain. We draw a poly(ethylene glycol), whose chemical pattern is C_2H_4O. (b) A chain coils with an end-to-end vector $\vec{R}$ in its preferred state. The ideal chain neglects any interaction between monomers and states: $\|\vec{R}\| = \sqrt{N}a$.

At rest, and because of Brownian motion, polymers usually coil. Thus, their effective size is far lower than their total unfolded length (Fig. 4.1b). The end-to-end radius $\vec{R}$ (orange arrow in Fig. 4.1b) characterizes the typical size of a coiled polymer that contains N monomers of size a. The simplest way to scale $\vec{R}$ is to neglect any interactions between monomers so that they can take any orientation regardless of their neighbours – this is the *ideal chain* model:

$$\|\vec{R}\| = \sqrt{N}a. \tag{4.1}$$

Now, what happens if we grab a polymer chain by its two ends and pull on them? Doing so, we break spatial isotropy with respect to position fluctuations for the monomers. From

the standpoint of the chain, some of its configurations become inaccessible: the entropy of the chain decreases. Therefore, the stretched polymer chain will pull back and exert a force to go back to its rest state. Polymers are often referred to as "entropic springs" because of their peculiar brand of elasticity.

4.1.2 Gels and elastomers

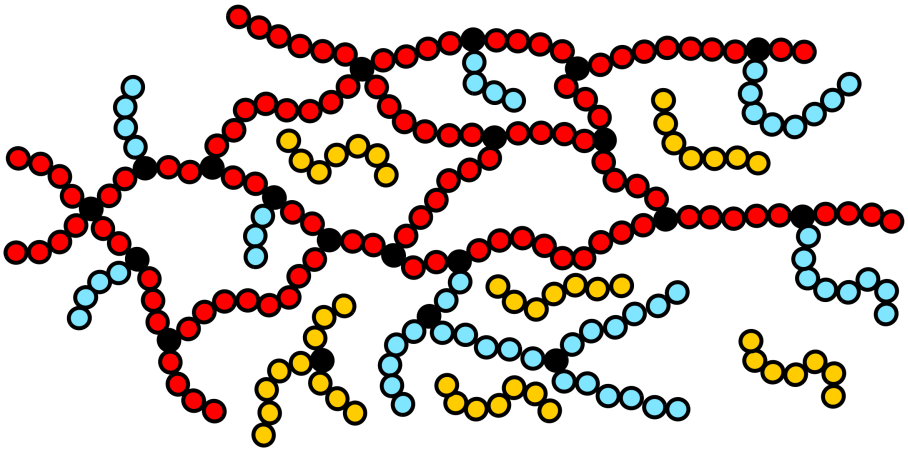

Figure 4.2: **Cross-linked polymers.** Polymers cross-link either by both ends (red chains), one end (blue chains) or not at all (yellow chains) to form a viscoelastic material. Black dots represent reticulation sites. The red chains contribute to the elastic network. Dangling (blue chains) uncrosslinked structures (yellow chains) contribute to the viscous properties of the material. Both may exhibit ramifications. Thermal fluctuations stir the whole structure.

Polymer chains can be connected to form a macroscopic macromolecule. This process is often called "cross-linking". They may bond via chemical reactions as well as other physical interactions (hydrogen bond, microcrystallisation upon cooling, etc...) [105, 107]. Materials scientists pool efforts to control both structure and interactions inside the material, and tailor materials with interesting properties: among others, let's cite self healing [108] and extremely strong hydrogels [109] that hold promise in mimicking biological tissues [110]. Liquid inclusions smaller than the elastocapillary length inside the network may also stiffen the material [111]. The shear stress of polymer networks remains proportional to strain over a large range of strain. Their rupture occurs at strains of $500-1000\%$. In comparison, strains of 1% damage hard solids such as steel [112].

While polymeric liquids will flow, cross-linking prevents macromolecules in the network from moving with respect to each other, conferring solid-like properties to the material: elastic chains can store energy upon stress [104, 113]. If the density of cross-linking sites ν is small, elasticity still originates from entropy [107]. The shear modulus of these materials increases with an increase of ν and a decrease of the number average molecular weight M_s:

$$\mu_0 = \frac{\rho \mathcal{N}_A k_B T}{M_s} \tag{4.2}$$

where ρ is the volumic mass of the material, $\mathcal{N}_A$ is the Avogadro number, k_B is Boltzmann's constant, T is temperature [112]. When put under stress, these materials will respond viscoelastically: they will reach finite strain, but with a certain kind of dynamics that comes from the fact that polymers rub against each other and dissipate energy.

In practice, cross-linking is never perfect (Fig. 4.2). Some chains are free to move while others dangle from one of their ends. They might relax and/or flow through the network upon stress [104, 113] and also contribute to the mechanical response via viscoelastic or poroelastic contributions [114].

4.2 Preparation and characterization of silicone gels

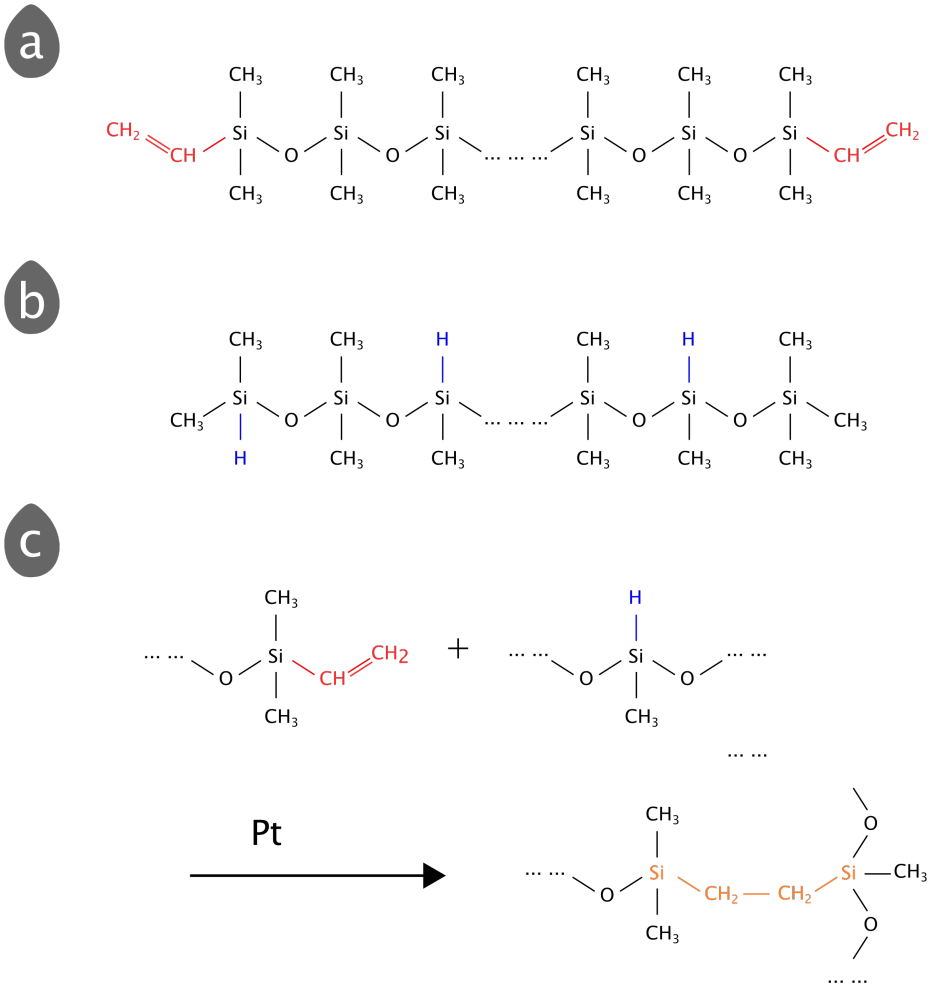

Figure 4.3: **Addition cure reaction.** (a) Vinyl-terminated poly-(dimethylsiloxane) (PDMS) reacts with (b) hydride-terminated poly-(dimethylsiloxane) in presence of a platinium catalyst Pt. Red (respectively blue) chemical groups correspond to vinyl (respectively hydride) terminations. They cross-link to form the Si – CH_2 – CH_2 – Si group (in orange) (c).

4.2.1 Protocol

We manufactured silicone gels (poly-(dimethylsiloxane), abbreviated to PDMS) using a commercial kit (Dow Corning, SYLGARD™ 527). This addition cure system [115] is sold as a two-part kit. The first part, usually referred to as part A, contains vinyl-terminated poly-(dimethylsiloxane) (Fig 4.3a); the second part, usually referred to as part B, contains a platinum-

based catalyst and silicone oligomers with hydride bonds (Fig 4.3b). Mixed together and heated, vinyl groups (in red) and hydride bonds (in blue) react and form $Si-CH_2-CH_2-Si$ chemical bonds (in orange, Fig. 4.3c) [116, 117]. Ref. [118] gives an example of how the platinum catalyst reacts in this multi-step hydrosilylation reaction.

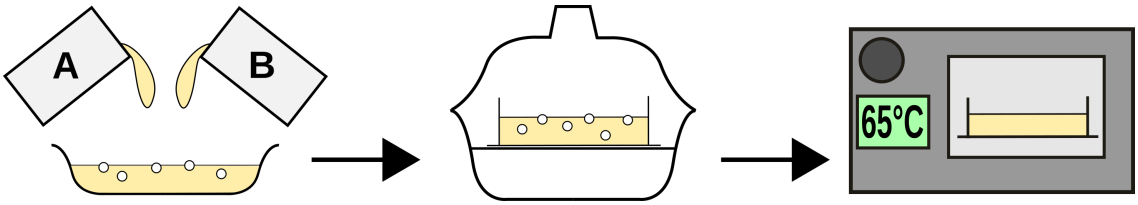

Figure 4.4: **Key steps for silicon sample preparation.** First, we mix both parts of the commercial kit at recommended ratio. Second, we pour the mixture into the desired mold and remove bubbles (represented as small white dots) in a vacuum atmosphere. Then, we bake it overnight.

All tools we use in the following are rinsed with ethanol and distilled water before use. Vessels are also vacuum-dried. This process minimizes contamination of the sample by dust and impurities that could modify the surface properties of silicone layers.

The schematics in Fig. 4.4 provide the key steps of sample manufacturing. Both parts of silicone gel commercial kit are mixed at the recommended ratio ((1:1) for SYLGARD™ 527) in a weighing boat. Next, we pour the mixture into clean vessels (Caubère, 60×40 mm^2, polystyrene). The thickness of the sample is $h_s = 4$ mm, and we do not expect finite-depth effects [44]. We place the mixture in a vacuum chamber for 2 h to remove air bubbles entrapped during mixing. Finally, the sample is let to cross-link in an oven at 65 °C overnight (approximately 15−18 h). We checked the surface of the samples after cross-linking as marks sometimes appeared for a reason that still eludes our understanding. We carried out experiments on unmarked layers.

4.2.2 Gel rheology

Rheology measurements

We characterize the rheology of SYLGARD™ 527 with a stress-controlled rheometer (MCR 501 d'ANTON PARR) with plate-plate geometry (diameter $d = 25$ mm). We prepare silicone disks of thickness $h_s = 4$ mm and whose area matches that of the plate tool of the rheometer. Samples are characterized *via* a small-amplitude oscillatory shear test (SAOS). This test consists in applying a time-periodic strain $\epsilon(t) = \epsilon_0 \sin(\omega t)$ to the solid. The amplitude $\epsilon_0 = 0.1\%$ is kept constant while the angular frequency ω varies over several orders of magnitude. The rheometer returns the stress σ measured as a function of pulsation ω. We check that this measurement is independent of ϵ_0. Thus we are in the linear regime, where measured stress is proportional to applied deformation.

We extend the pulsation range over which we perform SAOS tests by using the time-temperature superposition procedure [104, 106, 107]. This procedure relies on the fact that, in general, the ratio of the polymer relaxation timescale τ_p to the measurement timescale τ_m, known as the Deborah number De, is a good indicator of the mechanical response of polymer chains [106]:

$$\mathrm{De} = \frac{\tau_p}{\tau_m}. \tag{4.3}$$

As τ_p depends on temperature T, we expect that we can explore the rheology of polymeric materials by changing temperature. Taking this assumption to be true, we hypothesize that

measurements of σ at (T_1, ω_1) and (T_2, ω_2) are equivalent provided they have the same De. Hence, performing several rheological measurements on the same pulsation range at different temperatures is equivalent to one rheological measurement at a single temperature on an extended pulsation range. We apply shift factors a_T (along the pulsation axis) and b_T (along the complex modulus axis[1].) to collapse the measurements at different temperatures on a single master curve. This procedure allows us to access the mechanical response of the material at unattainable pulsations ω by changing temperature.

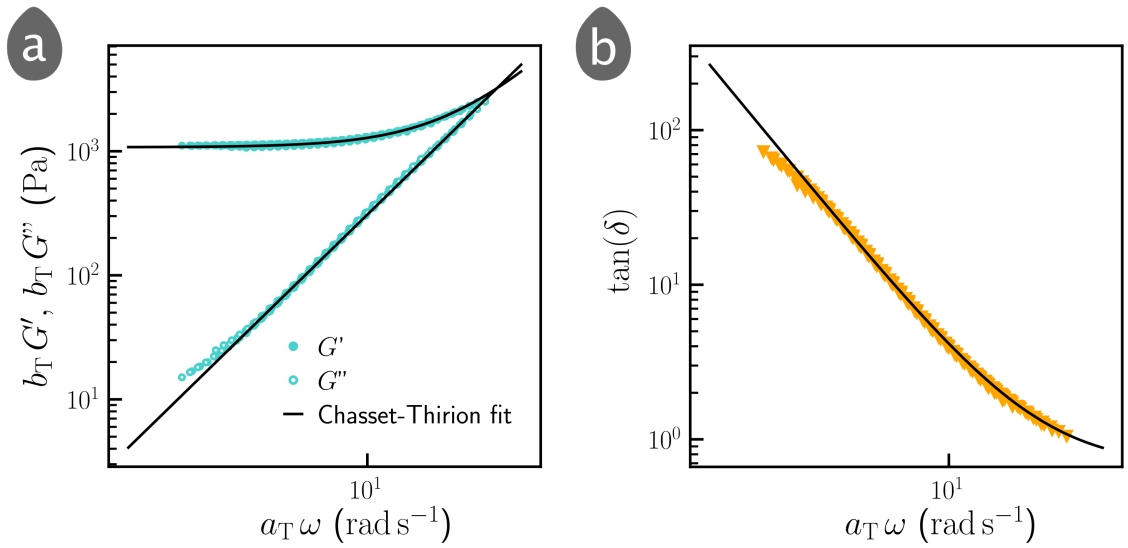

Figure 4.5: **Rheological properties of SYLGARD™ 527 .** Rheology of our silicone gel (SYLGARD™ 527). We used the time-temperature superposition procedure. We plot the frequency dependence of (a) the elastic G′ and loss G" modulii, and (b) the loss factor tan(δ). a_T and b_T are the shift factors necessary to collapse all the measurements at different temperatures on a master curve. The Chasset-Thirion model (solid line) fits experimental data (symbols). We find $\mu_0 = 1.077$ kPa, $\tau = 18.2$ ms and $m = 0.626$.

Figure 4.5a shows the results of this characterization. Temperatures range from T = −30°C to T = 50°C by steps of 10°C. Note that the temperature of our samples is always much larger than the glass transition temperature of PDMS, $T_g = -126$ °C [113]. We extract mechanical parameters of the sample by fitting the Chasset-Thirion model (Eq. 2.32) to the data. We retrieve from eq 2.32 the elastic and loss modulii G′(ω) and G"(ω):

$$G'(\omega) = \mu_0 \left(1 + \cos\left(\frac{m\pi}{2}\right)(\omega\tau)^m\right) \tag{4.4}$$

$$G''(\omega) = \mu_0 \sin\left(\frac{m\pi}{2}\right)(\omega\tau)^m. \tag{4.5}$$

We want to extract the shear modulus μ_0, the relaxation time τ and the exponent m from fits of Eqs. 4.4 and 4.5 to the data. We first remove μ_0 from the fits by focusing on the inverse of the loss factor $\tan\delta = G''/G'$ (Fig. 4.5b):

$$\frac{1}{\tan(\delta)} = \frac{G'}{G''}(\omega) = \frac{1}{\sin\left(\frac{m\pi}{2}\right)(\omega\tau)^m} + \frac{1}{\tan\left(\frac{m\pi}{2}\right)}. \tag{4.6}$$

[1]Actually, temperature-dependant prefactors also induces a vertical shift. Because polymer chains are "entropic springs", elastic modulii are proportional to $n(T)k_BT$ where n is the number of polymer chains per unit volume at temperature T and k_B is the Boltzmann constant [104, 107]. Changes in temperature also change $n(T)$ and a correction is usually necessary here too.

to our experimental data. Then, we inject the values of τ and m in equations 4.4 and 4.5 and fit experimental data of Fig 4.5a to find μ_0. We see that the fits capture very well the experimental data (Figs. 4.5a and b). We find that SYLGARD™ 527 has a shear modulus μ_0 = 1.077 kPa, a relaxation time τ = 18.2 ms and an exponent m = 0.626.

The exact formulation of the kit is unknown. We know from the datasheet that the viscosities of each part of the kit are around 500 mPa s. Assuming that the silicone polymers used in the kits are linear macromolecules, we deduce from these viscosities that their molecular weight is of the order of 10^4 g mol^{-1}, comparable to the entanglement molecular weight [119]. In this case, the shear modulus of a fully cross-linked PDMS sample containing no solvent is always greater than 200 kPa. The low value of μ_0 for SYLGARD™ 527 suggests that the density of cross-links is low. This could be the case if the sample contains a lot of free polymeric chains. To test this, we carry out chain extraction.

4.2.3 Free-chain extraction

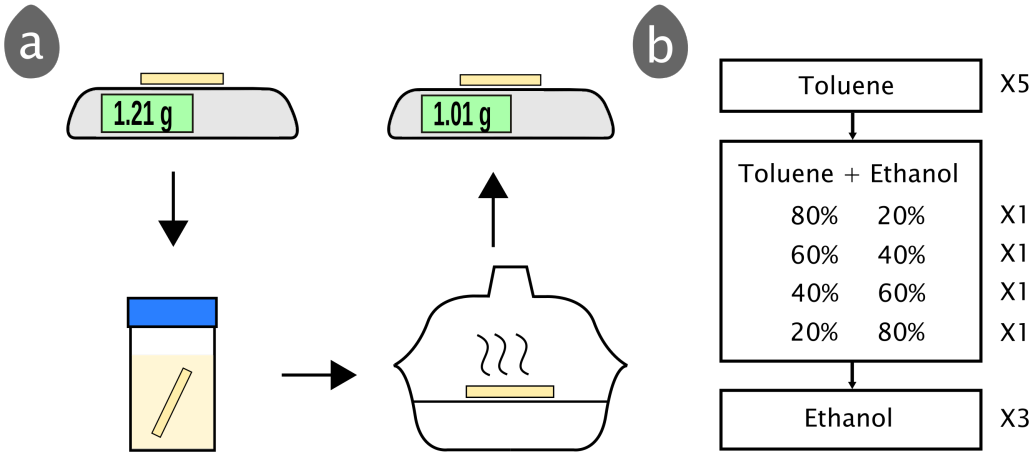

Figure 4.6: **Free chains extraction.**(a) Key steps of free-chain extraction. First, we weigh a piece of PDMS. Second, we dip it into several consecutive baths of good solvent (toluene) and bad solvent (ethanol) for PDMS to remove free chains. Third, we remove the remaining solvent under a vacuum atmosphere. Finally, we weigh again the PDMS sample. The difference between the initial and final masses gives the amount of free chains. (b) Number and type of liquid baths. First, we used toluene that swells PDMS and removes free chains. We progressively added ethanol that is miscible with toluene and do not swell PDMS. The last baths are in pure ethanol.

To quantify the amount of free chains in our samples, we need to extract them with the procedure described in figure 4.6. The core idea is to dip a piece of gel in a good solvent (toluene) then in a bad solvent (ethanol). The two solvents need to be miscible. Toluene will swell PDMS, and free chains can diffuse out of the gel without any energy cost. Then, we remove the sample from its toluene bath and place it in an ethanol bath. Ethanol does not penetrate in the sample, but toluene leaves the latter to mix with the new solvent. Fig. 4.6b details the numbers and types of solvent baths. The first baths to extract toluene use mixtures of toluene and ethanol to avoid sample degradation because of the shock in solubility if pure ethanol is used straight away. The mass loss gives the amount of free chains (we remove remaining solvent under a vacuum atmosphere before final weighing). SYLGARD™

527 contains about ~ 60 wt% free chains. For the sake of comparison, we performed a similar procedure on samples of CY 52-276 , a silicone kit used in the community. We find that it contains around 54 wt% free chains.

The presence of free chains may have consequences on the surface state of the droplet [92]. We will account for this issue and check for its possible consequences when we will describe and analyze our results.

4.3 Characterization of liquids

To circumvent the fact that gel properties τ, μ_0 and m are difficult to control independently, making it difficult to tune **R** from the solid side, we use different liquids. These liquids allow us to vary η by orders of magnitude while γ stays of the order of several tens of $\mathrm{mN\,m^{-1}}$. These liquids have long names, and Table 4.1 indicates the acronyms we use.

Acronym	Complete name
U90	Ucon™Lubricant 75-H-90,000
PEG-*ran*-PPG-ME	poly(ethylene glycol-*ran*-poly propylene glycol) monobutyl ether
PEG-*ran*-PPG-ME70	70% poly(ethylene glycol-*ran*-poly propylene glycol) monobutyl ether in water solution
PEG-*ran*-PPG	poly(ethylene glycol-*ran*-poly propylene glycol)
G100	Glycerol
G60	60% Glycerol in water solution

Table 4.1: **Acronyms of the liquids used.**

4.3.1 Rheology

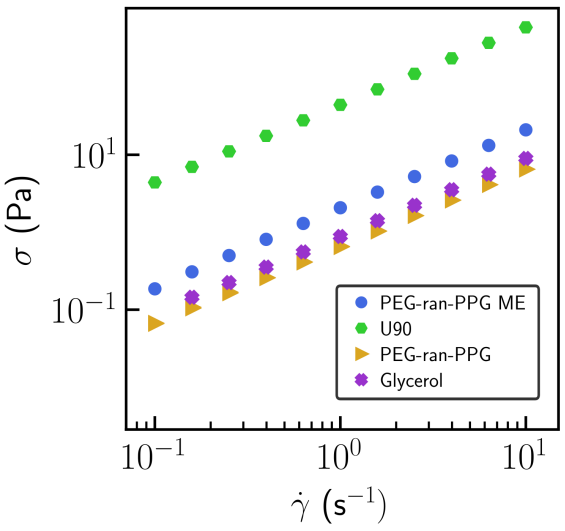

Figure 4.7: **Newtonian behaviour of the liquids used**. Measurement with a rheometer. Linear relationship between stress σ in function of shear rate $\dot{\gamma}$ indicates a Newtonian behaviour.

We measure the mechanical response of glycerol, Ucon oil and the two types of poly(ethylene glycol) (PEG-ran-PPG ME and PEG-ran-PPG) with a strain-controlled rheometer (Ares G2; TA Instruments). We use a parallel-plate geometry (PP25; TA Instruments) and set the gap at 1 mm and temperature at T = 25 °C. We obtain a linear relationship between the stress σ and the strain rate $\dot{\gamma}$ for all liquids (fig. 4.7). The viscosity of these liquids is hence constant, and they are Newtonian.

To account for day-to-day temperature and humidity variations, we measure the dynamic viscosities η with capillary viscosimeters sitting next to the experimental set-up every day. Table 4.2 references mean values and standard deviations for each liquid.

Liquid	η (Pa s)
U90	$(3.69 \pm 0.69) \cdot 10^{1}$
PEG-*ran*-PPG-ME70	$(8.42 \pm 0.99) \cdot 10^{-1}$
PEG-*ran*-PPG	$(4.91 \pm 0.34) \cdot 10^{-1}$
G100	$(6.31 \pm 1.04) \cdot 10^{-1}$
G60	$(6.8 \pm 0.23) \cdot 10^{-3}$

Table 4.2: **Liquid viscosities** Dynamic viscosity η values obtained with capillary viscosimeter during sliding experiments.

4.3.2 Density measurements

For each liquid, we weigh a volume of 10 mL with a 0.01-g-accurate scale. The last significant digit is taken as the measurement error for the mass. We also take an error of 0.5 mL in the injected liquid volume. Table 4.3 sums up our measurements. The values for G100, G60 and U90 are consistent with the value of the manufacturer or what can be found in the literature [120–122].

Liquid	ρ (kg m^{-3})
U90	$(1.08 \pm 0.05) \cdot 10^{3}$
G100	$(1.27 \pm 0.06) \cdot 10^{3}$
PEG-*ran*-PPG-ME70	$(1.05 \pm 0.05) \cdot 10^{3}$
PEG-*ran*-PPG	$(1.05 \pm 0.05) \cdot 10^{3}$
G60	$(1.16 \pm 0.06) \cdot 10^{3}$

Table 4.3: **Densities of the liquids we use.**

4.3.3 Surface tension measurements

We measure surface tensions with the *pendant-drop* method. A syringe pump injects liquid little by little through a glass pipet (Fig. 4.8) up to the point where the droplet is about to detach from the pipette tip. In this case, the shape of the droplet results from a balance between capillarity and gravity. Then, we fit the surface profile of the drop with an ImageJ/FiJi plugin [123] that returns the surface tension as a fitting parameter. For each liquid, we repeat the experiment 3 to 5 times. We take the standard deviation as the error bar. Table 4.4 summarizes measurements.

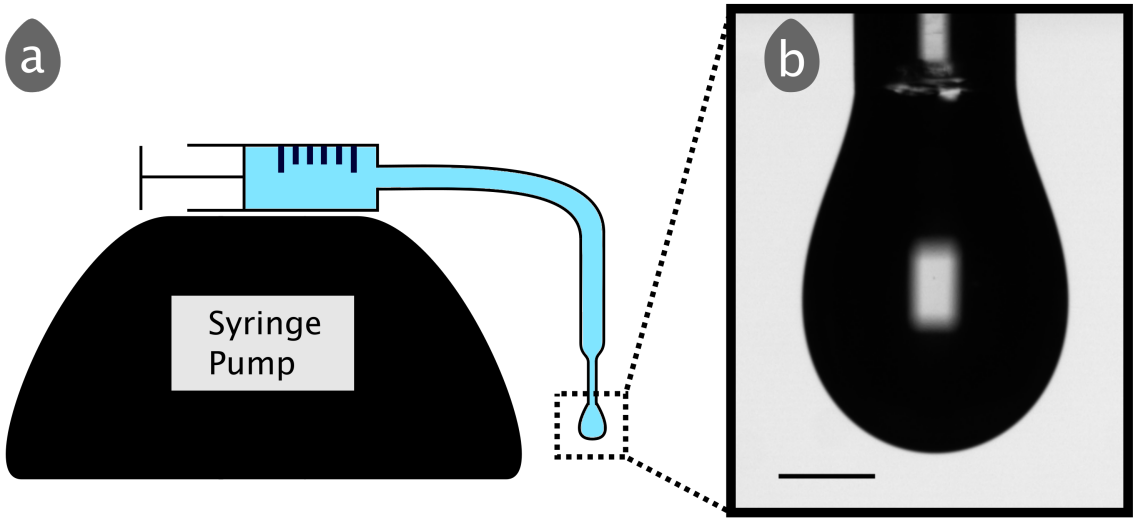

Figure 4.8: **Pendant drop setup.**(a) A syringe pump injects the desired amount of liquid through a Pasteur pipette. (b) Photograph of the pendant drop. Scale bar: 1 mm.

Note that it is difficult to reach equilibrium shape for viscous drops: they may relax for hours and evaporate or absorb water from the surrounding atmosphere [124]. In that case, we focus on slowly falling drops, which we assume to be in a quasi-static regime. We think our measurements are still valid because:

- falling speed U_f was slower than characteristic speed $U_l = \gamma/\eta$ for each liquid (for instance, it is 100 times smaller for PEG-*ran*-PPG-ME70), which suggests that viscous effects do not modify the shape of the drop;
- we double-check surface tension values with higher U_f measurements and found identical results;
- glycerol and PEG-*ran*-PPG-ME measurements are consistent with available in the literature.

Finally, we are somewhat surprised by the low surface tension of the glycerol-water solution. We expect it to be larger than that of pure glycerol given that we add water, but that is not the case. Also, the value we find for U90 is smaller than that given by the manufacturer.

Liquid	γ_{LV} (mN m^{-1})	γ_{LV} manufacturer
U90	40.7 ± 0.9	50.9 [121]
G100	63.1 ± 0.5	63.4 [120]
PEG-*ran*-PPG-ME	37.1 ± 0.4	36.0 ± 0.1 [125]
PEG-*ran*-PPG-ME70	37.3 ± 0.2	-
G60	62.9 ± 1.1	68.5 [120]
PEG-*ran*-PPG	41.4 ± 0.5	-

Table 4.4: **Surface tensions for our liquids.** We compared our measurements with the manufacturer's when available.

4.4 Liquid – solid systems

We describe here the properties of the solid-liquid pairs we have chosen. The atmosphere is always ambient air.

4.4.1 Swelling

A possible issue when working with gels and elastomers in contact with a liquid is that the latter may be a solvent of the macromolecules to some extent. We report here the results of tests that we have performed to address this issue.

We dip pieces of PDMS in every liquid we intend to use for 5 days to check whether they swell or not. Weighing PDMS slabs before and after immersion, we retrieve the swelling ratio $S = m_f/m_i$ where m_i and m_f are respectively the initial and final masses. Table 4.5 shows that all the swelling ratios are close to 1; we can neglect liquid diffusion in the substrate in our experiments – We exclusively use bad solvents of PDMS.

Liquid	S
U90	1.0072
G100	1.0007
PEG-*ran*-PPG-ME	1.0028
Water	1.0005
PEG-*ran*-PPG	1.0026

Table 4.5: **Swelling ratio** S **for SYLGARD™ 527 .** In our experiment, liquids do not swell solids.

4.4.2 Equilibrium contact angle measurements

The unreachable equilibrium state

Measuring macroscopic equilibrium contact angles θ_{eq} in soft wetting systems is tricky. When a droplet is deposited onto a substrate, it spreads until contact angle θ_c reaches its equilibrium value θ_{eq}. However, spreading dynamics of droplets relaxing to equilibrium after deposition can be very slow here, and it is not clear whether the measurement of the equilibrium contact is reliable or not.

When a U90 drop spreads on a piece of silicone gel (Fig. 4.9a), the contact angle decreases to a constant value (dotted line on Fig. 4.9d). However, the time scale of the order of 1000 s needed to reach a stationary value leaves many issues open. In particular, free-chain migration [35, 126], ridge growth [30] and water exchange between the atmosphere and the liquid may affect the final value of the contact angle, questioning the reliability of measurements. For example, droplets of water-based mixtures (Fig. 4.9b,e) and hygroscopic liquids (glycerol) 4.9c,f), the chemical composition of which evolves over time, never reach a regime of constant contact angle. It is thus difficult to determine an equilibrium state for all our systems.

Dynamic determination of the equilibrium contact angle.

As spreading drops are inconvenient, we measured θ_{eq} *a posteriori* from sliding drop experiments. To illustrate our method, we report the evolution of the dynamical contact angle θ_d

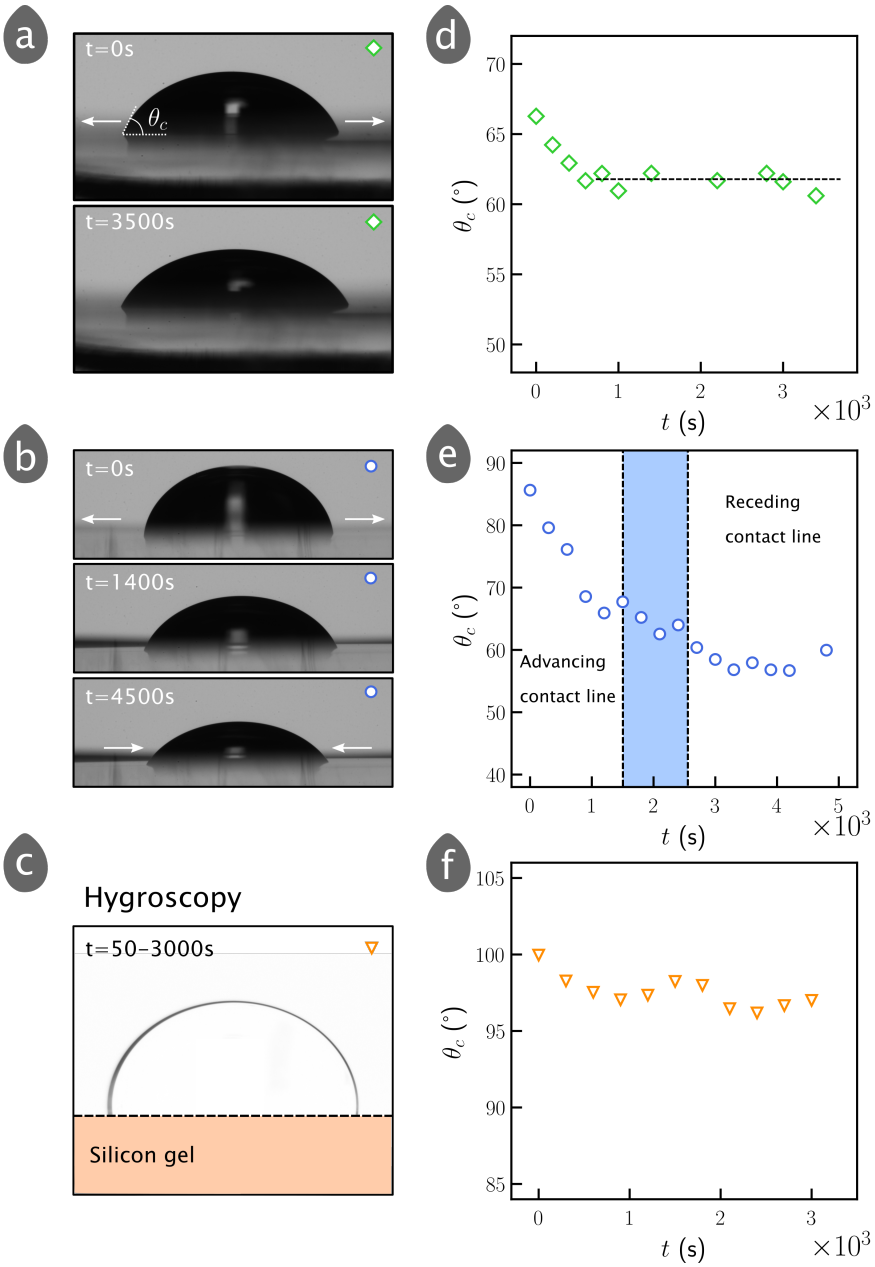

Figure 4.9: **Contact angle measurement of a spreading drops**. (a) U90, (b) U90-water mixing (40% of water) and (c) glycerol drops. (d), (e) and (f) display the corresponding evolution of macroscopic contact angle θ_c with time t. (a),(d) The contact line stops after ~ 1000 s and reaches a constant θ_c value. In the meantime, the ridge grows and free chains rearrange inside the materials [35]. (b),(e) When we add water, we have to deal with evaporation: the contact line first spreads, stops then recedes. (c),(f) Glycerol is hygroscopic. The drop absorbs water and swells (dark circle in (c) shows volume increase). In those three cases, we cannot define an equilibrium state.

as a function of the liquid capillary number Ca in Fig. 4.10. We define the equilibrium contact angle as the value of the dynamic contact angle at Ca = 0. We measure it by adjusting data with a linear fit (solid straight line in Fig. 4.10). For each {solid; liquid} system, we fit the data several times, changing the number of points over which fitting is performed. The standard deviation of these measurements gives the error measurement on θ_{eq}. Table 4.6 sums up the macroscopic equilibrium contact angles obtained with this method for each system. Note

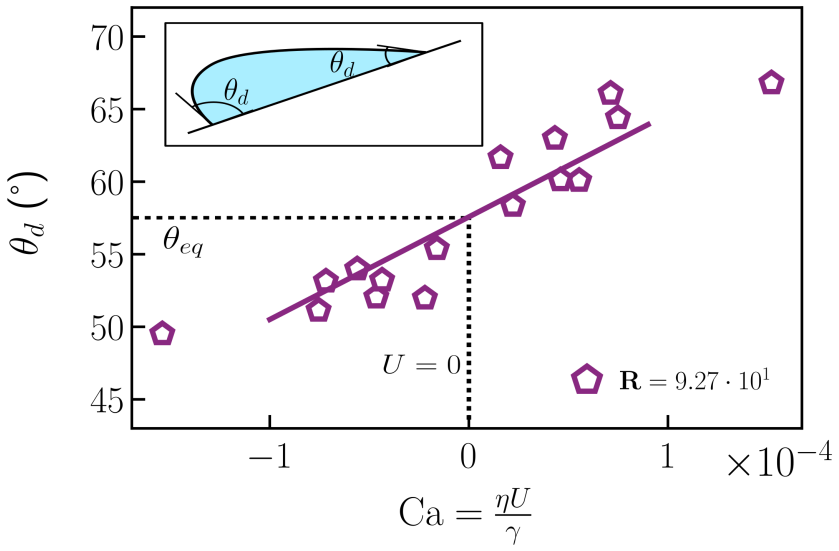

Figure 4.10: **Criterion for equilibrium contact angle θ_{eq} measurement**. Example with PEG-*ran*-PPG-ME70 . From sliding experiments, we report dynamic contact angles θ_d in function of running speed U. Zero speed value is θ_{eq}. A linear regression (solid line) for low-speed experiments is necessary to find θ_{eq}.

that it is either close to 60°, or close to 100°.

We note that this method indicates that contact angle hysteresis is at most of a few degrees. This value is compatible with other reports for this quantity [99].

Liquid	θ_{eq} (°)
U90	61.6 ± 0.7
G100	97.2 ± 1.1
PEG-*ran*-PPG-ME70	56.6 ± 0.7
G60	98.1 ± 0.9
PEG-*ran*-PPG	64.3 ± 0.2

Table 4.6: **Equilibrium contact angles θ_{eq} with SYLGARD™ 527 .** Measurements come from sliding experiments. We display the mean values and the standard deviations on several fits

4.4.3 Dissipation ratio

Rough estimation: number R

We have measured all the parameters necessary to estimate **R**. Now, a few tricks are used to obtain its estimate. First, we need to calculate the mean solid surface tension $\gamma_s = (\gamma_{sv}+\gamma_{sl})/2$ to estimate the elastocapillary length l_s. The solid/vapor surface tension of a silicone gel is measured in [51] $\gamma_{sv} = 29\,\mathrm{mN\,m^{-1}}$. Knowing γ and θ_{eq}, we retrieve γ_{sl} from the Young-Dupré equation (Eq. 2.8).

Doing so, we obtain estimates of l_s for each pair of solid and liquid. These values are summed up in Table 4.7. For all systems, the elastocapillary length l_s is of the order of ~ 10 µm. Values of **R** span four orders of magnitude, from about 2 to 10^4.

Pulsation dependance

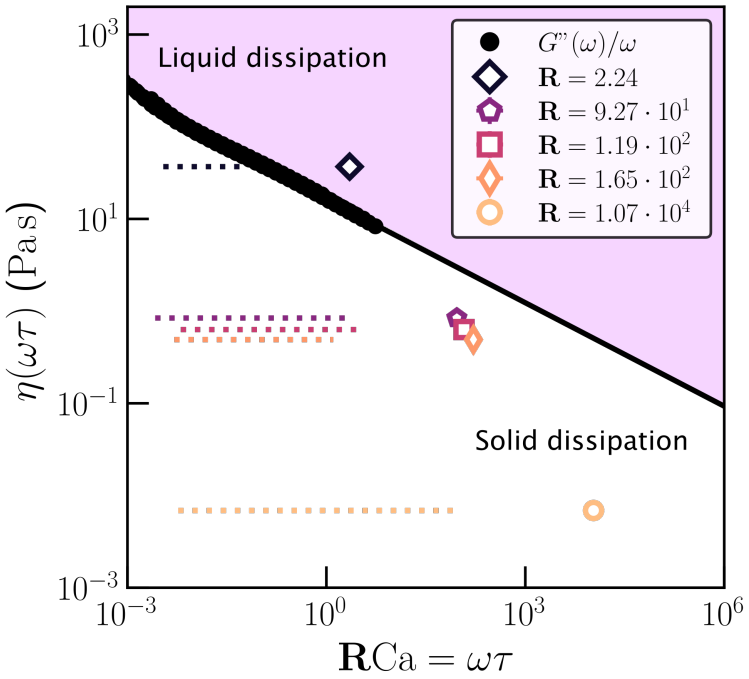

Figure 4.11: **Expected dissipation ratio in our systems**. We compare liquid viscosities to solid viscosity. Solid viscosity (•) depends on excitation frequency. Other symbols provide an upper limit for the excitation frequency (**R**Ca with Ca = 1). We expect liquid effects when the point locates above solid dissipation curve. Dotted horizontal lines correspond to experimental excitation pulsations.

We can also obtain a sense of the meaning of **R** by comparing the viscosities of the liquids we use to that of the solid. The latter depends on pulsation ω. The complex modulus of the material G(ω) is, in general:

$$G(\omega) = G'(\omega) + iG"(\omega). \tag{4.7}$$

G"(ω) represents energy dissipation. We can define an apparent viscosity of the solid based on this quantity, $\eta_s(\omega) = G"(\omega)/\omega$.

Now, we consider a contact line moving at velocity U on the surface of the elastomer. We can define a characteristic pulsation of this motion based on the properties of the material:

$$\omega_{LS} = U/l_s. \tag{4.8}$$

Now, we have that:

$$\mathbf{R}\mathrm{Ca} = \frac{U\tau}{l_s} = \omega_{LS}\tau \tag{4.9}$$

and there is equivalence between **R**Ca and $\omega_{LS}\tau$. If we set Ca = 1, a value we never reach in experiments, we have **R** = **R**Ca and we can interpret **R** as an upper limit for excitation pulsation. Thus doing we can plot liquid viscosities for $\omega = \omega_{LS}$ and $Ca = 1$, which leads to $\omega\tau = \mathbf{R}$. Doing so, we obtain figure 4.11. On the same plot, the Chasset-Thirion fit extends experimental data and splits the space into two regions, one above it where liquid dissipation dominates and the other below where solid dissipation dominates.

Figure 4.11 indicates that we can hope to overcome dissipation in the solid with our most viscous liquid, U90, for which **R** ~ 2. Conversely, the dynamics observed for contact lines in

the case where the liquid is G60, for which $\mathbf{R} \sim 10^4$, should be dictated by viscoelasticity in the solid.

In practice, experimental values for Ca are smaller than $2.0 \cdot 10^{-2}$. Thus, real non-dimensional excitation pulsations $\mathbf{R}\mathrm{Ca} = U\tau / l_s$, reported as dotted lines, are well below the upper limit **R**. We see that we can expect to have dissipation in the liquid of the same order of magnitude as in the solid in the case of U90. In all other cases, these effects should be vanishingly small.

In short, **R** helps to pick out and characterize wetting systems, even if it overestimates the actual dissipation ratio. Still, it provides a good estimation and we refer to it as dissipation ratio in the following.

Liquid	l_s (µm)	**R**
U90	9.0 ± 0.1	$(2.24 \pm 0.42) \cdot 10^0$
PEG-*ran*-PPG-ME70	8.7 ± 0.1	$(9.27 \pm 1.10) \cdot 10^1$
G100	15.3 ± 0.3	$(1.19 \pm 0.20) \cdot 10^2$
PEG-*ran*-PPG	9.3 ± 0.1	$(1.65 \pm 0.11) \cdot 10^2$
G60	15.5 ± 0.2	$(1.07 \pm 0.04) \cdot 10^4$

Table 4.7: **Elastocapillary length l_s and dissipation ratio R for {SYLGARD™ 527 liquid} systems.** l_s roughly equals ten microns, while **R** ranges over four orders of magnitude.

Chapter 5

Experimental set-up

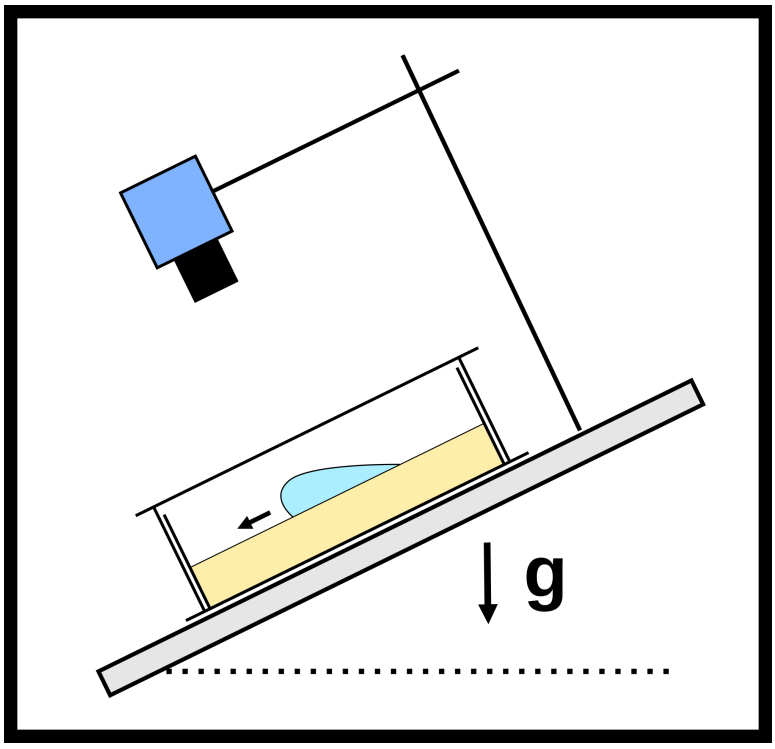

In this section, we describe the set-up we have used to study sliding droplets. We also provide tests and solutions for various problems we have encountered that have to be accounted for to reproduce our results.

5.1 Set-up

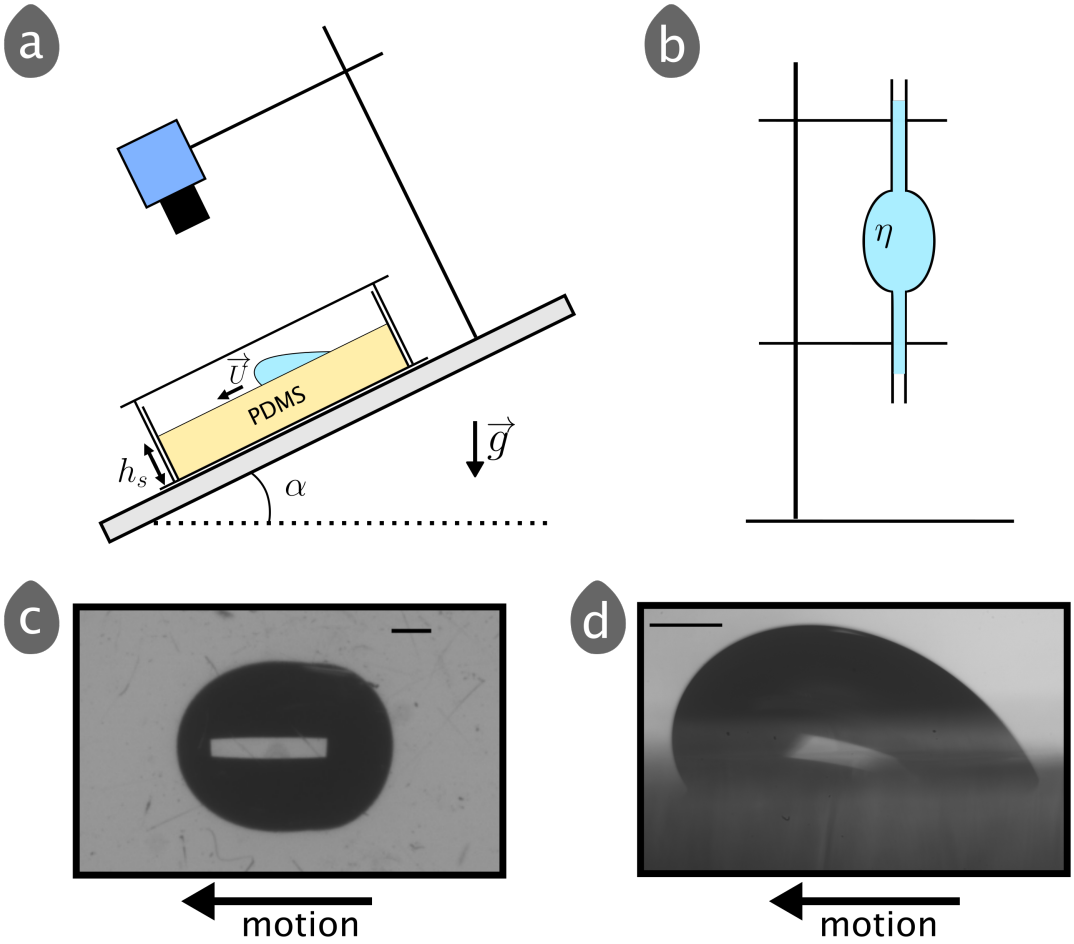

Figure 5.1: **Experimental set-up.** (a) Sketch of the inclined plane. The inclination angle is denoted α. We keep the lid on during experiments. (b) In parallel, we check the liquid viscosity η with a capillary viscosimeter. Two cameras record the following (c) top and (d) side views (scale bars correspond to 1 mm). We can therefore measure the trajectory and the dynamic contact angles θ_d.

The set-up we use relies on an inclined plane made of aluminium that supports the vessel containing the silicone layer of thickness h (Fig. 5.1a). We attach two digital cameras (Imaging Source, DMK 33UX174): one records a top view of the moving droplet while the other (not represented) captures a side view. Thus, we can track the dynamics and the shape of sliding droplets. We can also measure contact angles at the leading and trailing edges of the droplet. Spatial resolution is 33 $\mu m\,px^{-1}$ and 4 $\mu m\,px^{-1}$ for top and side views respectively . Cameras move together with the plate when we change the inclination α, such that the substrate remains in the focal plane of the top camera, and remains horizontal for the side camera.

Room temperature and humidity vary from day to day. The setup includes a capillary viscosimeter (Fig. 5.1b) to account for the variations of the dynamic viscosity η of the liquids.

We check viscosity twice a day and use a new liquid batch every day.

We deposit droplets using a micropipette. We vary the volume between 20 and 40 µL. As we use viscous liquids, we have to find a way to check drop volume as well. Indeed, we inject smaller volumes than what the micropipette indicates. To circumvent this issue, we weigh the droplet at the end of the experiment. Knowing liquid densities, we can go back to the volume of the droplet, a necessary piece of information if we want to compute the Bond number of the experiment. We take special care not to inject air bubbles. If so, and if we fail to burst the bubble with a needle, we perform again the experiment.

Liquid PDMS poured in the vessel before curing forms a meniscus everywhere around the walls of the vessel. This meniscus obstructs the side view of droplets and must be removed. To do so, we remove the viscoelastic slab from the vessel. Then we cut the meniscus carefully with a razor blade while stretching the sample the least possible. We stick it on another rigid substrate (cleaned with ethanol and distilled water before), cut edges and put a lid on the vessel. In practice, a smaller slice of PDMS, stuck next to the main slab, maintains the lid when we incline the sample. Fig. 5.1c and Fig. 5.1d show examples of the recorded top and side views.

5.2 Image capture

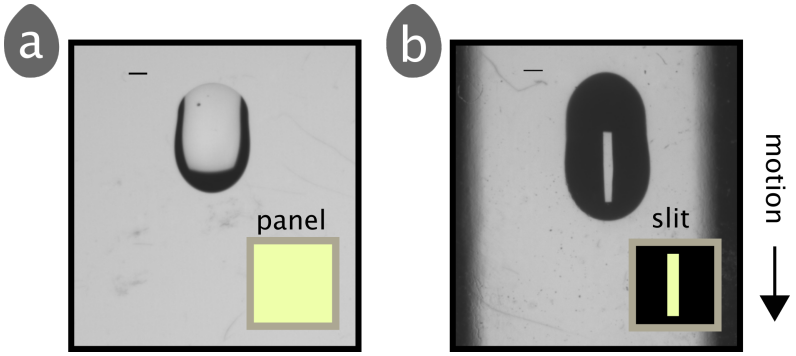

Figure 5.2: **Lighting technique**. Images are obtained when (a) the whole LED panel lights the sample and (b) when we reduce the size of the light source. In both cases, the volume of the glycerol drop is V = 40 µL , the inclination is α = 40 ° and the scale bar is 1 mm. Using a light slit better captures the shape of the drop.

A key issue in these experiments is to be able to track the contact line around sliding droplets. Such a task is difficult to achieve if the light field is left as is. However, simple shaping of light propagation in the system leads to a more accurate contact line identification.

The center of the aluminium plate supporting the sample is hollowed out. As the vessel, the gel and the liquid are all transparent, we capture images of droplets when light coming from a LED panel goes through them. However, the interface of the droplet is curved. This region deflects light rays away from the camera sensor and appears black (Fig. 5.2a). If the light source is too wide, the drop also deflects in the picture light rays that should not reach the camera were all interfaces flat. Masking the light source cuts those light rays and helps better define the perimeter of the drop (Fig. 5.2)– resulting in well-contrasted images that facilitate data analysis. For fast experiments, we had to adapt the size of the light source live, by hand.

Likewise, we carefully adapted the size of the light source to optimize the contrast of side views. Despite those efforts, the camera is not perfectly parallel to the surface of the gel. The

region of the contact line is blurred (Fig. 5.1d): if the drop is too close to the edge of the gel, this region is too blurred and we cannot measure the contact angles accurately.

5.3 Image analysis

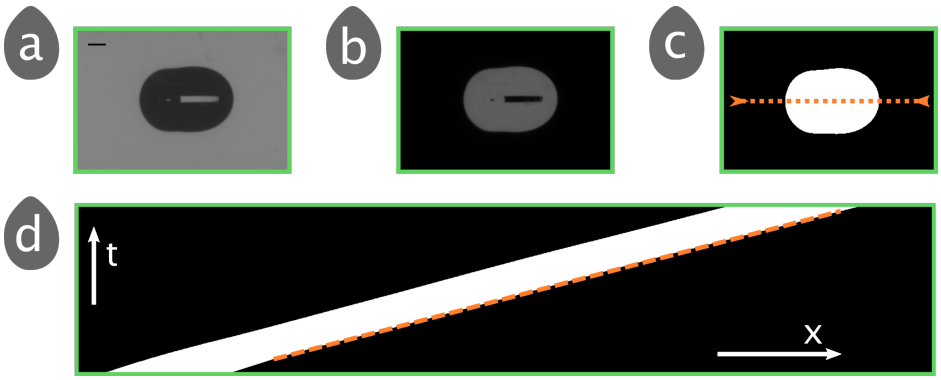

Figure 5.3: **Image analysis.** (a) Raw image of a glycerol drop (V = 20 µL, α = 50°). Scalebar: 1 mm. (b) Same image without background. (c) We apply a threshold and fill holes. For each frame, we look at the position of the drop along the orange dotted line. (d) We obtain the following kymograph and retrieve the speed of the drop thanks to the slope of the diagram (orange dashed line).

Once we have captured well-contrasted movies, we analyze them using the FiJi software package [127]. We rotate raw image stacks (Fig. 5.3a) so the drop moves along a horizontal line. As the surface of our polystyrene vessels often exhibit scratches, we subtract the background of the image to retain only moving objects in the movie. Figure 5.3b shows typical images obtained. Then, we apply a threshold and fill holes to isolate the drop (Fig. 5.3c), and build a space-time diagram, or kymograph, of droplet motion (Fig. 5.3d) that gives the trajectory of the drop (white streak on Fig. 5.3d). We retrieve the front speed of the drop from the slope (orange dashed line in Fig. 5.3d).

We also measure the radius of curvature R_{curv} of the trailing edge of the droplet from binary images such as Fig. 5.4 with a FiJi script [128]. To account for error bars, we measure R_{curv} at different times and different thresholds.

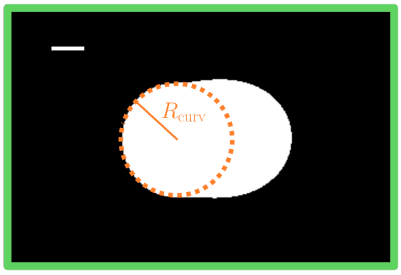

Figure 5.4: **Measurement of the radius of curvature at the tail of the drop.** We extract the rear radius of curvature R_{curv} from binary pictures such as in fig. 5.3c. For each sliding experiment, measurements at different frames and thresholds give uncertainties. Scale bar:1 mm.

5.4 Experimental issues and their solutions

5.4.1 Surface changes of PDMS with time

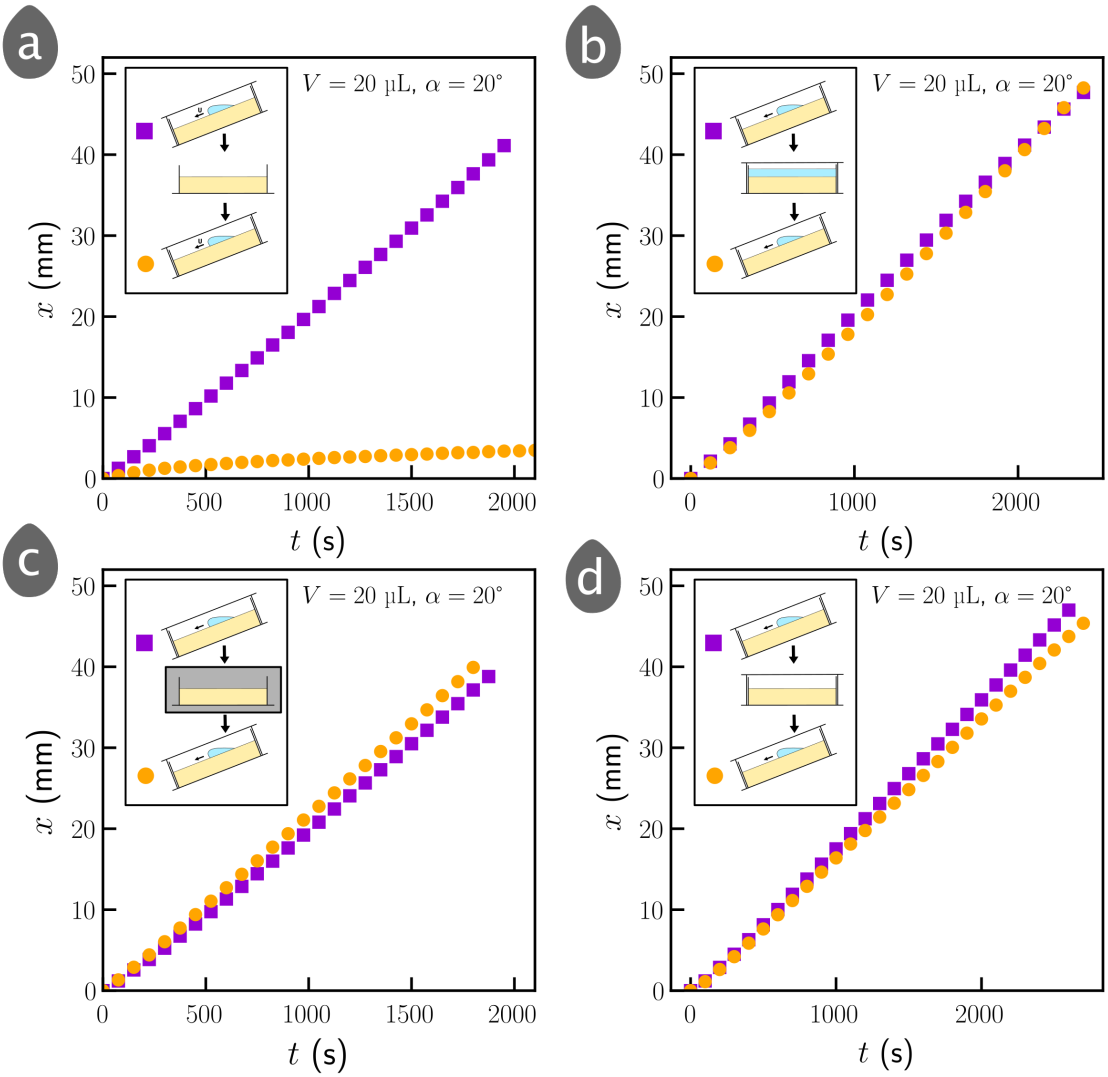

Figure 5.5: **silicone gel ageing.** For all experiments, liquid is glycerol, V = 20 µL, α = 50 ř. The substrate ages in between two successive experiments. For all graphs, (■) and (•) respectively corresponds to the first and second experiment. (a) Trajectories are not reproducible when the vessel is open between two experiments. (b) They are reproducible when the sample is immersed in water between two experiments. (c) Trajectories are reproducible when the sample is protected from light when open. (d) The lid of the vessel filters the wavelengths responsible for ageing.

Figure 5.5a shows that the trajectories of droplets sliding on the surface on PDMS differ if the vessel containing the sample is opened. The second experiment (orange bullets) is much slower than the first one (purple squares). The longer we open the vessel, the slower the second drop is. These measurements suggest that the surface properties of our samples change with time. If we perform a third experiment without opening the vessel, the drop will follow the same trajectory as the second experiment. We suspect two culprits:

- water molecules in the surrounding atmosphere, that may change the cross-linking reaction in the vicinity of the surface;

- light, especially UV rays, that would help sustain the cross-linking reaction at the surface.

Fig. 5.5b shows that covering the silicone surface with water does not affect trajectories. On the other hand, removing the lid but protecting the vessel from light leaves the surface unscathed. Indeed, experiments one day apart are reproducible when the sample is stored in pitch black (Fig. 5.5c). We conclude that light is responsible for the surface modifications that we have identified.

To the best of our knowledge, this effect has not been reported in the elastowetting literature and we should account for it from now on. Literature on surface analysis of PDMS reports that UV and UV/ozone plasma treatments modify the surface of PDMS [129–131]. UV light that might originate from ambient light. We circumvent this issue if we keep the lid on the vessels (Fig. 5.5d) in all experiments, except when we deposit liquid drops (~ 30 s per drop). Moreover, we perform experiments on one-day-old silicone gels. We thus avoid discrepancies due to aging.

5.4.2 Trajectories on the same path

We know that the wetting ridge relaxes when we release the pulling force. Relaxation is not immediate in the most general case. According to *Xu & al.* [34], the ridge size decreases one-hundred-fold in about one minute for a silicone gel. The ridge also relaxes over a longer time scale when increasing the residence time of the drop on the surface [35]. Thus, we may wonder whether a drop deposited on the surface and sliding down the inclined plane experiences deformations left during previous experiments?

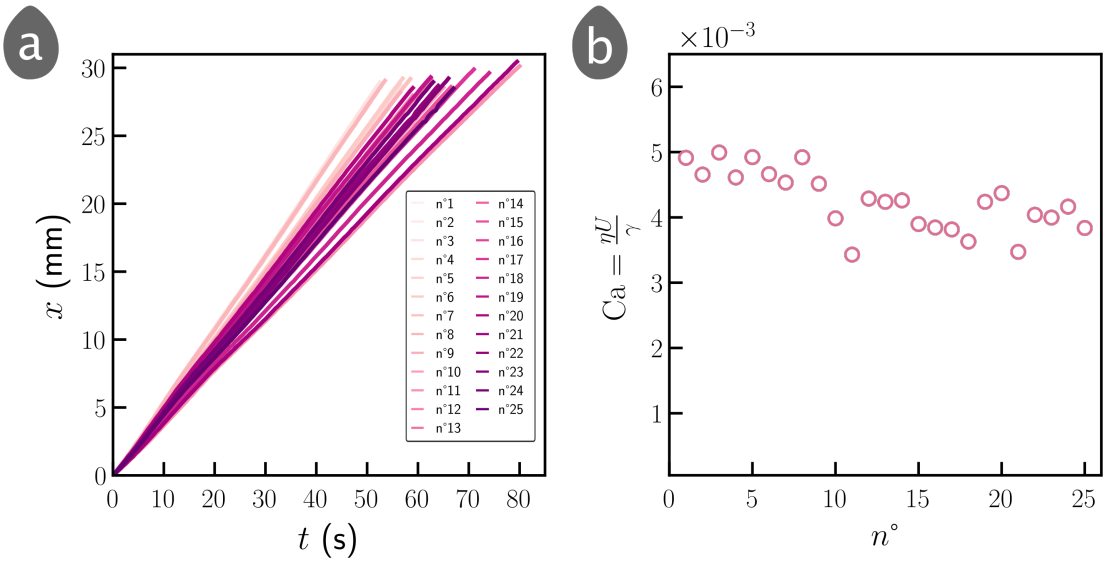

Figure 5.6: **Experiments on the same location.** Same experiment (Glycerol, V = 20 µL, α = 50 °) repeated 25 times on the same location. The corresponding Bond number is $\mathrm{Bo}_\alpha = 0.37 \pm 0.03$. (a) All trajectories. As we repeat the experiment, the drop seems slower. (b) This trend is confirmed when we report the capillary numbers Ca for each trial.

We investigate how the system responds when several drops slides on the same trail. A few minutes elapse between two identical experiments. Figure 5.6a shows all 25 trajectories while Fig. 5.6b shows the capillary number Ca for each trial. On average, early trajectories

have a higher velocity than experiments performed later. Figure 5.6b confirms the decreasing trend in Ca over time.

We also performed 4 experiments in the same conditions, except that the starting point is different for each trial (the corresponding trajectories are displayed in Fig. 5.9a). The corresponding statistical dispersion (in terms of Ca) is $\Delta\text{Ca} \simeq 1 \cdot 10^{-3}$. We see in Fig. 5.6b that the0 capillary number decreases by $\Delta\text{Ca} \simeq 1 \cdot 10^{-3}$ after about ten trials on the same location.

Zhao measured the profile of the wetting ridge with the Schlieren technique (he only has access to the solid/vapor interface) [43]. He showed that the solid/vapor interface stays flat 2 mm away from the contact line (Look at Fig. 3.7 in [43] for instance).

As a result, we conducted all experiments on fresh surfaces. Each drop slides at least 4 mm away from other experiments, such that previous deformations do not affect the experiments.

5.4.3 Resting time effect

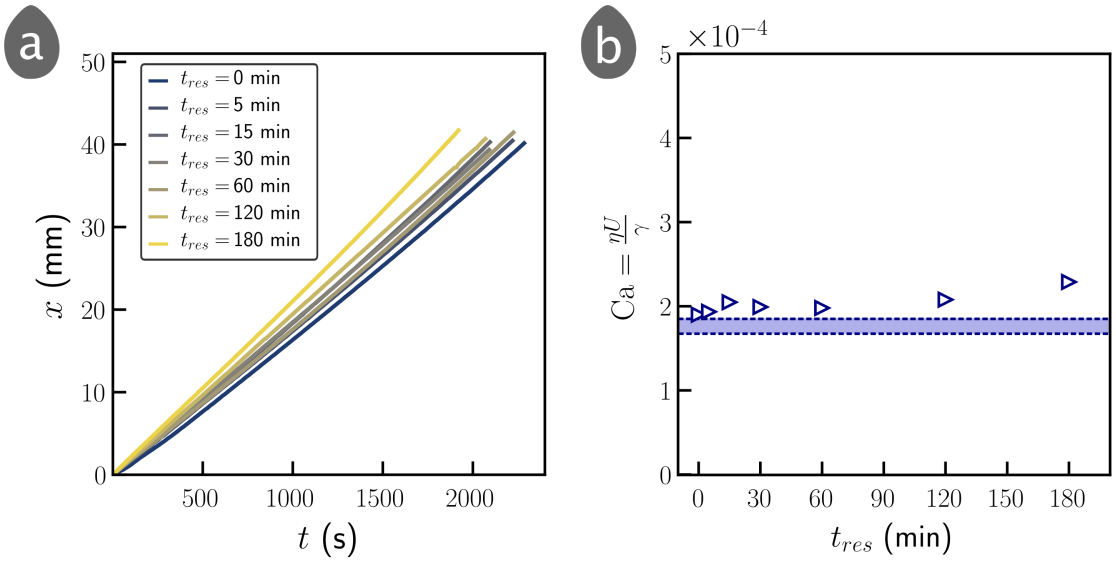

Figure 5.7: **Effect of resting time t_{res}.** Same experiment (Glycerol, V = 20 µL, α = 20 °) with resting time t_{res} increasing up to 3 h). The corresponding Bond number is $\text{Bo}_\alpha = 0.16 \pm 0.01$. (a) The corresponding trajectories and (b) capillary numbers Ca in function of t_{res}. Color patch: statistical dispersion when we incline straight away the same drop.

Park et al. show that the ridge surrounding a droplet resting on a silicone gel with a shear modulus $\mu_0 = 1$ kPa grows from 7.15 µm to 8.25 µm in 2 min [30], indicating that equilibrium has not been reached yet. In our experiments, we expect this phenomenon to occur before inclination. [30, 35]. Does resting time t_{res} affect sliding drops trajectories?

We increase the resting time t_{res} of glycerol droplets from 0 up to 3 h, everything else is kept constant (α = 20°, V = 20 µL). Figure 5.7 displays the corresponding trajectories (a) and Ca (b). We observe that an increase in the resting time of the droplet leads to a slight increase in its sliding velocity. This result is rather unexpected, as ridge growth is expected to lead to more dissipation.

Going back to images, we see that the volume of the droplet changes over time. The droplet absorbs water during its residence on the surface. As a consequence, its weight increases and its dynamic viscosity decreases. Both trends are consistent with faster drops.

We compare its magnitude with the statistical dispersion of 5 identical experiments inclined right away (color patch in Fig. 5.7b, the corresponding trajectories are displayed in Fig. 5.9b). We note that this statistical dispersion compares with the magnitude of the effect of t_{res} (at least when $t_{res} < 2$ h). As a precautionary measure, we incline all experiments straight away, though resting time effects are negligible.

5.4.4 Comments on evaporation

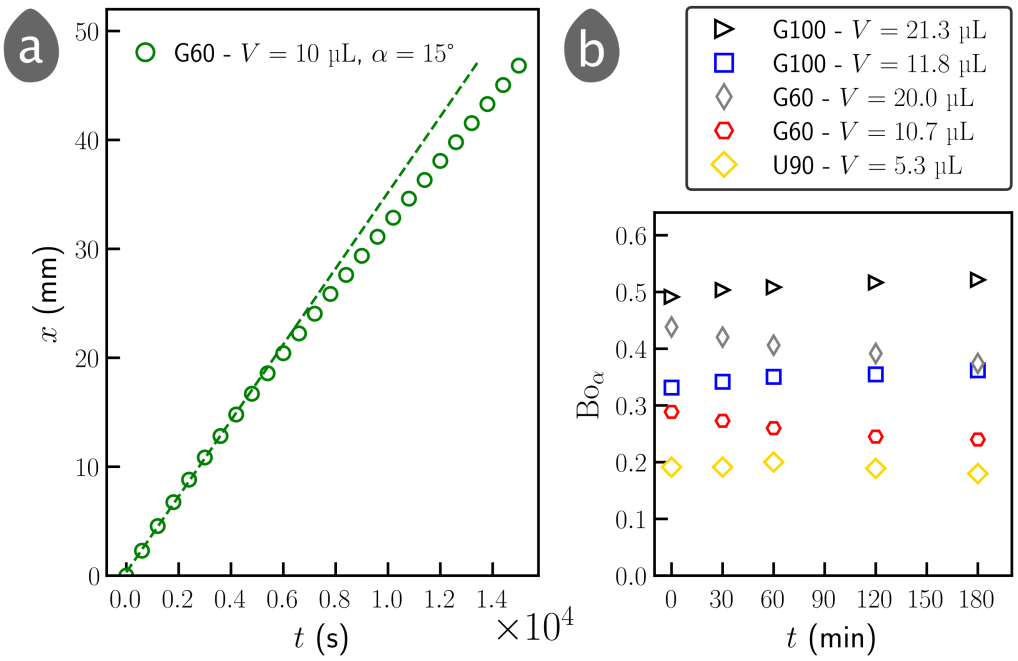

Figure 5.8: **Evaporation and hygroscopy.** Our liquids may evaporate or absorb water from the surrounding air. (a) The trajectory of evaporating 60% glycerol water solution drop (hollow circles). In that case, we determine Bo_α independently and only fit the beginning of motion, before those effects happen (dashed line). (b) Except for Ucon oil, Bond number Bo_α evolves when the experiment exceeds 1 h. It increases for glycerol (hygroscopy) and decreases for glycerol water mixture (evaporation).

Some experiments last for hours, and trajectories sometimes lose their linearity with time (Fig. 5.8a). In such cases, evaporation or hygroscopic effects may change the droplet running speed U. To characterize this effect, we weigh glycerol, glycerol-water and Ucon droplets as a function of time. Figure 5.8b reports this evolution in terms of the Bond number Bo_α (we refine the definition of the Bond number Bo_α in Eq. 6.7). Here, we neglect inclination to compute Bo_α. We see that U90 droplets remain stable, as $\mathrm{Bo}_\alpha \simeq 0.2$ for 3 h. It is a good piece of news as experiments often last several hours for this liquid. However, glycerol absorbs water and glycerol-water solutions lose water as expected: Bo_α increases by 6 to 9 % for glycerol, and decreases by 16 to 18 % for glycerol-water solutions. Weighing droplets at the end of such an experiment gives inaccurate values of Bo_α, so we must adapt our protocol. We retrieve early Bond numbers with independent weighing (more than 30 drops for each volume to have a correct statistical error), and fit only early stages of droplet motion that we assume to correspond to that Bo_α (green dashed line in Fig. 5.8a).

5.4.5 Sum-up

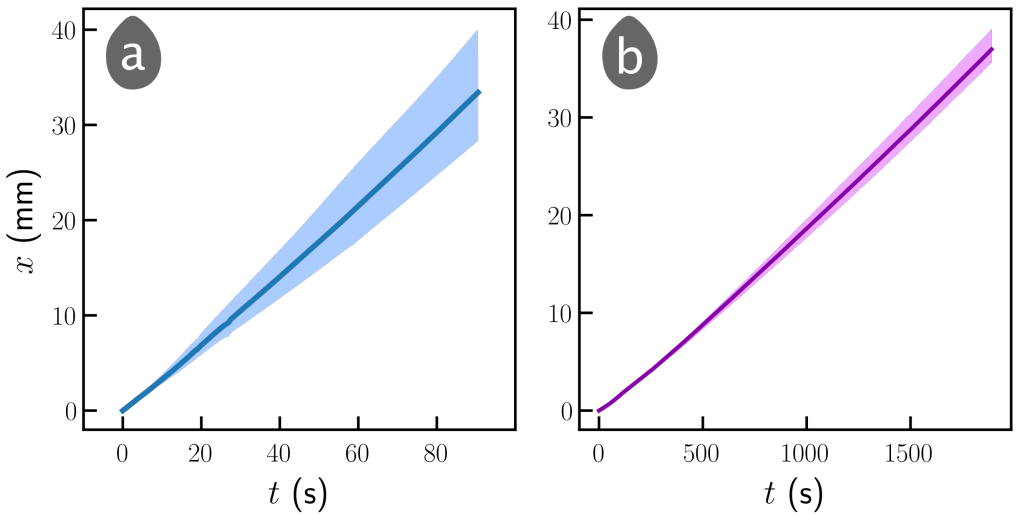

Figure 5.9: **Reproducibility of experiments.** Averaged trajectory on 4 experiments (solid line) and corresponding statistical dispersion (color patch). V = 20 µL glycerol drop. (a) α = 50 ° and (b) α = 20 °. We obtain linear trajectories.

All those tests allow us to refine our experimental protocol. When we deposit the liquid droplet, we avoid air bubbles that might affect the measurement. We also suppress the influence of resting time and starting point in our protocol. Droplets are deposited at different locations on a single sample so that they do not slide on a track taken by a previous droplet. We incline the system right after deposition, so drops rest between 10 and 30 s before sliding.

To ensure a reproducible surface state between each sample, we carry out experiments on enclosed, one-day-old samples. Doing so, we obtain linear trajectories (Fig. 5.9). The remaining statistical variation (colored patch in Fig. 5.9) might come from small differences in volume and inclination speed.

Part III

Observations and Results

Chapter 6

Shapes

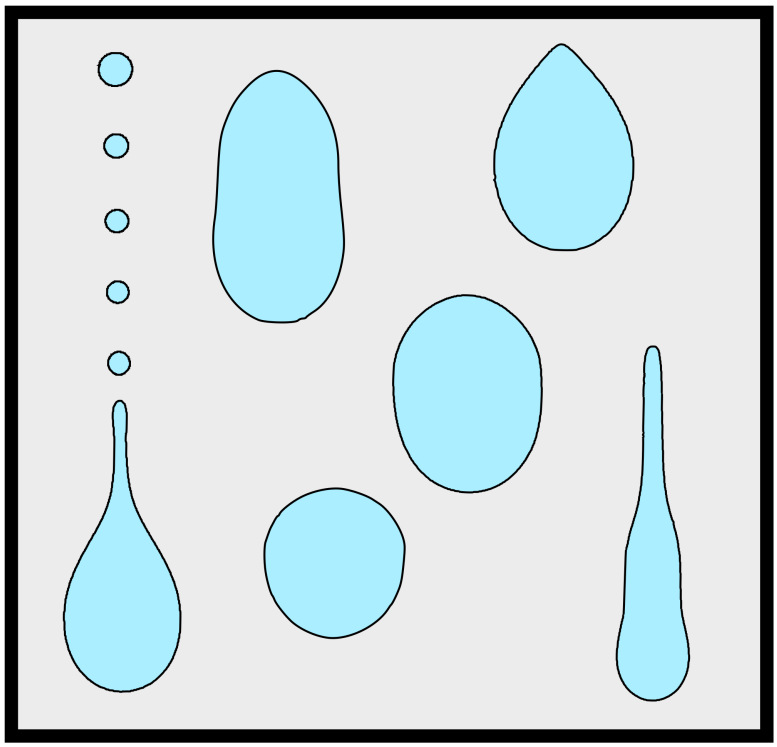

6.1 General observations

6.1.1 A refined definition of the Bond number

Before proceeding with the presentation of our observations regarding the shape of the sliding droplets on silicone gels, we suggest a definition of the Bond number different of the one used by *Podgorski et al.* that should be a better estimate of the balance between gravity and capillarity for droplets when they have reached equilibrium on the surface of gels. This definition accounts for the radius of the contact area between the droplet and the surface, a quantity that will also be important in estimating dissipation later in this document.

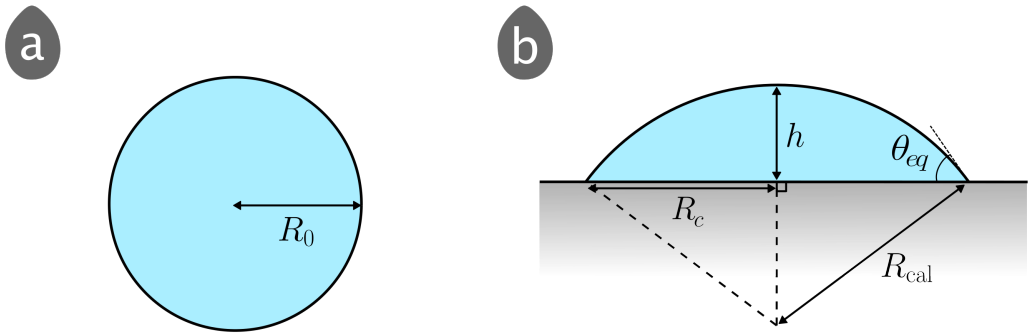

Figure 6.1: **Different configurations for a liquid drop.** (a) As a sphere, it has a volume $V = 4R_0^3/3\pi$. (b) This drop takes the shape of a spherical cap on the substrate, with radius R_{cal}, heigth h, contact radius R_c and contact angle θ_{eq}.

In our experiments, we deposit a volume V on the substrate that corresponds to a sphere of radius $\mathbf{R_0}$ (Fig. 6.1a). It spreads onto the substrate until it reaches its equilibrium shape, a spherical cap with radius R_{cal}, height h, contact radius R_c and contact angle θ_{eq} (Fig. 6.1b). In this configuration, the ratio between its weight and the capillary force that applies along its perimeter, called the Bond number, writes:

$$Bo_\alpha = \frac{\rho g R_0^3}{\gamma R_c} \sin\alpha. \tag{6.1}$$

R_c is out of reach from top views when the equilibrium contact angle is larger than $\pi/2$. We access R_0 by weighing the drop. Knowing the equilibrium contact angle θ_{eq} and assuming that droplets form spherical caps, we can write:

$$\begin{cases} R_c = R_{cal} \cos\left(\dfrac{\pi}{2} - \theta_{eq}\right) \\ R_{cal} - h = R_{cal} \sin\left(\dfrac{\pi}{2} - \theta_{eq}\right). \end{cases} \tag{6.2}$$

Thus, we link the contact radius and the height of the droplet to the spherical cap radius:

$$\begin{cases} R_c = R_{cal} \sin\theta_{eq} \\ h = R_{cal}(1 - \cos\theta_{eq}). \end{cases} \tag{6.3}$$

Now, we recall the formulas for the volume for both a sphere and a spherical cap:

$$\begin{cases} V = \dfrac{4\pi}{3} R_0^3 \\ V = \dfrac{\pi}{3} h^2 (3R_{cal} - h) \end{cases} \tag{6.4}$$

and we express them in terms of $\mathbf{R}_c$ and θ_{eq}:

$$\begin{cases} V = \dfrac{4\pi}{3} R_0^3 \\ V = \dfrac{\pi R_c^3}{3} \dfrac{(2+\cos\theta_{eq})(1-\cos\theta_{eq})^2}{\sin^3\theta_{eq}} \end{cases} \tag{6.5}$$

Volume conservation then leads to:

$$\frac{R_c}{R_0} = \frac{1}{f(\theta_{eq})} = \sin\theta_{eq} \left(\frac{(2+\cos\theta_{eq})(1-\cos\theta_{eq})^2}{4} \right)^{-\frac{1}{3}}. \tag{6.6}$$

Fig. 6.2 shows R_c/R_0 as a function of θ_{eq}. As expected, we retrieve the limit cases of *non-wetting* when $\theta_{eq} \to 180°$ and *total wetting* in the case $\theta_{eq} \to 0$. Injecting Eq. 6.6 into Eq. 6.1, we obtain a new expression:

$$\boxed{Bo_\alpha = f(\theta_{eq}) \frac{\rho g R_0^2}{\gamma} \sin\alpha.} \tag{6.7}$$

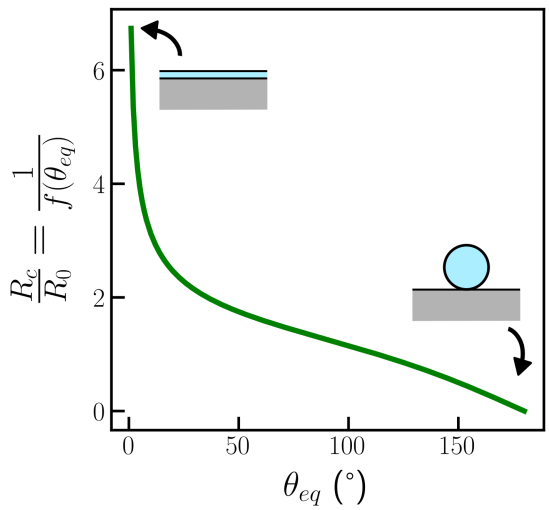

Figure 6.2: **How does θ_{eq} correct Rc at fixed R_0.** We retrieve the expected behavior for *total wetting* ($R_c = \infty$, $\theta_{eq} = 0°$) and *non-wetting* ($R_c = 0$ mm, $\theta_{eq} = 180°$).

6.1.2 Shape diagram: generalities

Previous studies document top views of drops sliding onto a rigid substrate [71, 73, 74, 77, 96–98], but the shape diagram remains unknown in the soft case: to the best of our knowledge, we found top views of stable drops in [132]. To fill this gap, we report top views of the droplets

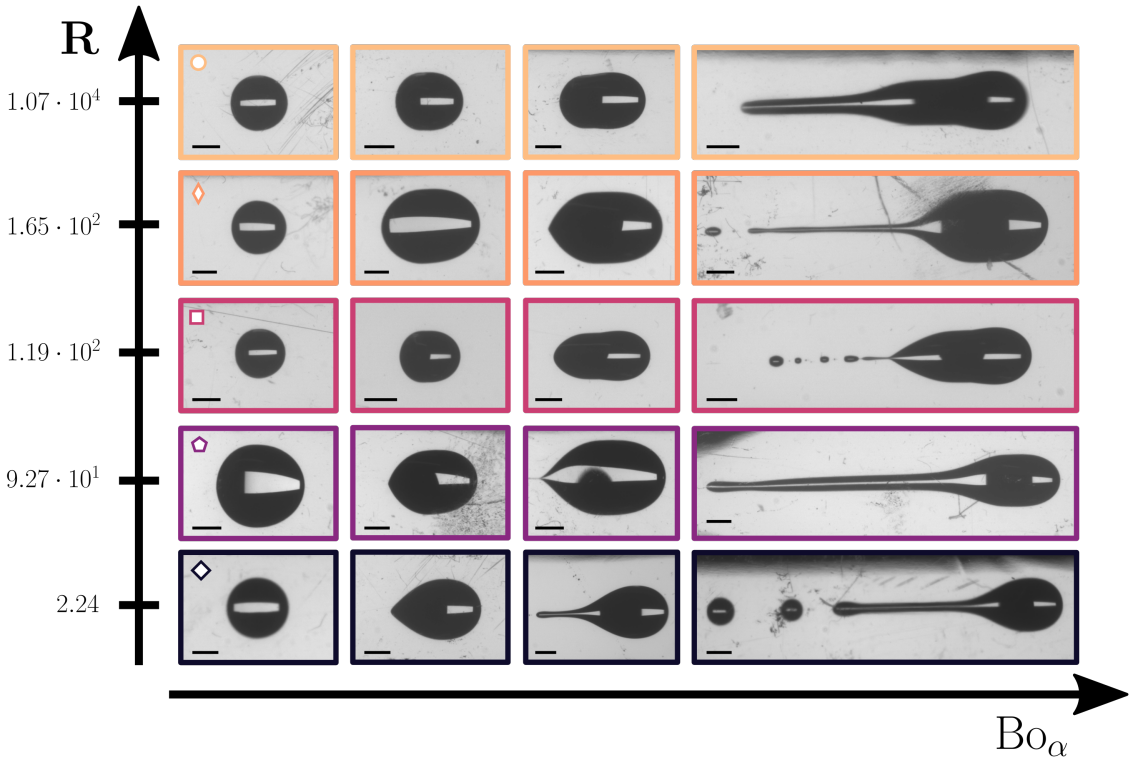

Figure 6.3: **Shapes as a function of the Bond number Bo_α for different values of R.** For each system, the drop becomes more asymetric and eventually unstable as Bo_α increases (along a line). It also elongates as **R** increases (along a column). U90: Bo_α = 0.095, 0.239, 0.273, 0.409; PEG-*ran*-PPG-ME70 : Bo_α = 0.111, 0.238, 0.270, 0.413; G100: Bo_α = 0.103, 0.237, 0.480, 0.496; PEG-*ran*-PPG : Bo_α = 0.107, 0.238, 0.273, 0.350; G60: Bo_α = 0.107, 0.268, 0.404, 0.442. Scale bar: 2 mm.

in Fig. 6.3. The shape mapping is built using two parameters: the dissipation ratio **R** and the Bond number Bo_α.

A qualitative examination of the images in Fig. 6.3 make it obvious that the dissipation ratio plays a major role in setting the shape of droplets. Two characteristics are common in all cases. First, the front edge of the droplets remains rounded regardless of the value of **R**. Also, at the smallest values of Bo_α that we display in this figure, droplets's geometry is close to axisymmetric whatever the value of **R**. Finally, droplets always destabilize above a threshold velocity. Droplets exhibit stretched tails beyond the instability threshold, when they leave pearl patterns in their wake. However, many distinctions remain to be described.

For $\mathbf{R} \sim 2$, the droplet adopts a shape reminiscent of the one we introduced in Fig. 3.2. While the front is rounded, the trailing edge of the droplet has the shape of a corner. When $\mathbf{R} \sim 100$, two features distinguish droplets from those observed at $\mathbf{R} \sim 2$. First, in most cases, the trailing edge has a curvature comparable to the front edge. Second, droplets have an elongated shape. Some parts of the droplet contour have very large, if not infinite, radii of curvature. We also observe that some droplets have a peanut shape for $\mathbf{R} \gg 1$.

The images of Fig. 3.2 also contain puzzling features. Droplets at $\mathbf{R} = 92.7$ and $\mathbf{R} = 165$, made of PEG-*ran*-PPG or an aqueous solution of PEG-*ran*-PPG ME, differ in shape from those made of an aqueous solution of glycerol characterizing by a comparable value of $\mathbf{R} = 119$. The former exhibit a sharp corner at their trailing edge (even sharper than in the case of U90) before they become unstable, while the latter remain rounded all along. We will come back to this issue when discussing the perspectives of this work (Chap. 9). We also observe

that the properties of pearl patterns cover rich ground also at large values of **R**. Such variability is also commented upon in ref. [97] in the case of rigid substrates. Here, we see that the size and the gap between ejected droplets as Bo_α increases beyond its critical value for instability (Fig. 6.4). We lack experimental statistics to provide reliable size distributions and estimates of the features of the patterns.

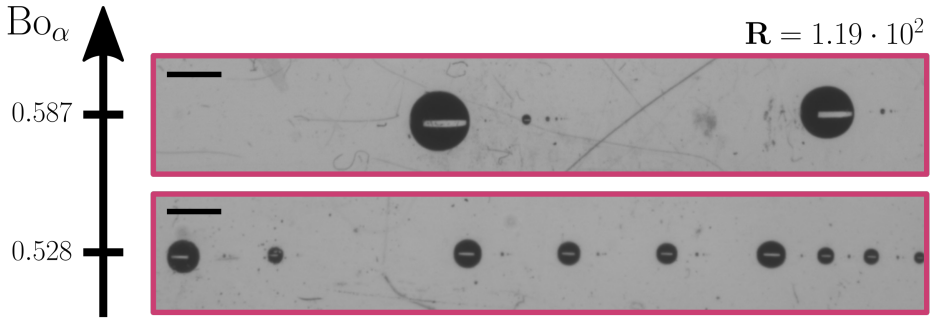

Figure 6.4: **The pearl pattern becomes more complex as the droplet velocity increases.** The size and the spacing between pearls increases with Bo_α. Scale bar: 2 mm.

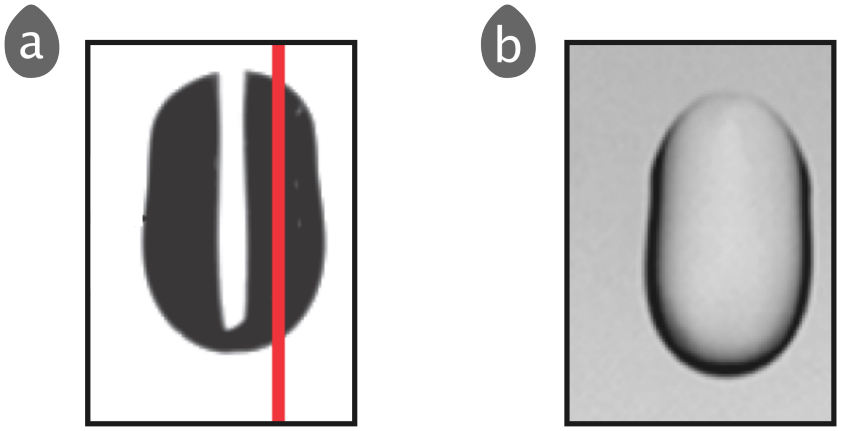

Figure 6.5: **Constricted droplets in the literature.** (a) {SYLGARD™ 184 ; 50% glycerol-water mixture} [132]. The authors uses the red line to draw a spatio-temporal diagram (not reproduced here). (b) ({glass; mercury} [133].

The last aspect of the shape diagram that we wish to comment on is the apparent peanut shape of droplets in certain cases. This shape results from a narrowing of the droplet around mid-length when seen from the top. *Hourlier-Fargette* reports similar droplet shapes (Fig. 6.5a) with a stiffer silicone gel [132]. Mercury droplets moving onto a rotating glass cylinder (Fig. 6.5b) seem to constrict as well [133]. If we consider this shape the projection of the contact line on the camera sensor, we have to think about its meaning in terms of contact line motion. Starting from the front and moving along the contour, the contact line switches from an advancing one to a receding. However, the contact line is almost straight after the constriction. Given the connection between straight contact lines around moving droplets and contact angle hysteresis, the peanut shape would then suggest that the contact line switches to a receding state before going back to a state of vanishing velocity and then again back to a re-

ceding state. The observation of such a response is not expected, and the solution lies in fact in a very simple matter.

For the systems that display peanut-shaped droplets, the equilibrium contact angle exceeds $\pi/2$. Thus, when the contact line advances, the droplet overhangs the substrate, hiding the contact line (Fig. 6.6). Then, despite deceiving top views, the contact angle always decreases from $\theta_{d,a}$ to $\theta_{d,r}$ (dynamic contact angles at the front and the rear of the drop) along the contour of the drop, whatever the values of **R** and θ_{eq}.

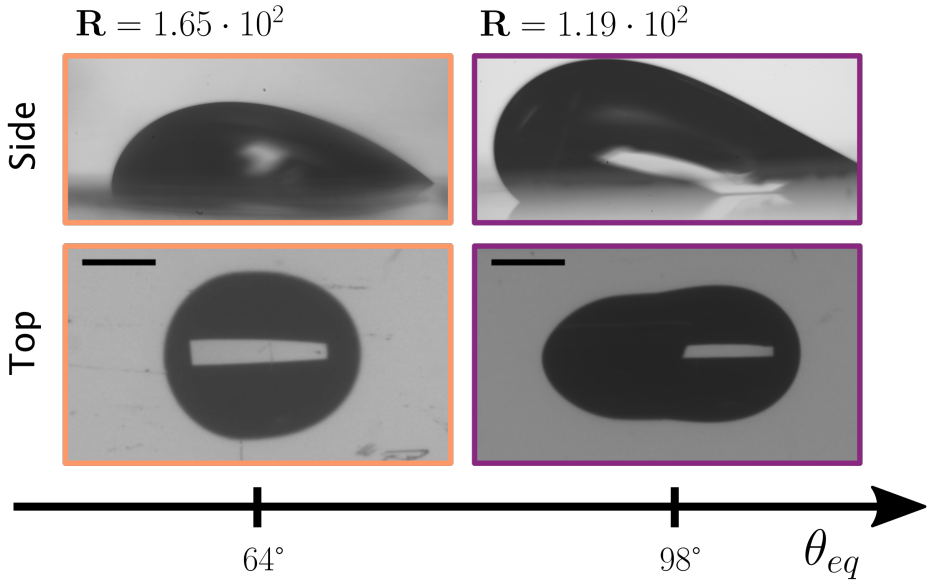

Figure 6.6: **Effect of θ_{eq} on the shapes** $Bo_\alpha = 0.19$ on the left and $Bo_\alpha = 0.45$ on the right. Scale bar: 2 mm.

6.2 Low R: analogy with the rigid case

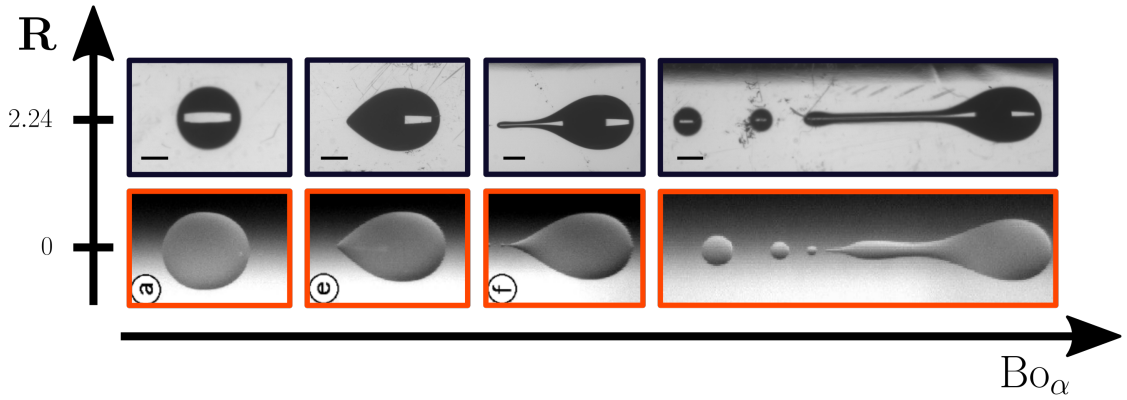

Figure 6.7: **Shapes at low R looks like that of the rigid case.** Increasing the speed, the drop forms a corner and eventually destabilizes. For U90 (**R** = 2.24), $Bo_\alpha = 0.10, 0.24, 0.27, 0.41$. scale bars: 2 mm. Pictures for the rigid case (**R** $\longrightarrow$ 0, bottom line) are taken from [97].

The fact that we observe shapes at $\mathbf{R} \sim 2$ that are close to that of the rigid case is encouraging: we obtain support for the fact that $\mathbf{R}$ can indeed be a guide to select systems depending on where we want dissipation to occur, offering control over shapes. However, these observations are also surprising since we are in a case where dissipation in the liquid is comparable rather than greater than the dissipation in the solid. Here we discuss the extent to which both the rigid case and the low-$\mathbf{R}$ one are similar.

Figure 6.7 juxtaposes top views that we obtain at $\mathbf{R} \sim 2$ with those obtained by *Podgorski & al.* [97]. In both cases, the sequence of shapes is similar. Droplets are circular at low Bo_α. Then their trailing edge transforms into a corner. Beyond a critical Bond number, the corner zone elongates, becoming a cusp, and pearls are left behind the main droplet. Closer examination reveals differences. The corner is sharper in the rigid case than in the soft case. A measure of the radius of curvature of the corner in both cases indicates that $\mathrm{R}_{\mathrm{curv}} \simeq 400$ µm in the soft case (see Fig. 6.7, second picture on the top row), while $\mathrm{R}_{\mathrm{curv}} \simeq 50$ µm in the rigid case [98].

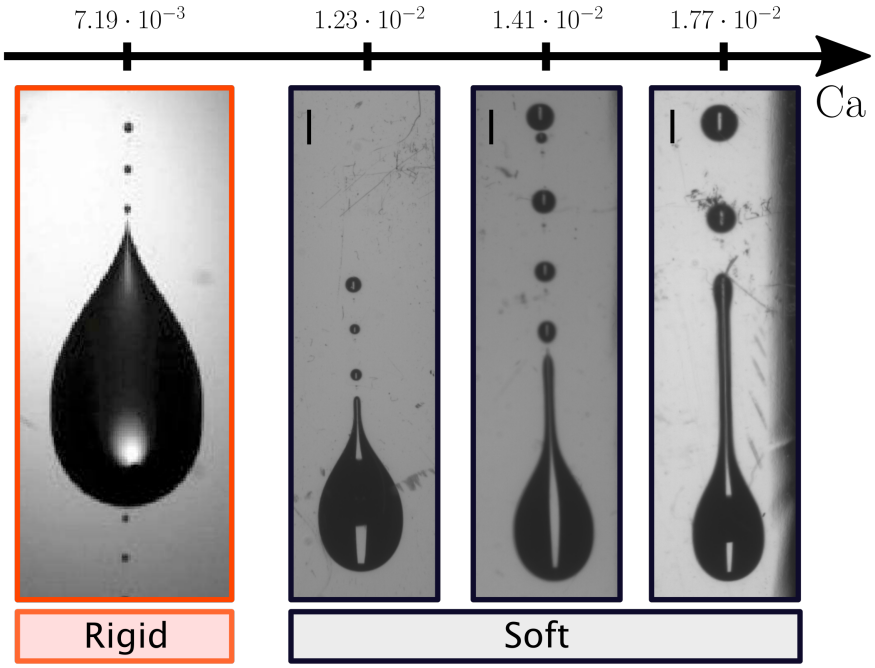

Figure 6.8: **Pearl patterns of our low-R system.** A droplet of U90 leaves bigger pearls than a droplet of silicone oil on a fluoro-treated silicon wafer just above the instability threshold. The size of the pearls also increases with Ca. For U90, $\mathrm{Bo}_\alpha = 0.272, 0.329, 0.409$. Scale bar: 2 mm. Picture for the rigid case (left, $\mathrm{Ca} = 7.19 \cdot 10^{-3}$) is taken from [74].

The pearl pattern also has features that call for a comparison with the rigid case. Just above instability, a drop sliding onto a rigid substrate breaks into smaller droplets than a drop sliding onto a soft substrate (Fig. 6.8). We measure pearls with radius $\mathrm{R} = 500$ µm for the first unstable experiment at $\mathbf{R} \sim 2$ (drop sliding at $\mathrm{Ca} = 1.23 \cdot 10^{-2}$) while *Le Grand & al.* report droplets with radius $\mathrm{R} = 125$ µm (drop sliding at $\mathrm{Ca} = 7.19 \cdot 10^{-3}$)[1]. We also point out that the critical value of the capillary number Ca_u beyond which the pearling instability occurs is larger when the substrate is viscoelastic: $\mathrm{Ca}_\mathrm{u} = (-7.13 \pm 1.64) \cdot 10^{-3}$ for the rigid case[2] versus $\mathrm{Ca}_\mathrm{u} = (-11.36 \pm 0.92) \cdot 10^{-3}$ for U90. Figure 6.8 illustrates that the size of the pearls, along

[1] We give the radius of the first pearl in the picture at $\mathrm{Ca} = 1.23 \cdot 10^{-2}$ and $\mathrm{Ca} = 7.19 \cdot 10^{-3}$.

[2] We average reported values in refs. [74, 96] for silicone oils with different viscosities ($2 \geq \eta \geq 1040$ mPa s).

with the width and length of the tail, increases as Bo_α increases. These observations are reminiscent again of those made by *Podgorski et al.* (Fig. 3.2). Some patterns seem to be built around a subpattern made of a large droplet accompanied by a small one ($Ca = 1.41 \cdot 10^{-2}$). Pearls can even be big enough to slide, and there are no remaining pearls at the end of the experiment (Fig. 6.9).

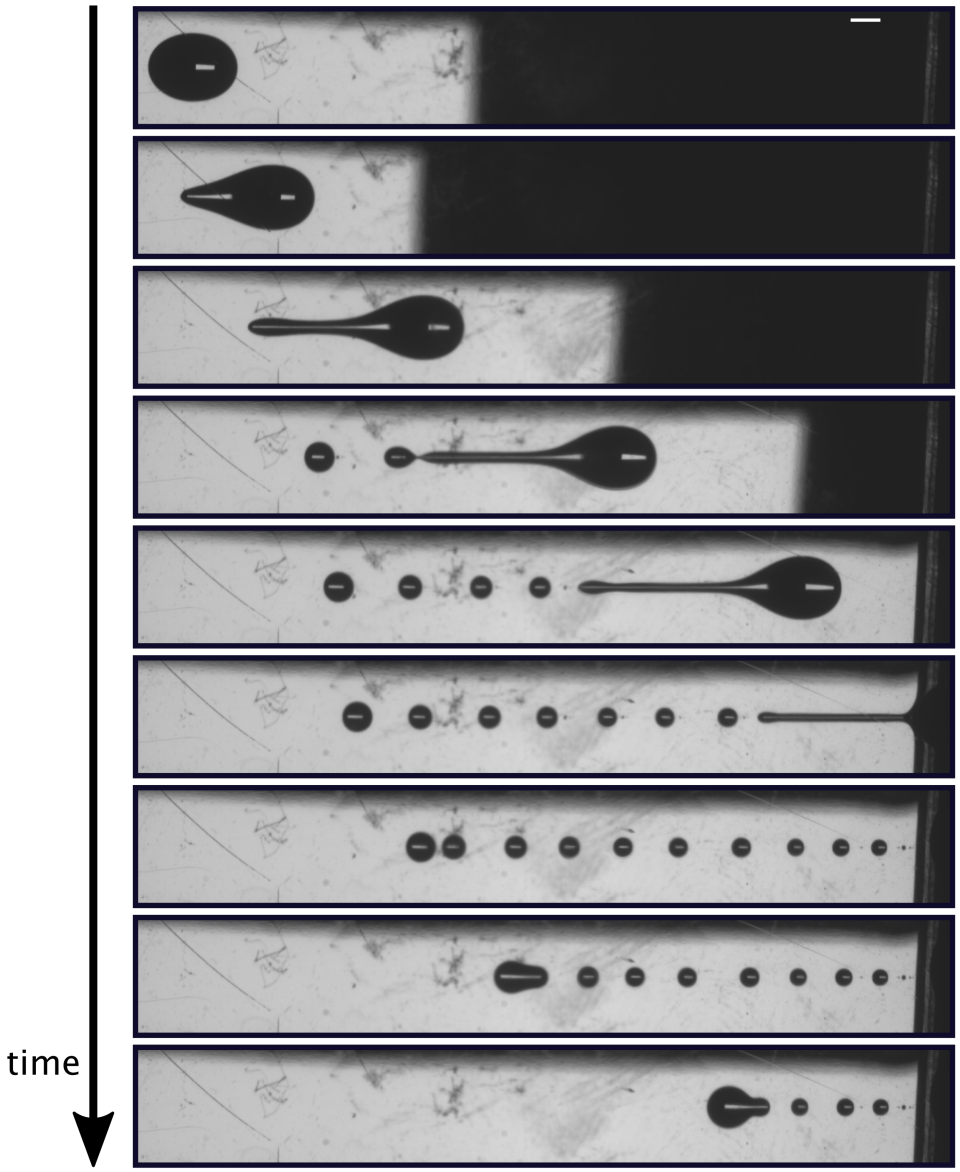

Figure 6.9: **Droplets and pacgums.** The liquid is U90, **R** = 2.24 and $Bo_\alpha = 0.409$. The droplet grows an elongated tail that breaks into smaller droplets. In this particular case, pearls are big enough to slide and merge into a single drop. scale bar: 2 mm. .

6.3 Large R: new shapes and a signature of soft hysteresis.

To the best of our knowledge, a systematic description of the shape and dynamics of droplets running down an inclined plane coated with a viscoelastic layer do not exist, even moreso when dissipation occurs in the solid. The shapes that we observe are distinct from those

that we described in Sec. 6.2. Their careful analysis even provides the first insights into the compatibility of *Dervaux et al.'s* predictions with experimental observations.

We have already pointed out that transfer of dissipation mostly to the solid phase leads to rounder trailing edges. An interesting feature of most of these droplets, peanut-shaped or not, is that the region connecting the advancing and receding parts of the contact line has a large, if not infinite, radius of curvature, as we noted earlier (see images of the systems for which $\mathbf{R} \geq 100$ at intermediate and large values of Bo_α in Fig. 6.3). As we are going to see below, this property of the droplet contour is actually the first experimental evidence of soft hysteresis.

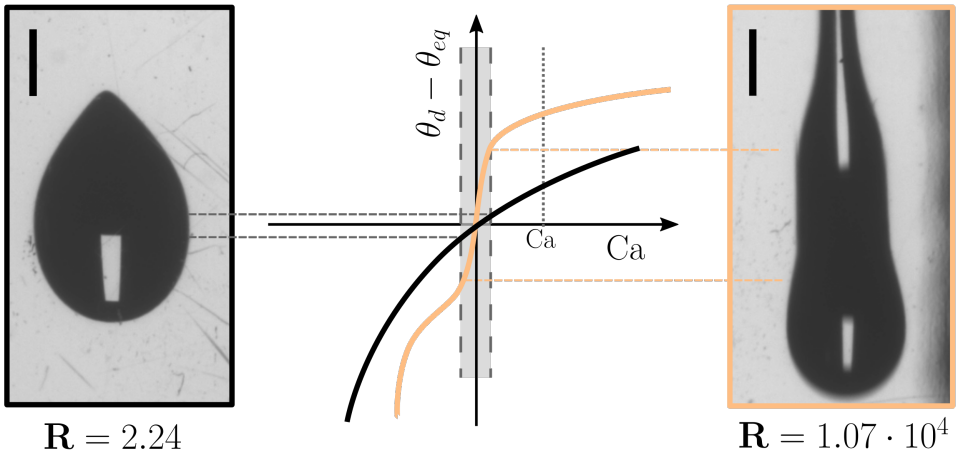

Figure 6.10: **Mechanism of *soft hysteresis*.** Two drops slide onto a viscoelastic solid with the same Ca_0 but a different **R**. The larger **R**, the larger the range of angles available at low Ca (gray patch). As low Ca liken to the contact lines almost paralell to the motion, the drop elongates. Left and right images illustrate that the zone where the contact line is paralell to the overall motion increases with **R**. Scale bar: 2 mm.

Past studies showed that measuring the contact angle along the contour of the droplet provides a way to obtain the full curve relating θ_d and Ca [73, 77], including contact angle hysteresis. The latter manifests itself when the contact line becomes still. In the context of sliding droplets, given that fluid velocity inside the droplet is always perpendicular to the contact line and its magnitude depends on the angle between the contact line and the overall motion, velocity vanishes when the contact line is orthogonal to the motion of the droplet. For an ideal system, we then have $\theta_d = \theta_{eq}$. However, in the presence of hysteresis, the contact angle is comprised in the range $\theta_{s,r} < \theta_d < \theta_{s,a}$, with $\theta_{s,a}$ and $\theta_{s,r}$ the advancing and receding hysteresis contact angles, so long as the velocity is 0. As a consequence, the contact line is a straight line paralell to droplet motion. The drop then elongates.

Applying a similar rationale to our images, we can observe portions of the contour of our droplets that look straight or almost straight. Now, if we go back to Fig. 2.14, we see that the region around Ca = 0 encompasses a large range of contact angles. Assuming that this apparent effect should lead to an effect similar to that of actual contact angle hysteresis, we would expect the droplet to have long straight sides. Figure 6.10 shows that droplets do have long straight portions on their contour in the extreme case $\mathbf{R} \sim 10^4$.

Chapter 7

Dynamics

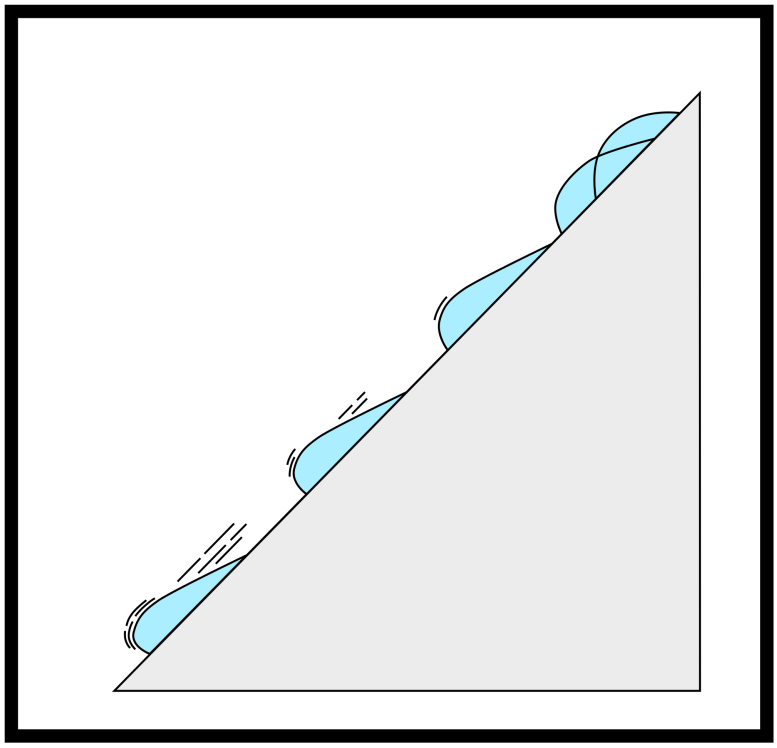

7.1 Energy balance at the scale of the droplet

As we have seen in Chap. 3, we can interrogate the system of a droplet sliding on the surface of a solid in terms of how much energy is dissipated, quantified by the capillary number Ca, as a function of injected energy, quantified by the Bond number Bo_α. This comparison is based on observations at the scale of the droplet, as they require that we measure the weight of the droplet and its velocity down the inclined plane. We process top views to obtain these datasets.

The reader should note that each {solid; liquid} system keeps the same color and marker throughout the whole manuscript, filled symbols always referring to unstable droplets in the pearling regime.

7.1.1 General comments

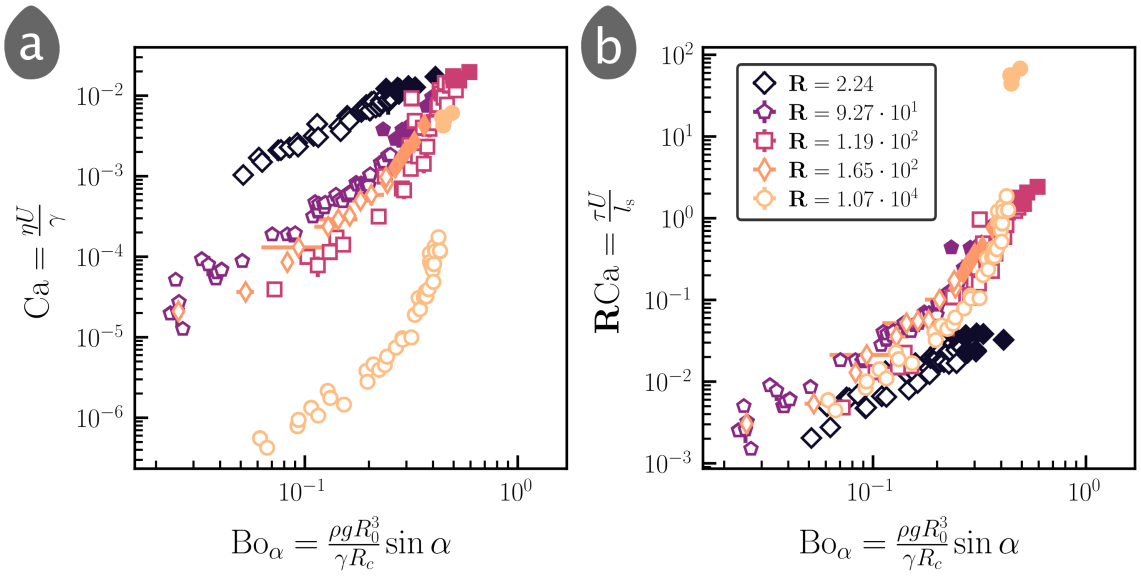

Figure 7.1: **Dissipation ratio R rules dynamics.** Non-dimensional weight-speed diagram when the characteristic speed of (a) the liquid U_l or (b) the solid U_s normalizes the running speed U. Different laws characterize datasets when energy mostly dissipates in the liquid or in the solid. Solid capillary number **R**Ca better collapses our data.

Two channels of energy dissipation exist in our system, either *via* the liquid or *via* the solid. Thus, two basic plots may represent the balance between dissipation and injected energy. The first one is similar to that of the rigid case, where the evolution of Ca is reported as a function of Bo_α (Fig. 7.1a). Data for all the liquids span four orders of magnitude in Ca in this representation. The curves shift downwards with increasing **R**. This shift is direct evidence of viscoelastic braking [27, 80, 81, 81, 82]: for a given droplet weight, the larger **R**, the more the solid dissipates and the slower the droplet moves. We can also see that the functional form linking Ca to Bo_α differs depending on the value of **R**.

The other representation, in terms of the solid capillary number **R**Ca (Fig. 7.1b), provides a clearer view leading to the grouping of data in two groups. The data for $\mathbf{R} \sim 2$ reside in the bottom part of the graph, while other datasets obtained at $\mathbf{R} \ll 1$ almost collapse on a master curve. Careful analysis shows that glycerol-based droplets collapse with each other

while PEG-*ran*-PPG ME-based droplets form another population, despite similar values for **R**.

7.1.2 Low-R sliding

Once again, we compare low-**R** data with *Podgorski & al.*'s data [97]. To make the discussion possible, we calculate the Bond number of their experiment with Eq. 6.7. Figure 7.2a shows the capillary number of the experiments follow the same trend with respect to the Bond number. This observation supports the similarity between the two systems that we had suggested when analyzing droplet shapes in the previous chapter (Fig. 6.7).

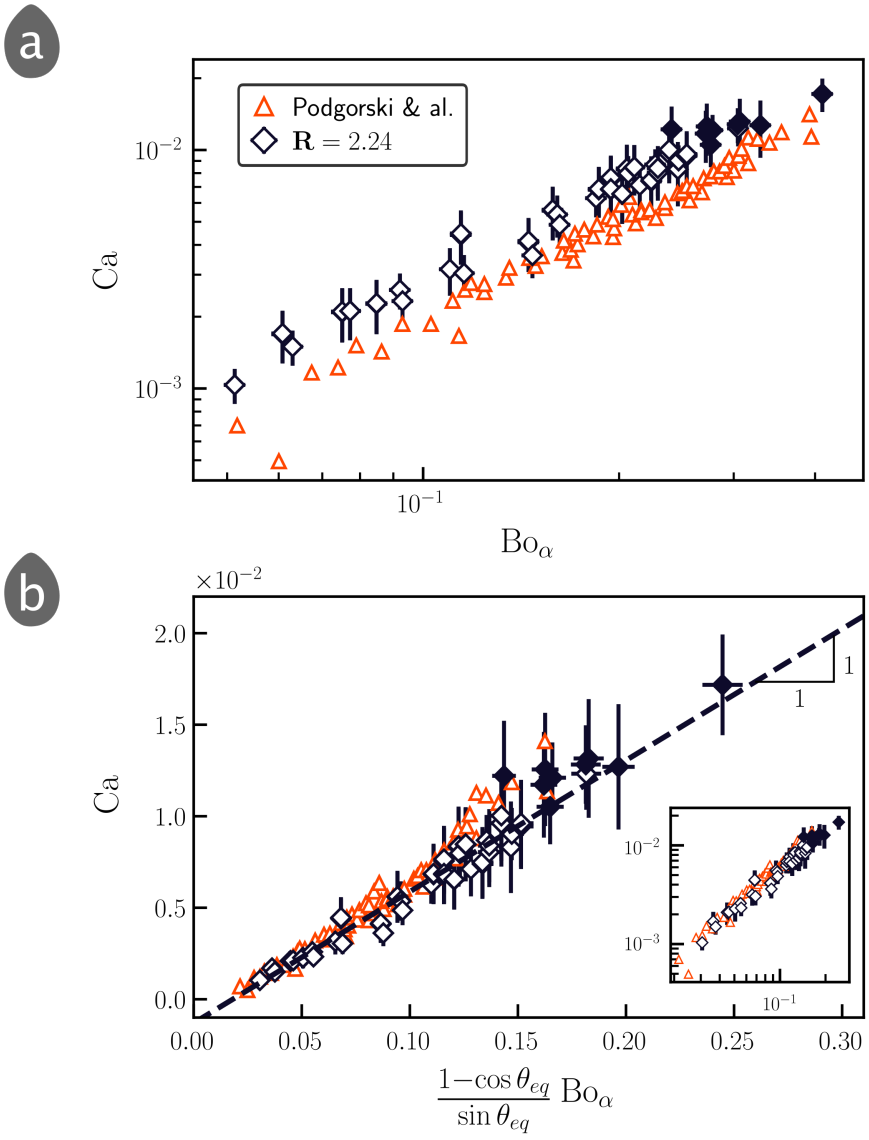

Figure 7.2: **Weight-speed relationship when energy mostly dissipates inside the liquid.** (a) As in the rigid case [97], a single regime rules the dynamics. (b) Datasets overlap with a suitable θ_{eq} correction. An affine law (dashed line) shows that the dissipation inside the liquid drives the dynamics. Inset: the same plot in logarithmic scale.

A closer examination of Fig. 7.2a shows that *Podgorski & al.*'s data lie below ours in the $\mathrm{Ca}-\mathrm{Bo}_\alpha$ parameter space. We expect that droplets with equivalent Bond numbers should be

slower in our system than in *Podgorski & al.*'s because the substrate also dissipates energy. But as we will see below, the scaling relating Ca to Bo_α can be refined to account again for contact angle effects.

To derive this refined balance, we assume that dissipation in the liquid balances the force of gravity on the droplet:

$$\rho g \mathrm{R}_0^3 \sin\alpha \sim \eta \frac{\mathrm{U}}{h} \mathrm{R}_c^2 \tag{7.1}$$

where $\mathrm{U}/h = \dot{\gamma}$ estimates the velocity gradient in the droplet and R_c^2 is the area of the contact between the drop and the substrate. Using Eqs. 6.3 and 6.6, we obtain:

$$\frac{\mathrm{R}_c^2}{h} = \mathrm{R}_c \frac{\sin(\theta_{eq})}{1-\cos(\theta_{eq})} \tag{7.2}$$

Dividing both sides of Eq. 7.1 by liquid-vapor surface tension γ and replacing R_c^2/h, we obtain:

$$\frac{1-\cos(\theta_{eq})}{\sin(\theta_{eq})} \mathrm{Bo}_\alpha \sim \mathrm{Ca}. \tag{7.3}$$

We observe that this correction leads to data overlap (Fig. 7.2b, the inset shows that the collapse works for the whole range of our data). Moreover, experiments support the finding of proportionality between Ca and Bo_α. Thus our observations provide strong evidence that dissipation in the liquid must be accounted for in this system.

Scaling law 7.3 predicts a linear relationship between Bo_α and Ca. However, *Podgorski & al.* predict an affine law (Eq. 3.1) that can be rewritten as:

$$\frac{1-\cos(\theta_{eq})}{\sin(\theta_{eq})} \mathrm{Bo}_\alpha \sim \mathrm{Ca} - \mathrm{Ca}_{\mathrm{hyst}}. \tag{7.4}$$

The y-intercept represents the effect of contact angle hysteresis $\Delta\theta = \cos\theta_{s,r} - \cos\theta_{s,a}$. Droplets are pinned to the surface if the contact angles remain in the range of the contact angle hysteresis, leading to the existence of a minimal value for the Bond number to observe motion [97]. Fitting our data with an affine law (Fig. 7.2b), we find $\mathrm{Ca}_{\mathrm{hyst}} = (2.3 \pm 0.1) \cdot 10^{-2}$ for both systems. Interpretation of this finding in our parameter space requires that we account for the contribution of the equilibrium contact angle on the hysteresis term. Doing so, we find:

$$\mathrm{Ca}_{\mathrm{hyst}} = \frac{1-\cos(\theta_{eq})}{\sin(\theta_{eq})} \Delta\theta \tag{7.5}$$

For U90, we find that the contact angle hysteresis is about 2.3°, a value consistent with the small hysteresis usually reported for these systems [43, 91, 99]. It is also compatible with our measurements, which are plagued with a measurement accuracy on contact angle measurements that is larger than this estimate of $\Delta\theta$. The same procedure applied to *Podgorski & al.*'s datasets provides an estimate of 4.8° for contact angle hysteresis, in good agreement with their measurement.

7.1.3 Large-R sliding

We expect that the relation between injected energy and dissipation is modified when the effective viscosity of the solid exceeds liquid viscosity. We see in Fig. 7.1 that the functional form relating Bo_α and Ca at large values of **R** differs from that observed at small values. We also know that **R**Ca is likely a good metric, as curves almost collapse on a single curve when

plotted in the $\mathbf{R}\mathrm{Ca} - \mathrm{Bo}_\alpha$ space (Fig. 7.1)b). Besides, we know from the previous section that the equilibrium contact angle matters. Hence we should derive a scaling law for the solid-dominated case that accounts for all of these modifications.

Inspired by ref. [44], we estimate the power dissipated per unit of volume of the solid when the drop moves by a length ℓ:

$$p_{\mathrm{diss}} \sim \sigma \epsilon^2 \omega \tag{7.6}$$

with σ the viscous stress, ϵ the strain and ω the pulsation. Using the Chasset-Thirion model (Eq. 2.32), we have the following estimate for viscous stress:

$$\sigma \sim \mu_0 \left(\frac{U\tau}{l_s} \right)^m. \tag{7.7}$$

Besides, we take:

$$\epsilon \sim \frac{\gamma}{\gamma_s} \sin(\theta_{eq}) \tag{7.8}$$

and:

$$\omega = \frac{U}{l_s}. \tag{7.9}$$

Then we have:

$$p_{\mathrm{diss}} = \mu_0 \left(\frac{U\tau}{l_s} \right)^m \left(\frac{\gamma}{\gamma_s} \sin(\theta_{eq}) \right)^2 \frac{U}{l_s} \tag{7.10}$$

Dissipation takes place in a volume that we assume to be a torus of radius R_c, width l_s and height l_r. As elasticity balances the vertical component of the resulting capillary force at the contact line $\gamma \sin(\theta_{eq})$, the height of the ridge scales as:

$$l_r \sim \gamma \sin \theta_{eq} / \mu_0. \tag{7.11}$$

Then, we estimate dissipated power:

$$\mathscr{P}_{\mathrm{diss}} \sim \sigma \epsilon^2 \omega R_c l_r l_s \tag{7.12}$$

$$\sim 2\mu_0 U R_c l_s \left(\frac{\gamma}{\gamma_s} \sin(\theta_{eq}) \right)^3 \left(\frac{U\tau}{l_s} \right)^m \tag{7.13}$$

Now, we can write the force balance that a droplet sliding on a viscoelastic substrate must obey. Dividing $\mathscr{P}_{\mathrm{diss}}$ by the sliding velocity U, we have:

$$\rho g R_0^3 \sin(\alpha) \sim 2\mu_0 R_c \ell \left(\frac{\gamma}{\gamma_s} \sin(\theta_{eq}) \right)^3 \left(\frac{U\tau}{l_s} \right)^m. \tag{7.14}$$

Dividing by the liquid-vapor surface tension γ into both sides and rearranging, we obtain:

$$\mathrm{Bo}_\alpha \sim \frac{2\mu_0 l_s}{\gamma} \left(\frac{\gamma}{\gamma_s} \sin(\theta_{eq}) \right)^3 \left(\frac{U\tau}{l_s} \right)^m \tag{7.15}$$

and using:

$$\frac{U\tau}{l_s} = \mathbf{R}\mathrm{Ca}, \tag{7.16}$$

we end up with the following prediction:

$$\boxed{\mathrm{Bo}_\alpha \sim \left(\frac{\gamma}{\gamma_s} \right)^2 \sin^3(\theta_{eq}) (\mathbf{R}\mathrm{Ca})^m} \tag{7.17}$$

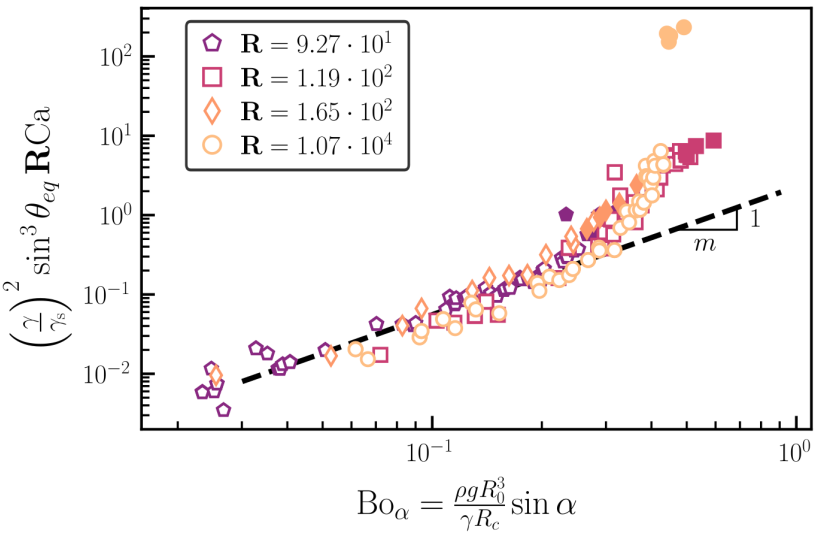

Figure 7.3: **Energy balance in the case of solid-dominated dissipation** All curves superimpose once plotted in the parameter space **R**Ca – Bo_α . Dashed line: fit with Eq. 7.17. Data deviate from the m-power-law regime when **R**Ca approaches 1.

Eq. 7.17 suggests that prefactor $[(\gamma/\gamma_s)\sin(\theta_{eq})$ should capture the dependence on equilibrium contact angles. *PEGs* and *Glycerols* collapse when this prefactor corrects the (Bo_α - **R**Ca) space – Different wetting properties shift our data in the (Bo_α - **R**Ca) space.

Figure 7.3 shows that all the data that we have obtained collapse on a single curve. The dependence on the specifics of the liquid is removed. We see that Eq. 7.17 is compatible with data in the region $10^{-2} < (\gamma/\gamma_s)^2 \sin^3(\theta_{eq})\mathbf{R}\mathrm{Ca} < 3 \cdot 10^{-1}$. However, the scaling fails when $(\gamma/\gamma_s)^2 \sin^3(\theta_{eq})\mathbf{R}\mathrm{Ca} \geq 3 \cdot 10^{-1}$. The functional form is not a power law anymore, at least not an obvious one in this representation.

7.2 Energy balance at the scale of the contact line

The approach employed in the previous section relies on a balance between energy injected in the system assumed to be of the gravitational kind and energy dissipated *via* viscous processes. Another view of this problem that forms the basis of the Cox-Voinov relation in the rigid case is to balance energy injected in the system due to a gradient of Laplace pressure and dissipation. Characterization of this balance requires that we measure the dynamic contact angle θ_d as a function of the velocity U of the droplet, and then transform the latter into a non-dimensional quantity that can be the liquid capillary number Ca or its counterpart for the solid, **R**Ca.

Figure 7.4a shows at a glance that the functional form of the relation between dynamic contact angle and capillary number depends on **R**. This dependence is qualitatively similar to the prediction of *Dervaux et al.* (Fig. 2.14) [62]. When dissipation inside both the liquid and the solid are of the same order of magnitude, $\mathbf{R} = 2.24$, the curve is reminiscent of that of the rigid case (Fig. 3.3 [71, 77]: the advancing and receding branches are close to each other, and the slope is a bit steeper for the receding branch. The smoothness of the curve around $\mathrm{Ca} = 0$ confirms that our gel shows little to no contact angle hysteresis (at least with our accuracy on θ_d), in agreement with previous observations [43, 99].

For values of $\mathbf{R} \gg 1$, the advancing and receding branches separate around $\mathrm{Ca} = 0$. We

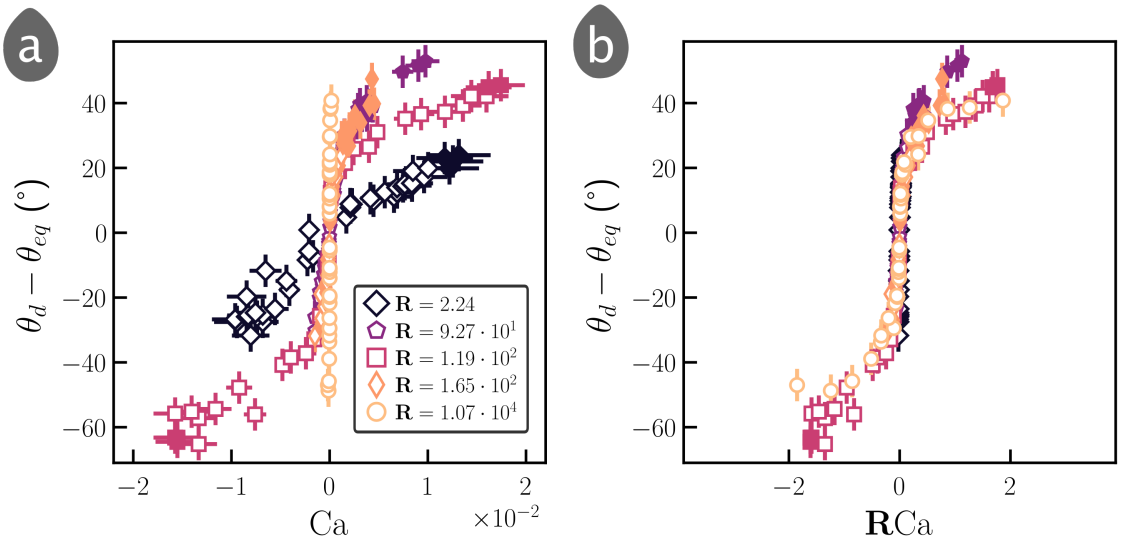

Figure 7.4: **Dissipation ratio R sets the relationship between θ_d and speed U.** (a) Dynamic contact angle θ_d as a function of liquid capillary number Ca. Normalizing with equilibrium contact angle θ_{eq} centers the curves. Receding (Ca < 0) and advancing (Ca > 0) branches separate as **R** increases. (d) The curves overlay when plotted as a function of solid capillary number **R**Ca.

even obtain a vertical curve when $\mathbf{R} \sim 10^4$, *i.e.* when dissipation in the solid dominates. The steep slope at low velocity for high **R** data at large **R** is akin to contact angle hysteresis on solid surfaces, with the difference that the transition of contact angle values between the advancing and receding branches is continuous.

The curves collapse on an S-shaped master curve when we plot the deviation of the contact angle from equilibrium $\theta_d - \theta_{eq}$ as a function of the solid capillary number **R**Ca (Fig. 7.4b). In this parameter space, the advancing branch is separated from the receding branch by a portion with a steep slope for all systems. Both branches have slopes much smaller than this portion, and even seem to flatten at higher **R**Ca.

7.3 Instability threshold

Finally, we would like to describe observations and measurements obtained at the threshold of the pearling instability. Indeed, two other properties of sliding droplets depend on dissipation ratio **R**, the capillary number at the onset of pearling Ca_u and the associated receding contact angle θ_u. In what follows, we consider the absolute value of Ca_u, as its minus sign is of no relevance to our discussion.

Threshold capillary numbers seem scattered at first glance (Fig. 7.5a). However, the focus must be given to trends in systems where a single parameter is varied at once, either θ_{eq} or **R**. Then, the solid arrow indicates that $|\mathrm{Ca_u}|$ decreases when we decrease θ_{eq} at **R** =cst. As we see on Fig. 7.5b, the threshold receding contact angle θ_u is identical for the systems that we discuss now, for which $\mathbf{R} \sim 160$. As **R** =cst, the difference between the equilibrium and the dynamic contact angles $\theta_d - \theta_{eq}$ at a given speed U is also the same. Thus the system with the smallest θ_{eq} reaches θ_u sooner, *e.g.* at a smaller receding speed.

We see that θ_u has a finite value at the pearling transition (Fig. 7.5a). Other groups found a non-zero θ_u in the rigid case [77, 78]. This observation is rather surprising as the liquid deposition is expected when the receding contact angle decreases to 0. Non-zero values

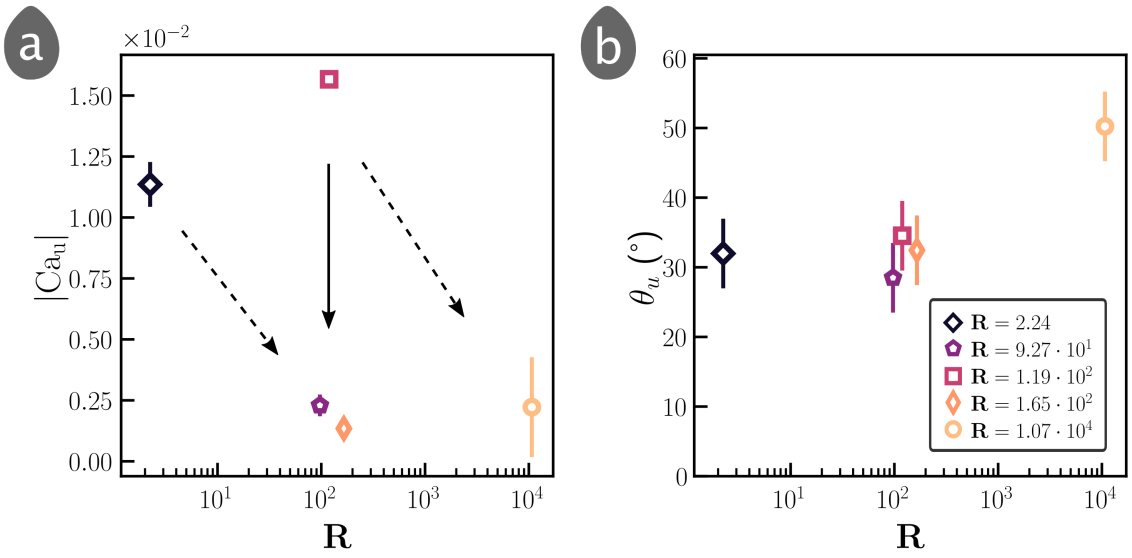

Figure 7.5: **The Capillary number and the dynamic angle at instability threshold.** (a) The absolute value of critical liquid capillary number Ca_u in function of **R**. $|Ca_u|$ decreases when **R** increases at constant θ_{eq} (dashed arrows) and when θ_{eq} decreases at constant **R** (solid arrow). (b) Critical receding contact angle θ_u as a function of the dissipation ratio **R**. θ_u stays close to 30° except for $\mathbf{R} = 1.07 \cdot 10^4$ (G60), where it is equal to 50°.

for θ at the threshold were attributed to small defects on the surface of the substrate that could destabilize the drop sooner than expected. In our case, the liquid-like behavior at the molecular scale of our material [14] should promote defect-free surfaces for our gels, provided the gel is well prepared. Thus, we conclude that the receding contact angle remains finite at the pearling transition, with or without defects.

For most systems, the value of the contact angle at the pearling instability threshold remains constant, $\theta_u \simeq 32°$, while **R** increases by two orders of magnitude. This value is comparable to that reported in the rigid case, of the order of ~ 40°. Note that a related deposition transition is described when a plate is withdrawn from a bath of liquid, the celebrated "dip-coating" geometry. In this case, the value of θ_u is ~ 25° [78], slightly smaller than in the sliding droplet experiments.

The value of θ_u for $\mathbf{R} \sim 10^4$ is larger than all the others. This difference may stem from the difficulty that we encounter in defining the threshold for the pearling instability of this system. As we can see in Fig. 7.5a, the uncertainty on Ca_u for $\mathbf{R} \sim 10^4$ is very large. This uncertainty exists because the system jumps abruptly from a stable regime at a given Ca to an unstable regime with a much larger Ca. This jump can be seen in Fig. 7.3: the open dots and the filled ones are separated by one order of magnitude along the ordinate axis. Hence, we chose the mean between the last stable and the first unstable capillary numbers, which gives $Ca_u \sim (2.2 \pm 2.0) \cdot 10^{-3}$. We report the dynamical receding contact angle of the last stable drop for θ_u. We have $\theta_u \simeq 50°$, corresponding to $Ca \sim 1.7 \cdot 10^{-4}$. It is possible that this value overestimates the actual critical value.

Chapter 8

Discussion

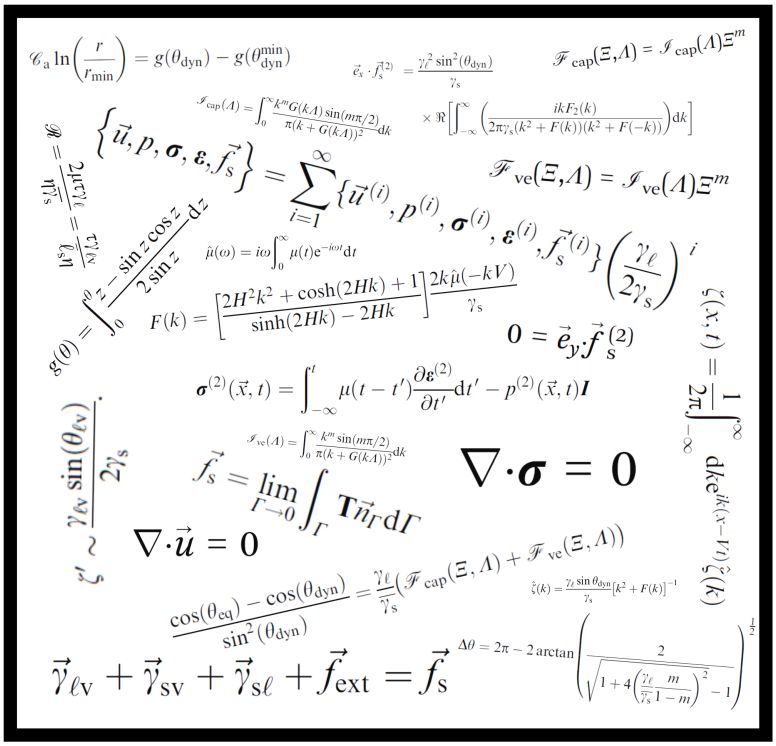

8.1 R ~ 2: dynamics in the light of the Cox-Voinov law

We have seen in the previous chapter that droplets sliding on substrates at **R** ~ 2 have shapes and dynamics that are similar to those observed in the case of a rigid non-dissipative substrate. In particular, the relation between the Bond and the capillary number for both systems superimpose (Fig. 7.2). The relation between dynamic contact angles and Ca of both systems also look alike. It is described by the Cox-Voinov relation in the case of the rigid substrate, the form of which we recall in its simplified version valid for $\theta_d \leq 3\pi/4$:

$$\boxed{\theta_d(h)^3 - \theta_d(h_{\min})^3 = 9\,\mathrm{Ca}\log\left(\frac{h}{h_{\min}}\right)}. \tag{8.1}$$

where h and $h_{\min}$ are the height at which the angle is measured on the droplet-atmosphere interface and the microscopic cutoff length to circumvent stress divergence respectively. We can try and extract the magnitude of $h_{\min}$ obtained in the gel case by testing Eq. 8.1 against θ_d – Ca data for **R** ~ 2 (Fig. 7.4a).

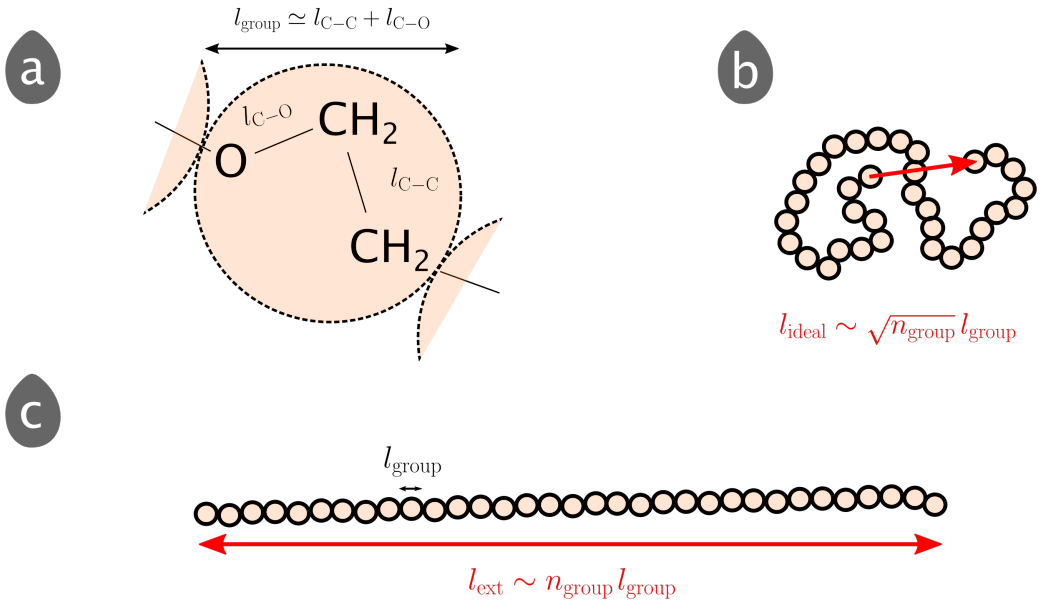

Figure 8.1: **Estimation of the size of a polymer.** The polymer contains n_{group} monomers of size l_{group}. (a) A monomer of oxyethylene. We sum the lengths of the chemical bonds l_{C-C} and l_{C-O} to approximate l_{group}. The size of the whole molecule a is between that of (b) an ideal chain $l_{\mathrm{ideal}} \sim \sqrt{n_{\mathrm{group}}}\, l_{\mathrm{group}}$ and that of (c) a fully extended chain $l_{\mathrm{ext}} \sim n_{\mathrm{group}}\, l_{\mathrm{group}}$.

Given our spatial resolution, we take h = 100 µm. Following refs. [71, 74], we estimate that the microscopic cut-off length is the size of a liquid molecule a. U90 is a polyalkylene glycol containing respectively 75 wt% oxyethylene and 25 wt% oxypropylene groups. It has an average molecular weight of $M_w = 1.20 \cdot 10^4\ \mathrm{g\,mol^{-1}}$ [134]. As an approximation, we will estimate the length of a chain containing 100% oxyethylene groups. Dividing by the molecular weight of an oxyethylene group C_2H_4O, $M_{w,EO} = 44\ \mathrm{g\,mol^{-1}}$), we obtain that a U90 molecule contains $n_{\mathrm{group}} \sim 272$ groups on average. The lengths of C – C and C – O bonds are equal to 1.54 Å and 1.43 Å respectively [135] (Fig. 8.1a). We sum them to approximate the length of a single oxyethylene group l_{group}. The size of the whole chain lies between the length of the extended chain l_{ext} and that of the ideal chain l_{ideal} (Fig. 8.1b and c):

$$l_{\mathrm{ext}} \sim n_{\mathrm{group}}\, l_{\mathrm{group}} \tag{8.2}$$

$$l_{\text{ideal}} \sim \sqrt{n_{\text{group}}}\, l_{\text{group}}. \tag{8.3}$$

We obtain $4.9 < l_{\text{chain}} < 81.0$ nm (and $4.3\text{ nm} < l_{\text{chain}} < 61.4$ nm when we repeat the calculation for 100% of oxypropylene groups C_3H_6O). Figure 8.2a shows that the Cox Voinov law with $h = 100\,\mu$m and $4.3 < h_{\text{min}} < 81.0$ fails to describe our data. A correct description of our data with Eq. 8.1 requires $a = 0.3$ Å, a value inconsistent with our molecular scales, and even with the molecular scale of typical materials. This value is indeed 5 times smaller than the sizes of the C−C and C−O bonds that we have used to estimate the extent of a U90 molecule.

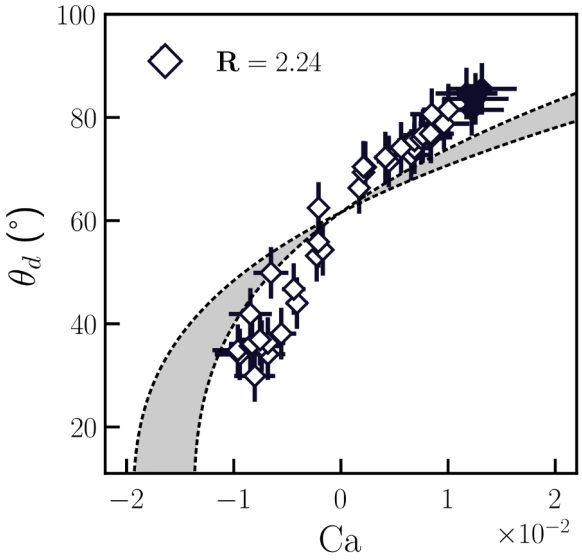

Figure 8.2: **Cox Voinov fits for U90.** The fit fails for the estimated molecular size $4.3 \leq a \leq 81$ nm (colored patch).

The approach that we have just described is flawed straight from its inception. Indeed, we have assumed that dissipation occurs in the liquid only. However, the value of **R** suggests that dissipation inside the solid is twice as much as that in the liquid. Therefore, a proper description should account for solid dissipation even in this deceiting case where the similarity to the rigid case suggests that solid dissipation is negligible. We need a more refined approach to capture our data quantitatively.

To sum up, the low **R** wetting system behaves qualitatively like the rigid case. Yet, the Cox-Voinov law fails to describe it quantitavely, and suggest a key role of the substrate.

8.2 Predictions for the dynamic contact angle

We have seen in Chaps. 6 and 7 that increasing the dissipation ratio leads to experimental $\theta_d - \text{Ca}$ curves that are in qualitative agreement with the predictions in Fig. 2.14 [62]. Now we test the quantitaive agreement between our contact angle measurements and Eq. 2.50, that we recall here:

$$g(\theta_d) = g\left(\frac{\pi}{2} + \arctan\left[\left(\frac{\sqrt{1+\mathscr{A}^2(\mathbf{R}\text{Ca},\Lambda)}-1}{2}\right)^{1/2}\right]\right) + \text{Ca}\log\left(\frac{x}{x_{\text{min}}}\right). \tag{8.4}$$

To proceed further, we have to estimate γ_s. The usual way to do so is to assume that γ_s is the mean between the solid/vapor interfacial tension γ_{sv} and the solid-liquid interfacial tension γ_{sl}. The solid/vapor surface tension of a siliconee gel should be the same for all wetting systems. A measurement based on a static wetting experiment in which $\theta_{eq} = \pi/2$ provides a value $\gamma_{sv} = 29\ \mathrm{mN\,m^{-1}}$ [51]. Then we retrieve γ_{sl} using the Young-Dupré relation. The only remaining parameter is the ratio between the macroscopic scale, usually at which contact angle measurements are performed, and the microscopic cutoff length that is necessary to avoid stress divergence. For all our systems, we measure the dynamic angle at the same height ($\sim 100-150\,\mu\mathrm{m}$). Besides, the size of a liquid molecule (~ 1 nm) and the elastocapillary length ($\sim 10\,\mu\mathrm{m}$) stays of the same order of magnitude. We enforce $x/x_{\min} = 1000$[1].

8.2.1 Extremal values of R

Figure 8.3 shows that the model captures the data well. In particular, the model is in excellent agreement with data for $\mathbf{R} = 2.24$ and $\mathbf{R} = 1.07\cdot10^4$. Both the advancing and receding branches are captured. We can also see that the model predicts a sharp slope of the data in the vicinity of $\mathrm{Ca} = 0$ even in the case $\mathbf{R} \sim 2$. Finally, the value of $x/x_{\min}$ suggests that the microscopic cutoff length is $x_{\min} \sim 100$ nm. This value is rather large compared to the typical molecular scales usually reported for liquids, and also much smaller than the elastocapillary length. As we have seen also, an attempt to fit these data with a Cox-Voinov relation that does not account for the effect of the solid fails at describing the data. Hence, the microscopic cutoff might be a compromise between the size of a liquid molecule and the elastocapillary length for elastowetting systems.

In the other well-fitted regime, $\mathbf{R} \sim 10^4$, we see that the slope is steep around $\mathrm{Ca} = 0$. This slope connects two regions where the dynamic contact angle tends to reach plateau values in both branches. Experimental plateaus seem a little flatter than predicted ones, although we need larger values of Ca along both axes to ascertain this difference.

8.2.2 Intermediate values of R

Agreement is less satisfactory when $\mathbf{R} \sim 100$. While the model captures the steep slope at low Ca for all these systems, issues arise with the branches. Experiments suggest two different causes for this disagreement that are system-dependent. In the case of pure glycerol, $\mathbf{R} = 119$, the model underestimates the receding branch. The trailing edge of the droplet experiences oscillation during its motion, making it hard to define what the value of contact line velocity and the associated receding contact angle should be. This observation, not predicted by the model at all, may explain the disagreement between model and data.

The situation with PEG-ran-PPG liquids is more complex. Not only has the model a hard time capturing the branches, the shape diagram also shows that something is happening: these droplets form sharp corners at their back (Fig. 8.4), even sharper than those observed for $\mathbf{R} \sim 2$. Moreover, the droplet leaves minuscule pearls in its wake (Fig. 6.3). Finally, the trailing edge of the droplet oscillates too, with the curvature of the droplet increasing and decreasing in cycles.

Observations of a sharp corner (Fig. 8.4a) and the deposition of small droplets (Fig. 8.4b) are reminiscent of those reported when tip streaming occurs (Fig. 8.4c) [137–139]. In this situation, a fluid-fluid interface deforms into sharp structures from the end of which droplets

[1] We could perfectly fit each system if we release this condition and allow $x/x_{\min}$ to span several orders of magnitude. We doubt it is physically relevant though.

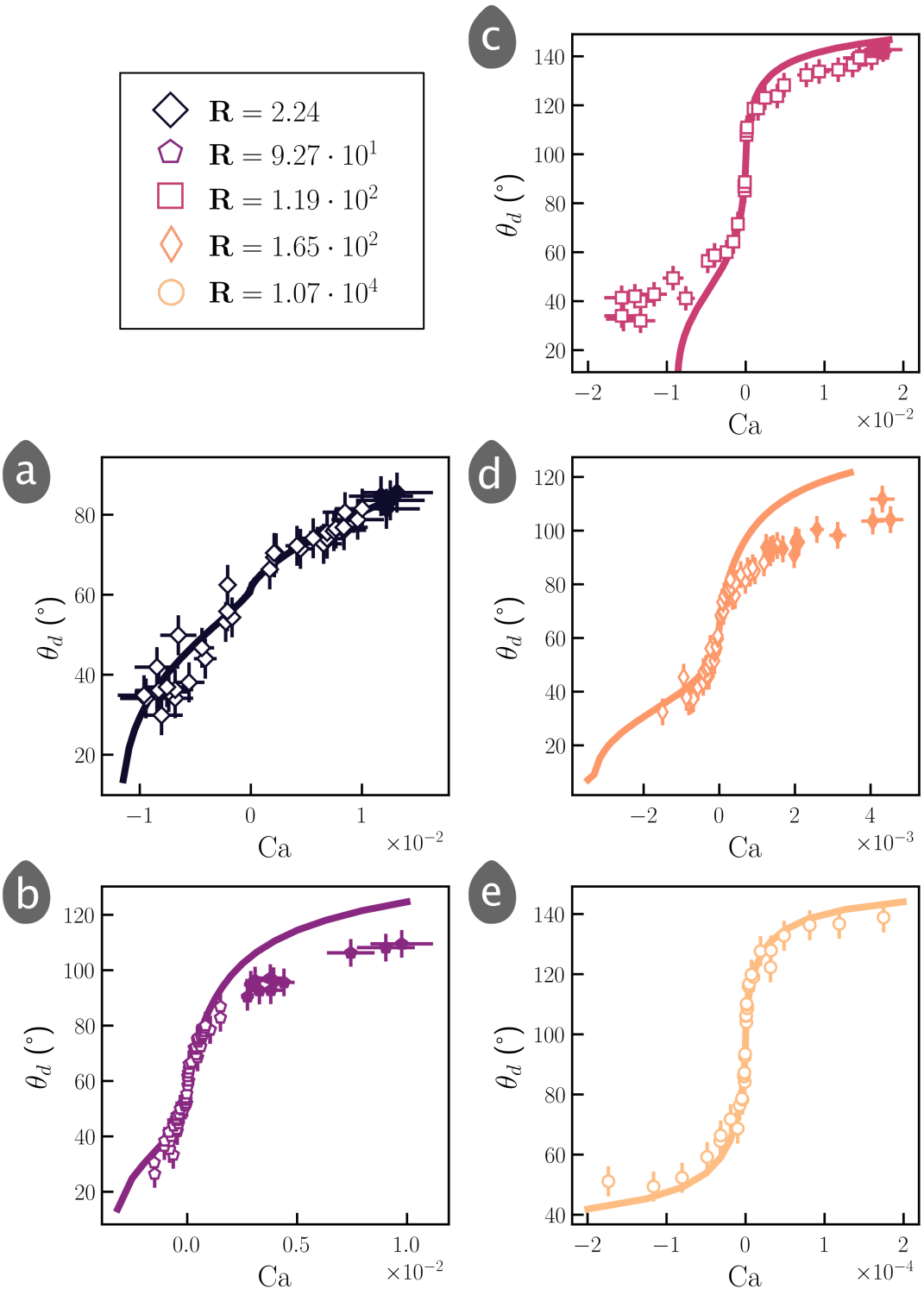

Figure 8.3: **Theory versus experiments: $\theta_d = f(\mathrm{Ca})$ curves.** Each time, the points are experimental data and the solid line is the fit of the nonlinear theory [62]. The sole fit parameter has the same value $x/x_{\mathrm{min}} = 1000$ for all systems. It suggests a microscopic cutoff $x_{\mathrm{min}} \sim 0.1$ µm, well above the usual molecular scale. (a) {SYLGARD™ 527 ; U90}; (b) {SYLGARD™ 527 ; PEG-*ran*-PPG-ME70 }; (c) {SYLGARD™ 527 ; G100}; (d) {SYLGARD™ 527 ; PEG-*ran*-PPG }; (e) {SYLGARD™ 527 ; G60}. The model fails to capture the receding branch in (c) and overestimates the advancing branch in (b,d). The agreement is excellent otherwise.

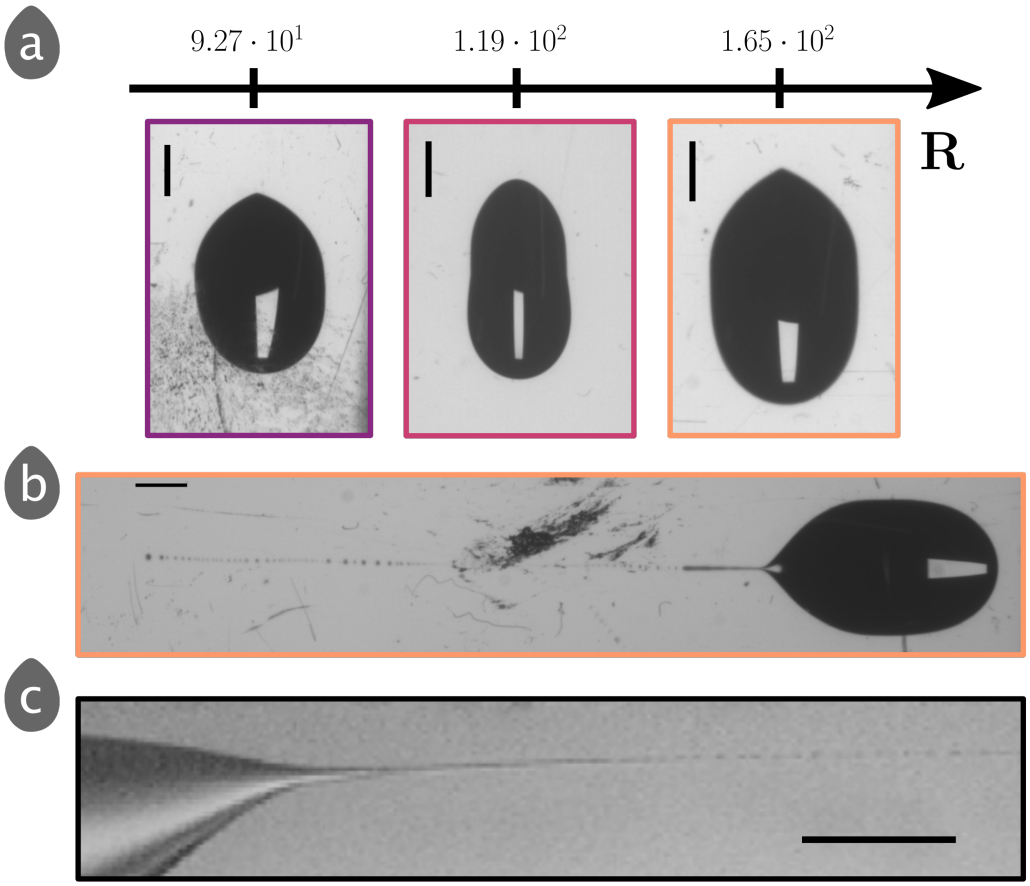

Figure 8.4: **Surfactants allow sharper interfaces.** (a) Drops sliding onto SYLGARD™ 527 at $\mathbf{R} \sim 10^2$ (from left to right: PEG-*ran*-PPG-ME70 ; glycerol; PEG-*ran*-PPG). The glycerol is rounder than the *PEGs*. The surfactants might lower the interfacial energy and thus the energy cost of the corner – the latter sharpens. Scale bars: 2 mm. (b) Unstable drop of PEG-*ran*-PPG ($Bo_\alpha = 0.311$). Scale bar: 2 mm. The thin filament at the rear and the tiny droplets are reminiscent of tip streaming. (c) Tip streaming in a Couette device. A drop of water is surrounded by a one-thousand-fold more viscous silicone oil. The angular frequency of the Couette device is 19.5 s^{-1}. Adding surfactants allows a thin filament to develop. Scale bar: 100 µm [136, 137].

can be emitted. Observations of this process have been reported in the presence of an electric field or surfactants. In the latter case, these sharp structures are promoted by surfactant accumulation at some location along the fluid/fluid interface because of flow inside the droplet. This accumulation leads to a lowering of the energy cost to curve the interface. Then filaments and corners can grow (Fig. 8.4c). We have investigated whether PEG-*ran*-PPG and PEG-*ran*-PPG ME-based liquids could be thought of as surfactant solutions.

To test this hypothesis, we perform a simple experiment in which we release a droplet of liquid on a layer of water covered with peppercorns. We carry out this test with all the liquids that we use. If one liquid contains surfactants, the deposition of a droplet on the surface of water decreases surface tension locally and induces a surface tension gradient. A stress arises along the air/water interface, and fluids move on both of its sides (Fig. 8.5). This flow is known as the Marangoni effect [140].

We detect a Marangoni effect for both of the PEG-ran-PPG-based liquids. Figure 8.5b shows an example of the flow visualization for pure PEG-ran-PPG-ME. Its aqueous solution,

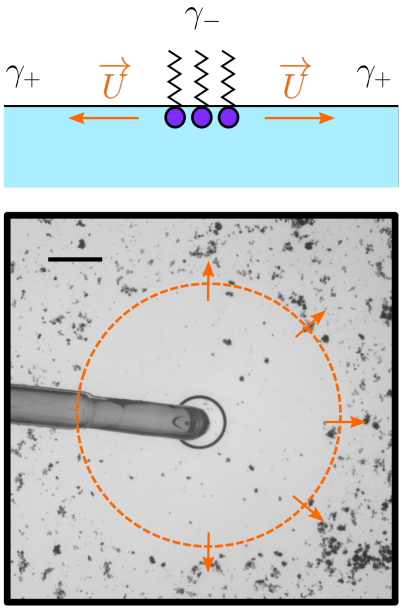

Figure 8.5: **Marangoni effect.** Top: if the deposited liquid contains surfactants, the lower surface tension γ_- at the point of deposition creates a Marangoni flow towards the region of higher surface tension γ_+. Bottom: release of a drop of PEG-*ran*-PPG-ME70 on pepper-sprinkled water. The Marangoni flow advects peppercorns outward. Orange dashed circle and arrows illustrate this radial flow. Scale bar: 5 mm.

PEG-*ran*-PPG-ME70 , can be considered as a surfactant solution. This observation also explains why we measured a surface tension of $\gamma = 37$ mN m^{-1} for both PEG-*ran*-PPG-ME and PEG-*ran*-PPG-ME70 : even though water is added to the base liquid, PEG-ran-PPG-ME molecules cover the interface with air, and they bring down surface tension to a value that we notice to be identical to that of pure PEG-*ran*-PPG-ME. While we use the other PEG-ran-PPG-based liquid as received, its hygroscopic nature suggests that it contains some amount of water that may well lead to surface effects. In contrast, the deposition of droplets of U90 and glycerol-based liquids do not induce a Marangoni flow.

Now we analyze the data for PEG-ran-PPG-based liquids again in the light of their surface-active properties. Back at the scale of the droplet (Fig. 7.3), we see that PEG-*ran*-PPG-ME70 and PEG-*ran*-PPG overlap in the ($\mathrm{Bo}_\alpha - \mathbf{R}\mathrm{Ca}$) space, even with data for pure glycerol, G100, suggesting that surfactants play no role at this scale. The story is different if we focus on the contact line.

Figure 8.6 focuses on the comparison between prediction 2.50 of the nonlinear theory and experimental data for PEG-*ran*-PPG and PEG-*ran*-PPG-ME70 . We see that the nonlinear theory overestimates the advancing branch as Ca increases: the drop goes faster than expected by the model at fixed θ_d. We propose the following mechanism to explain our data, sketched in Fig. 8.7. Given the geometry of our problem, the surface concentration of surfactants at the front of the drop may differ from that at the back. In particular, surfactants may accumulate at the trailing edge, leading to a smaller surface tension there than at the front. This difference of surface tension along the droplet contour can induce a stress and a flow from the back to the front the droplet, adding a source of energy to the system that our model does not account for; droplets should then move faster than what the model predicts, as we observe here. We think that this interpretation is consistent with the sharpening of

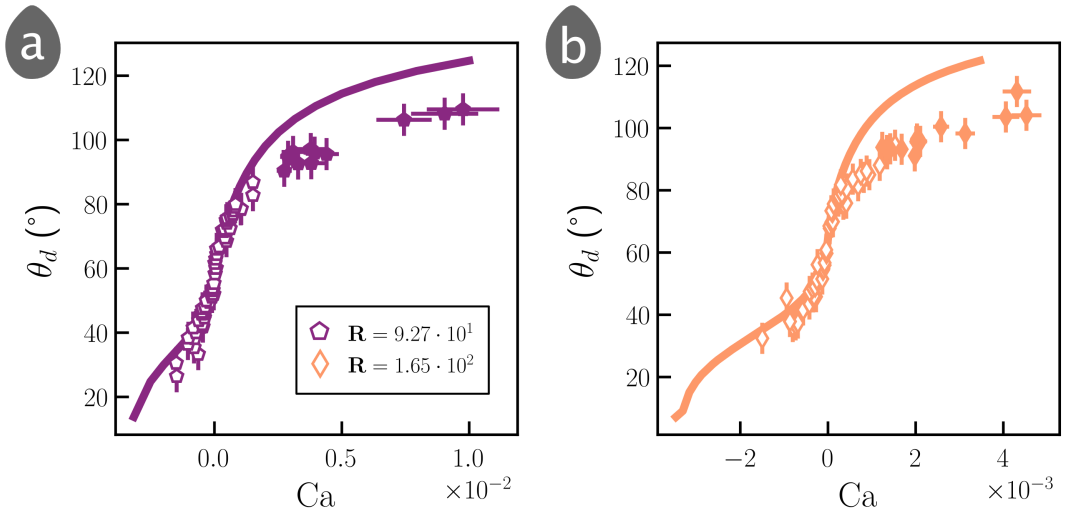

Figure 8.6: **The model overestimates the advancing branches of PEG-*ran*-PPG-ME70 and PEG-*ran*-PPG .** $\theta_d = f(\mathrm{Ca})$ curves for (a) PEG-*ran*-PPG-ME70 and (b) PEG-*ran*-PPG . Each time, the symbols and the solid line account for the experiments and the theoretical fit.

the droplet trailing edge, which indicates that the surfactants gather at the trailing edge to reduce the energetic cost of bending the droplet interface at small scales.

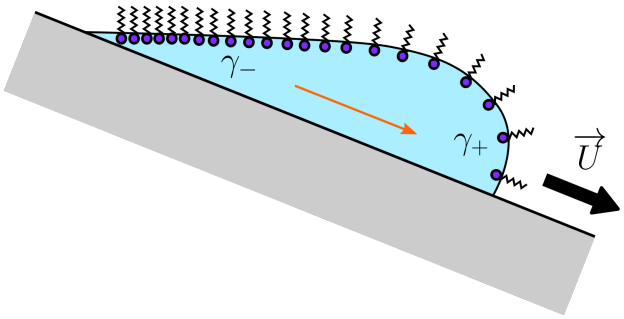

Figure 8.7: **The surface distribution of surfactants might accelerate a sliding drop.** A drop of an aqueous solution with surfactants slides onto an incline with a speed $\vec{U}$. A non heterogeneous surface distribution of surfactants at the free surface might induce a Marangoni flow. If the surfactants gather at the rear of the drop, the surface tension at the front γ_+ exceeds that at the rear γ_-. The resulting Marangoni flow accelerates the drop (orange arrow).

8.3 Droplet scale dynamics

8.3.1 Back to the $\mathrm{Bo}_\alpha - \mathrm{Ca}$ space

We can use the good agreement between Eq. 8.4 and the data to analyze dynamics at the scale of the droplet in the $\mathrm{Bo}_\alpha - \mathrm{Ca}$ parameter space. To do so, we need to relate Bo_α to contact angles so that we can convert gravitational potential energy into capillary energy. We do so by assuming that:

$$\rho g R_0^3 \sin(\alpha) \propto R_c \gamma (\cos(\theta_{d,a}) - \cos(\theta_{d,r})). \tag{8.5}$$

where $\theta_{d,a}$ and $\theta_{d,r}$ are the dynamic contact angles at the front and the back of the droplet respectively. Rearranging, we obtain:

$$\mathrm{Bo}_\alpha = b(\cos(\theta_{d,a}) - \cos(\theta_{d,r})). \tag{8.6}$$

where b is an appropriate proportionality coefficient. Now, using Eq. 8.4, we can compute the value of $(\cos(\theta_{d,a}) - \cos(\theta_{d,r}))$ for each value of Ca that we have investigated. We can then determine coefficient b from a fit of these theoretical datasets to the experimental ones. We find that the fits capture the datasets best when $b = 2.0 \pm 0.4$ (Fig. 8.8).

8.3.2 Threshold to pearling: prediction for the critical capillary number

In the literature, the pearling instability is assumed to develop when the receding contact angle vanishes. The non-linear model is able to predict the value of the capillary number at which this should occur. Dashed horizontal lines in Fig. 8.8 represent the absolute value of this critical capillary number $|\mathrm{Ca_u}|$ ($\mathrm{Ca_u} < 0$ since the contact line recedes). We obtain a good agreement between data and theory. The critical capillary number is underestimated at $\mathbf{R} = 119$: this mismatch is likely due to the fact that the model has issues capturing the receding branch of the $\theta_d - \mathrm{Ca}$ curve. In contrast, the model overestimates $|\mathrm{Ca_u}|$ at $\mathbf{R} = 165$. We also note that the model seems able to predict the steepening of the slope at the largest values of Bo_α when $\mathbf{R} \sim 10^4$. The prediction suggests that the actual value of $|\mathrm{Ca_u}|$ should be chosen close to those of the unstable points. It supports the idea that we overestimate the value of θ_u reported for G60: we measure it too far from the actual instability threshold.

Figure 8.9 compares experimental values of $|\mathrm{Ca_u}|$ with predicted thresholds as a function of $\mathbf{R}$. Each color on the graph represents a set of points for which the equilibrium contact angle is identical. The model is in good agreement with the experiments: the critical capillary number $|\mathrm{Ca_u}|$ decreases with increasing $\mathbf{R}$ at fixed θ_{eq}, and also decreases with decreasing θ_{eq} at fixed $\mathbf{R}$. The predictions provide also a good order of magnitude of the instability thresholds.

In a similar fashion to the rigid case [71, 77, 78], we are left with the puzzling observation that, while the model seems able to predict $|\mathrm{Ca_u}|$, the assumption made to select its value in the model is actually not verified in experiments: the receding dynamic contact angle is still finite, of the order of 30 to 60 °. In fact, the good predicition of $|\mathrm{Ca_u}|$ comes from the fact that the receding branch of our nonlinear theory approaches $\theta_{d,r} = 0$ vertically: θ_d varies by a significant amount while Ca hardly does.

Thus, we conclude that the model gives a good order of magnitude of the instability threshold despite a crude assumption (vanishing receding angle close to instability) and constrained fits (an identical fit parameter for all systems).

8.4 Force balance at the ridge tip

Our data also allow us to test a prediction for the force balance at the tip of the ridge, Eq. 2.46, that is assumed to be adaptable to an arbitrary equilibrium contact angle θ_{eq} in ref. [62]:

$$\frac{\gamma_s}{\gamma}\left(\frac{\cos\theta_{eq} - \cos\theta_d}{\sin^2\theta_d}\right) = \mathscr{F}_{\mathrm{cap}}(\mathbf{R}\mathrm{Ca}, \Lambda) + \mathscr{F}_{\mathrm{ve}}(\mathbf{R}\mathrm{Ca}, \Lambda). \tag{8.7}$$

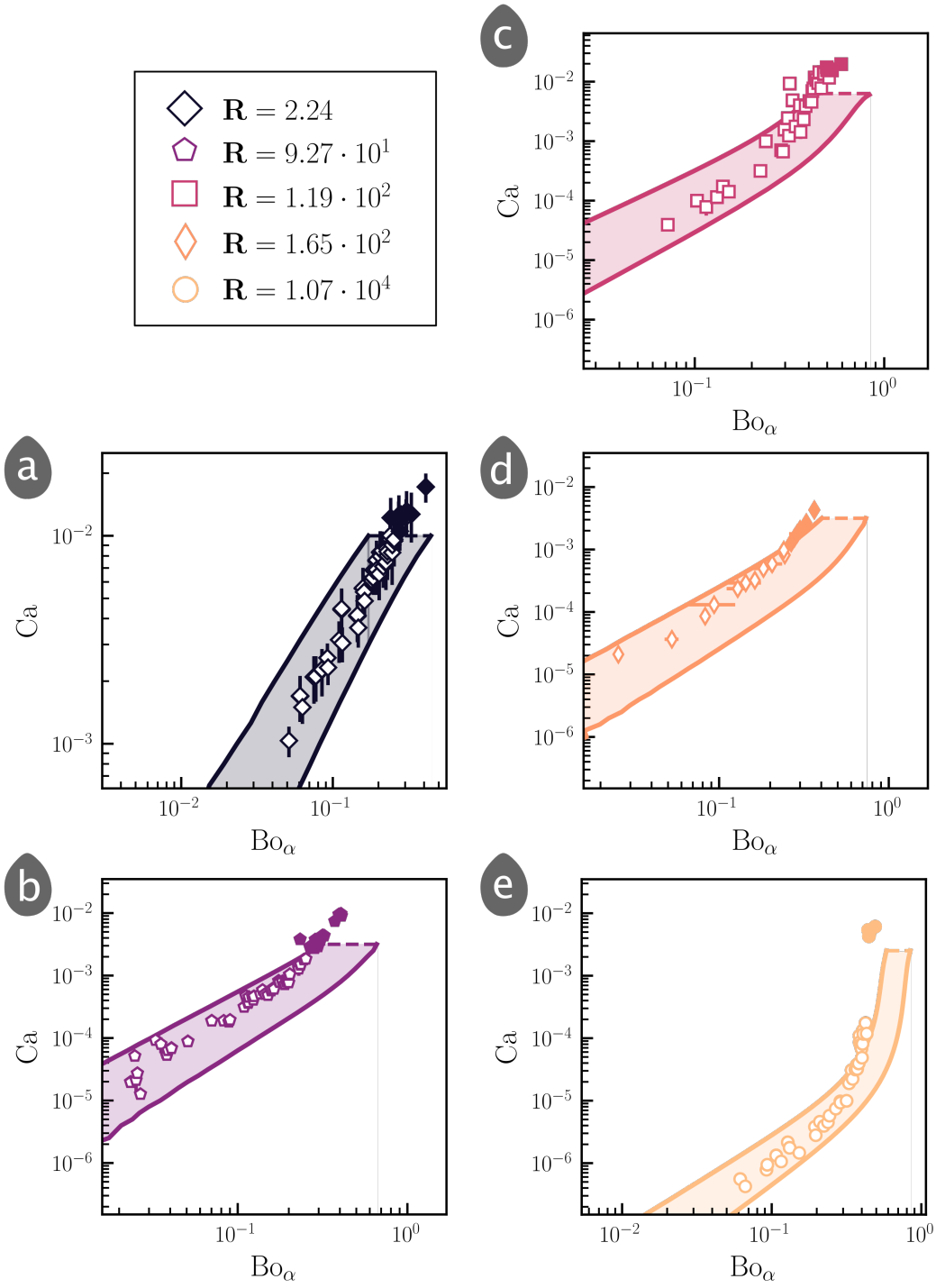

Figure 8.8: **Theory versus experiments: $\mathrm{Bo}_\alpha = f(\mathrm{Ca})$ curves.** Each time, the points are experimental data and the solid lines are fits of the nonlinear theory [62]. There are two fitting parameters with identical values for all systems: $x/x_{\min} = 1000$, and the proportionality coefficient $b = 2.0 \pm 0.4$ between the weight and the capillary driving force. Colored area: confidence interval of the fits (colored patches); dashed lines: prediction of the pearling transition. (a) {SYLGARD™ 527 ; U90}; (b) {SYLGARD™ 527 ; PEG-*ran*-PPG-ME70 }; (c) {SYLGARD™ 527 ; G100}; (d) {SYLGARD™ 527 ; PEG-*ran*-PPG }; (e) {SYLGARD™ 527 ; G60}.

We compare our dynamic contact angle measurements to solution 8.7 in Fig. 8.10. The black solid line represents the analytical calculation of $\mathscr{F}_{\mathrm{cap}}(\mathbf{R}\mathrm{Ca}, \Lambda) + \mathscr{F}_{\mathrm{ve}}(\mathbf{R}\mathrm{Ca}, \Lambda)$, and the

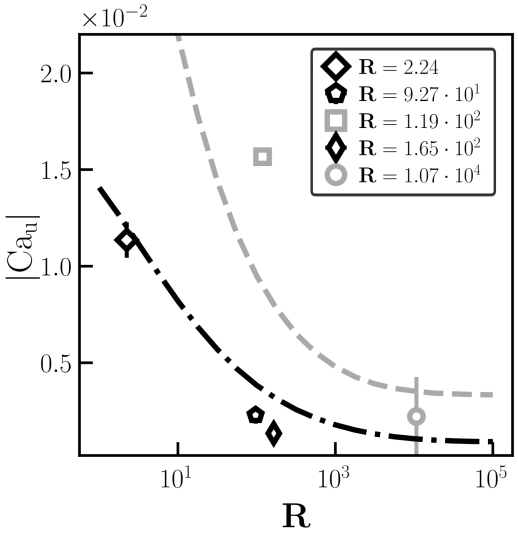

Figure 8.9: **Theoretical instability threshold.** The critical capillary number $|Ca_u|$ decreases with **R** at $\theta_{eq} = 98°$(gray dashed line, G100 and G60) and $\theta_{eq} = 62°$ (black dash-dotted line, *PEGs* and U90). The model predicts similar trends to the experimental data.

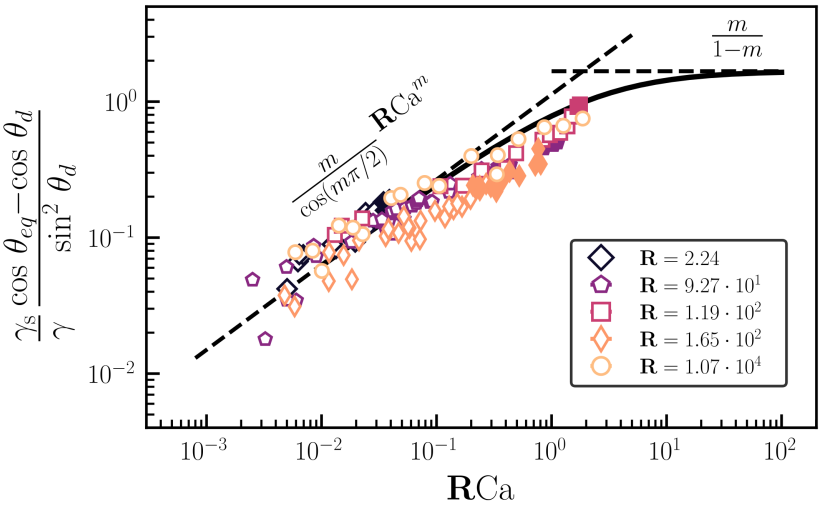

Figure 8.10: **Summed contributions of the viscoelastic and capillary restoring forces to the contact angle selection.** The analytical expression has two asymptotes, a power law with exponent m at low values of **R**Ca and a plateau.

dashed lines represent its two asymptotes [62]:

$$\frac{\gamma_s}{\gamma}\left(\frac{\cos\theta_{eq}-\cos\theta_d}{\sin^2\theta_d}\right)=\frac{m}{\cos(m\pi/2)}\mathbf{R}\mathrm{Ca}^m, \qquad \mathbf{R}\mathrm{Ca}\to 0 \tag{8.8}$$

$$\frac{\gamma_s}{\gamma}\left(\frac{\cos\theta_{eq}-\cos\theta_d}{\sin^2\theta_d}\right)=\frac{m}{1-m}, \qquad \mathbf{R}\mathrm{Ca}\to\infty \tag{8.9}$$

We see that the model is in very good agreement with the data. The asymptote for **R**Ca → 0 collects the experimental points sitting below **R**Ca = 10^{-1}. Beyond the latter limit, data depart from Eq. 8.8, still following the analytical prediction toward the plateau for **R**Ca → ∞, a regime where ridge rotation due to viscous delay is expected to play a significant role in

setting the force balance at the ridge apex. Our experiments stop at $\mathbf{R}\mathrm{Ca} \sim 1$, *i.e.* close to the solid capillary number $\mathbf{R}\mathrm{Ca}^*$ at which the $\mathbf{R}\mathrm{Ca} \to 0$ and high $\mathbf{R}\mathrm{Ca} \to \infty$ asymptotes intersect:

$$\mathbf{R}\mathrm{Ca}^* = \left(\frac{\cos(m\pi/2)}{1-m}\right)^{\frac{1}{m}} \sim 1.9 \tag{8.10}$$

These observations shed light on the failure of the Cox-Voinov relation to predict the microscopic length for U90. Equation 8.7 does not account for viscous dissipation in the liquid and still captures well this dataset. This agreement supports our previous claim that, despite similarities in droplet shapes and the $\mathrm{Bo}_\alpha - \mathrm{Ca}$ curves with the rigid case, the physics of U90 running droplets on our elastomer still involves dissipation in the solid. From Fig. 8.10, and considering all datasets, we are even led to conclude that our measurements are mostly sensitive to capillary and viscoelastic restoring forces at the scale of our measurements (~ 100 µm $\sim 10 l_s$), neglecting viscous dissipation.

8.5 Consequences of the general agreement between model and data

The comparison between experimental data and the non-linear model of ref. [62] shows that theory is able to describe experiments very well overall. In particular, the role of the dissipation ratio **R** as a good guide to predict whether dissipation in the solid or in the liquid will dictate the shapes and dynamics of running droplets is now well established. Care should be taken however when thinking about the dynamics at the scale of the contact line as dissipation in the solid is still at play even when droplets tend to indicate that their dynamics are dominated by viscous dissipation in the liquid. We wish to discuss here some aspects of our results that we think open interesting questions to conclude this chapter.

One of the most intriguing results comes from the discussion of Eq. 8.4. For all the systems that we have used, the value of the ratio x/x_{min} used in the fits is 1000. As we have already pointed out, we find then that $x_{\mathrm{min}} = 100$ nm, a scale that is independent of the used liquid phase (and hence of **R**) and still smaller than the elastocapillary length l_s, the scale below which dissipation in the solid occurs. These observations open the question of the origin of this length scale, and whether it influences other aspects of the droplet, such as its shape or the size of pearls.

Another interesting result is related to the puzzle around the pearling transition. The model is able to predict the threshold for the instability rather well. However, the assumption of a vanishing receding contact angle for liquid deposition to occur is not met in experiments, in the same fashion as in the case of a rigid substrate. In the latter situation, this disagreement was related to the presence of surface defects. This hypothesis is unlikely to be true here. Indeed, we observe little to no hysteresis when measuring contact angles around sliding droplets, in particular in the case $\mathbf{R} \sim 2$. Besides, our gels contain a significant amount of free chains, and we think that these chains occupy the surface of the gel as well. As a consequence, the surface should be defect-free. Thus, we feel that the conditions under which liquid deposition occur remain mysterious.

Along similar lines, we have seen that the trailing edge of droplets can have an oscillatory motion as the threshold to liquid deposition is approached. Again, the model says nothing about this. The reasons behind these oscillations are unclear. One possibility is that the receding contact line cannot bend and form a corner as easily on these soft substrates as it does on rigid ones. The reason behind this remains to be identified though.

The success of Eq. 8.7 at describing data up to prefactors also suggests that the force balance that it is based on contains the appropriate physics. The predicition for the value of the plateau remains to be checked systematically. The data suggest that these experiments should be performed at large values of **R**. The only other set of data that reports a similar trend is that of ref. [83]. While we reach a maximum value **R**Ca ~ 2, their data reaches slightly a slightly higher value, around 5. Figure 8.10 shows that the plateau value is expected to be reached at much higher values of **R**Ca.

Finally, the model that we use does not resort to the hypothesis of a strain-dependent surface tension for the solid. Extending the elastic part of the model to finite strains and geometric non-linearities seems to be sufficient to describe the data. While this result does not close the debate on the existence of the strain dependence of surface tension for a gel, it shows that the assumption is not necessary to describe our data with good accuracy.

Chapter 9

Perspectives: receding contact lines on soft substrates

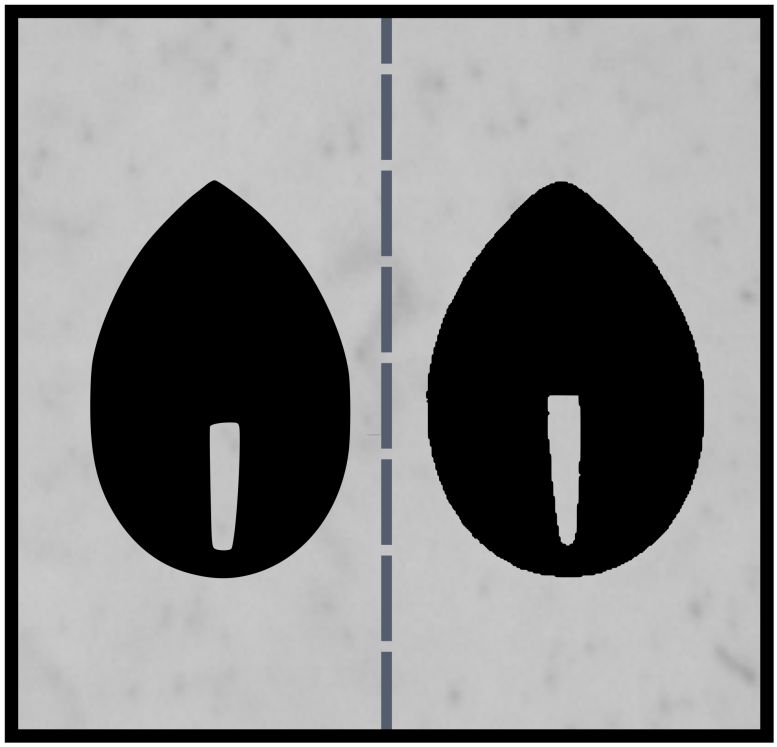

We have pointed out in Chap. 6 how the shape of droplets sliding on a silicone gel in conditions where energy dissipation occurs mostly in the solid has little to do with those described in the case of a rigid substrate, when dissipation in the liquid dominates [97, 98]. In particular, the droplet trailing edge remains rounded even close to the threshold of the pearling instability. We have started investigating the possible origin of these observations. While this work is still very much in progress, we have results that we want to discuss here. We also comment on the directions these results point us to.

9.1 Trailing edge curvature: dependence on R and l_s

Corners at the trailing edge of sliding droplets were first reported by *Podgorski & al.* [97]. Two features of the corner attracted the attention of scientists, its opening angle ϕ and its curvature R_{curv}. The theoretical description of these quantities is a subtle matter: the corner region is characterized by a strong curvature of the contact line, and the description of the flow must be three-dimensional. In the rigid case, the critical capillary number associated with the transition to liquid deposition is dependent on the curvature of the contact line [100]: the corner appears as a way for the droplet to avoid this transition. Predictions have been proposed for both ϕ and R_{curv} that capture the experimental data well [98, 100]. The latter is of particular interest to us, as we can easily measure it on our images and discuss its relation to characteristic length scales such as estimated molecular scales of our liquids and the elastocapillary length l_s of the silicon gel.

Peters & al. proposed the following law to fit the radius of curvature R_{curv} of the trailing edge of the droplet as a function of its velocity [98]:

$$R_{curv} \sim \ell \exp\left(\frac{\theta_{s,r}^3}{Ca}\right), \tag{9.1}$$

with ℓ the microscopic cut-off length scale appearing in the Cox-Voinov relation and $\theta_{s,r}$ the receding contact angle limit of the hysteresis. Comparison with experiments showed that Eq. 9.1 was a good fit to the data (reproduced in Fig. 3.4c).

We take inspiration from *Peters & al.'s* work and we measure the radius of curvature R_{curv} of the trailing edge of our droplets. Then we plot the ratio R_c/R_{curv}, with R_c the radius of the contact area of the droplet at rest, as a function of the non-dimensionalized velocities Ca and **R**Ca (Fig. 9.1). We approximate the drop as a spherical cap of contact angle θ_{eq} to calculate the contact radius R_c. In the rigid case, the ratio remains almost constant and of order 1 until the capillary number becomes comparable to the critical capillary number for liquid deposition, at which point the ratio increases rapidly by several orders of magnitude (Fig. 9.1a). The picture is more nuanced in the case of a soft substrate.

For $\mathbf{R} \sim 10^4$ we do not approach the transition to pearling close enough to observe a sudden rise of the curvature. Other datasets showing the instability have a qualitative resemblance to the rigid case, with the difference that the rise of R_c/R_{curv} is of smaller amplitude. Looking at the data as a function of **R**, we see that the maximum possible curvature increases with decreasing dissipation ratio. The radius of curvature at the rear of the drop reaches at most one-eighth of its static contact radius, for U90. This ratio decreases to one-third for G100 and stays below one-half for G60 (we do not deal with the PEG-ran-PPG fluids here). Drops sliding onto rigid substrates exhibit much larger curvatures. Viscoelastic substrates seem to prevent sharp curvatures. Note that errorbars become larger for the very last points of {SYLGARD™ 527 ; U90} and {SYLGARD™ 527 ; G100} because the rear of the drop oscillates in those particular experiments.

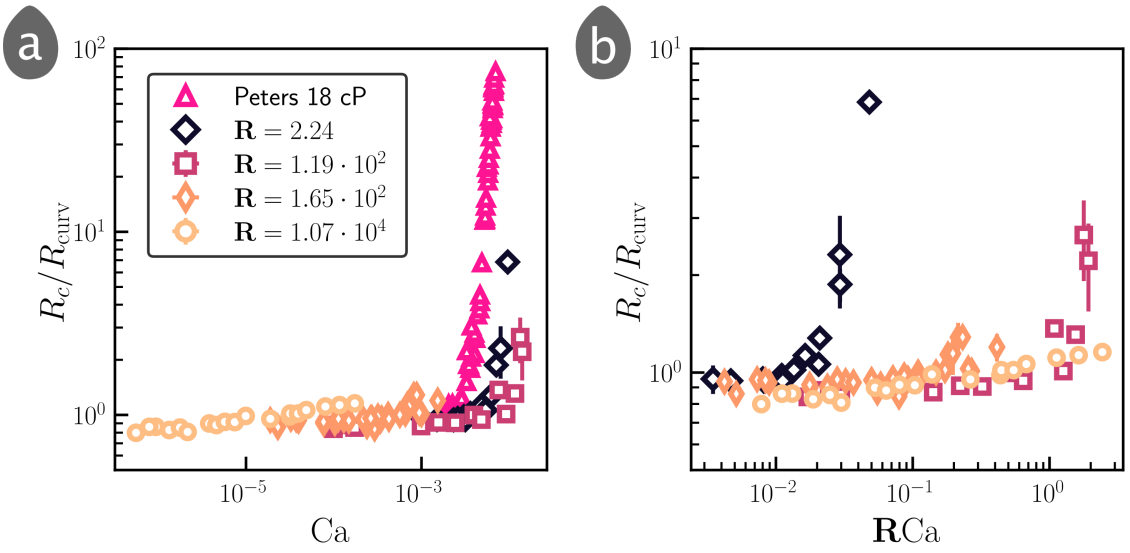

Figure 9.1: **Relation between the curvature at the rear of the drop and the running speed.** The curvature at the rear $1/R_{curv}$, normalized by the curvature $1/R_c$ of the same drop at equilibrium, as a function of the (a) capillary number Ca and (b) the solid capillary number **R**Ca. The gel is SYLGARD™ 527 . None of the configurations collapses our data.

In all of the cases described in Fig. 9.1a, datasets stop when the drop destabilizes and pearls are emitted. In other words, systems with a large dissipation ratio emit droplets before a corner can form and the radius of curvature remains of the order of the radius of the droplet at rest all along. Decreasing **R** leads to a decrease of the radius of curvature of the trailing edge of the droplet just before reaching the pearling transition.

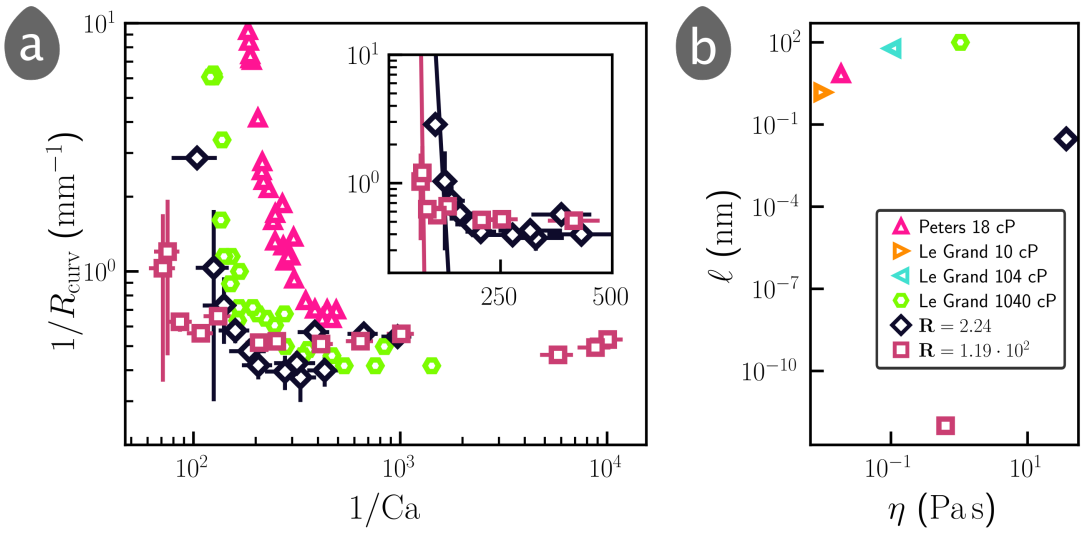

Figure 9.2: **Cornered drops on soft and rigid substrates.** The legend is the same for (a) and (b). For the sake of clarity, we only plot the data corresponding to η = 18 cP [98] and η = 1040 cP protect [71] in (a).(a) The curvature at the rear of the drop as a function of 1/Ca. Inset: Fit of Eq. 9.1 for the two elastowetting systems (solid lines). (b) Microscopic cutoff lengths ℓ as a function of the viscosity of the fluid.

To move a step further, we plot the data in the fashion suggested by *Peters & al.* We focus

on data obtained with G100 and U90, as their shape is the closest to that of the rigid case (Fig. 9.2a). We fit Eq. 9.1 to the datasets (inset in Fig. 9.2a), taking $\theta_{s,r} = \theta_{eq}$ as hysteresis is absent in our systems. We then extract the lower cutoff length ℓ. Figure 9.2b compares the obtained ℓ with those of refs. [71, 98]: the points of our systems are clearly off. Despite the resemblance between the datasets for U90 and those obtained by *Le Grand & al.*, the values for ℓ differ by orders of magnitude, giving the non-physical value $\ell = 3 \cdot 10^{-2}$ nm for U90. We draw the same conclusion as for the Cox-Voinov approach: the curves look alike but the model that describes wetting on rigid substrates gives a non-physical value for the microscopic scale for the elastowetting system. The disagreement is even worse for G100: its curve shifts to the left, and $\ell = 1 \cdot 10^{-12}$ nm! Hence, we should account for the viscoelastic substrate to work out the relation between the rear curvature and the running speed. We should also keep in mind that Eq. 9.1 has a strong dependence on the contact angle.

Further investigation should confirm the role of **R** in the relation between the speed and R_{curv}.

9.1.1 The elastocapillary length affects the size of the corners

Given the apparent failure of *Peters et al.'s* model at describing our datasets, we go back to experiments to see whether we can identify dependencies of the radius of curvature of the trailing edge of the droplet on parameters of the system that are irrelevant to the rigid case. The obvious candidate is the elastocapillary length, as it is a scale lying between the nanoscopic cutoff of the liquid and the size of the droplet, and it is the typical scale under which dissipation in the solid occurs.

To test this dependence, we conduct sliding experiments with a stiff silicon gel, SYLGARD™ 184 . The rheology of this gel [43] fitted with the Chasset-Thirion indicates that the shear modulus is $\mu_0 = 520$ kPa, $\tau = 120\,\mu$s and $m = 0.251$. With these parameters and the same surface tension as that of SYLGARD™ 527 , we obtain $l_s \sim 30$ nm, three orders of magnitude smaller than l_s for SYLGARD™ 527 . At the same time, values for **R** remain in the same realm, by a factor of 4-5, because the variation of τ compensates that of μ_0; we obtain systems with comparable **R** but different l_s.

The shape diagram 9.3 compares top views obtained on the two silicon gels, with G100 and U90. Images are grouped by values of **R**. We see that the shapes obtained at similar values of Bo_α for comparable **R** are similar. We find again the transition to cornered drops that elongate and destabilize forming small pearls at low values of **R**. Shapes obtained at **R** of the order of a few hundred show paralell sides at intermediate values of Bo_α.

As usual in this problem, the devil lies in the details. Careful analysis shows that the corner is sharper in the case of stiff PDMS than for the soft one (Fig. 9.4a). For both gels, we measure the typical radius of curvature at the trailing edge of the drop R_{curv} when the drop is slightly below the instability threshold. The curvature is three times bigger when l_s increases by three orders of magnitude (Fig. 9.4b). Note that the curvatures measured on SYLGARD™ 184 reach our limit of resolution. We need magnified photographs to better quantify it.

Likewise, the elastocapillary length l_s sets the pearl pattern above the instability threshold (last pictures in the two upper columns of Fig. 9.3). Figure 9.5a displays two drops just above the instability threshold for {SYLGARD™ 527 ; U90} and {SYLGARD™ 184 ; U90}. The spacing between pearls increases with an increase of l_s. Figure 9.5b reports a similar increase in the size of the pearls: they are four times larger when l_s increases by three orders of magnitude.

To sum up, our observations suggest that the sharpness of corners is in part controlled

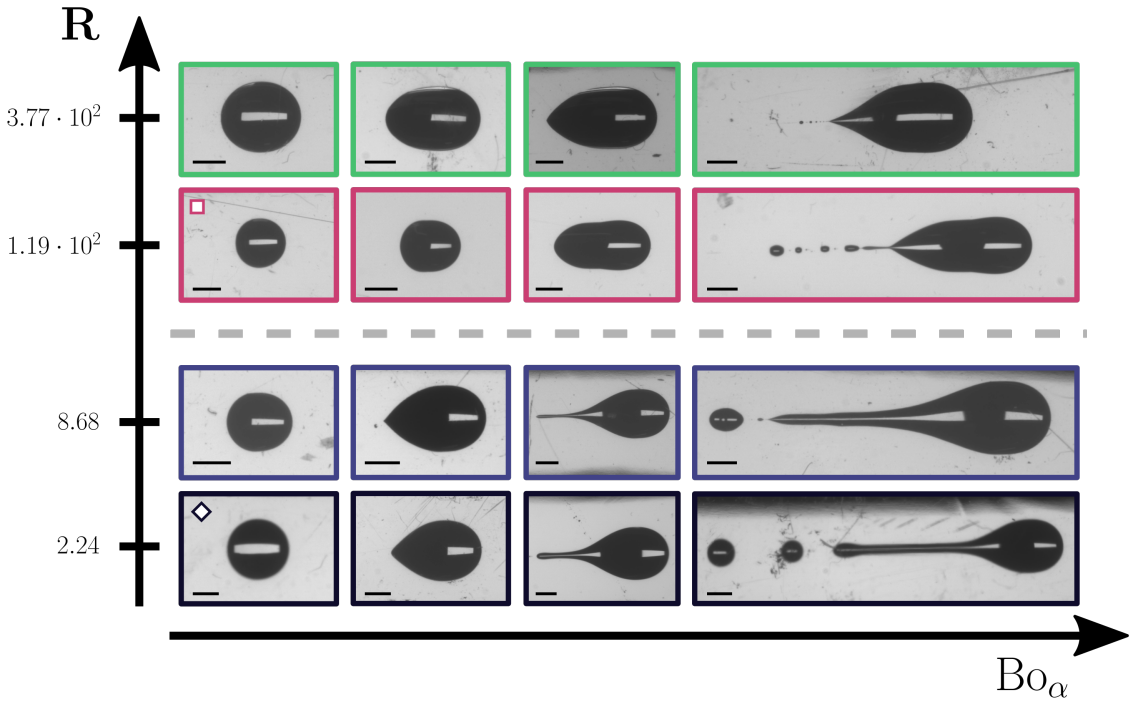

Figure 9.3: **Changing the silicone gel impacts the shape of the drops at comparable values of R.** Shape diagram obtained at comparable values of **R** on both SYLGARD™ 527 and SYLGARD™ 184 . Scale bar: 2 mm.

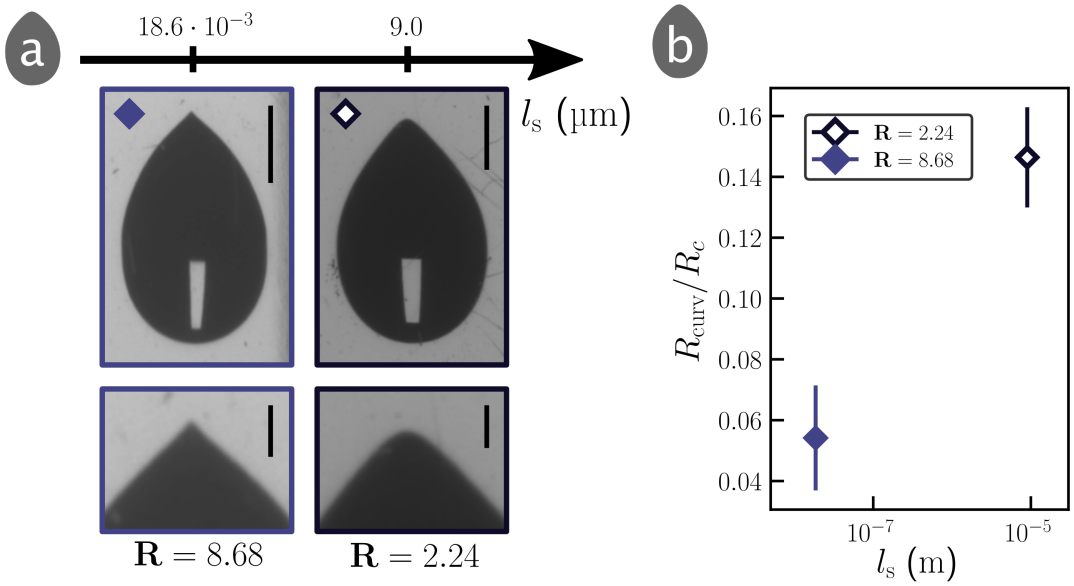

Figure 9.4: **Corners sharpen with decreasing l_s at fixed R.** (a) Top views of a U90 drop sliding onto SYLGARD™ 184 (left) and SYLGARD™ 527 (right). The bottom pictures magnify the corners of the top pictures. Scale bar: 2 mm for top images, 500 µm for images. Left: **R** = 8.68; l_s = 18.6 nm; Bo_α = 0.146. Right: **R** = 2.24; l_s = 9.0 µm; Bo_α = 0.239. (b) Radius of curvature at the rear of the drop R_{curv} as a function of l_s. The contact radius is identical in both cases and we use it to normalize R_{curv}. R_{curv} = 349 ± 39 µm when l_s = 9.0 µm, R_{curv} = 107 ± 34 µm when l_s = 18.6 nm.

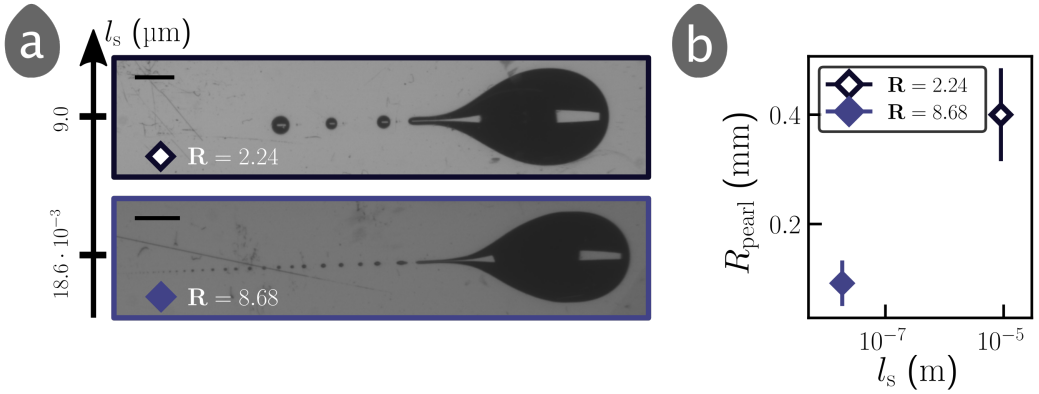

Figure 9.5: **Effect of l_s on pearl patterns at fixed R.** (a) Top views of a U90 drop sliding on a silicon gel just above the instability threshold. Top: SYLGARD™ 527 , **R** = 2.24; l_s = 9.0 µm; Bo_α = 0.272. Bottom: SYLGARD™ 184 , **R** = 8.68; l_s = 18.6 nm; Bo_α = 0.160. Scale bar: 2 mm. (b) Pear radius as a function of l_s. We averaged our measurement over several drops (the three biggest drops in the top picture, the fourteen first drops (that already relaxed) in the bottom picture), the standard deviation gives the error bar.

by the elastocapillary length l_s. The existence of the corner itself seems to depend also on the value of **R**: droplets sliding at large **R** switch from a rounded trailing edge to the pearling instability without showing a corner. The latter claim remains to be thoroughly tested with the stiff substrate. These observations pave the way for further research to understand what sets the sharpness of cornered interfaces.

9.2 A broader look at wetting on a stiff gel

Experiments on SYLGARD™ 184 hold promise in discriminating the link between the dynamics of receding contact lines and the properties of both the solid and the liquid. However, we stumbled on issues that have yet to be solved if we want to carry out an extensive study of wetting on SYLGARD™ 184 .

A systematic study of droplet sliding shows that care must be taken to reach reproducibility. This issue is particularly obvious if we analyze droplet trajectories.

Even though we take great care in setting up our systems, the first trajectories that we obtain with SYLGARD™ 184 are puzzling (Fig. 9.6). Figure 9.6a displays two trajectories that we observed for a droplet of U90. The dynamics of both drops are characterized by a slow down during the whole duration of the experiment. Moreover, the velocities are very different. These effects are reminiscent of those that we observe if we leave SYLGARD™ 527 samples exposed to light during long sliding experiments. However, the issue here is that the polystyrene lid that is known to prevent ageing of the surface in the case of SYLGARD™ 527 is in place too, and the droplet still has dynamics characterized by a time-dependent velocity. Finally, the shape of the droplet also evolves over time, and the radius of curvature of the trailing edge decreases as the droplet slows down, a rather surprising result.

The trajectory of another liquid, a droplet of G100, has a shape reminiscent of those reported by *Hourlier-Fargette et al.* [92, 126, 132]. The droplet slides at a low pace before accelerating and sliding at a much higher velocity (Fig. 9.6b). This type of trajectory was related to contamination of the droplet/air interface by free chains present in the gel. The difference with SYLGARD™ 527 is that the amount of free chains in SYLGARD™ 184 is 5 wt%. Hence surface contamination can take some time. These dynamics are also akin to those attributed

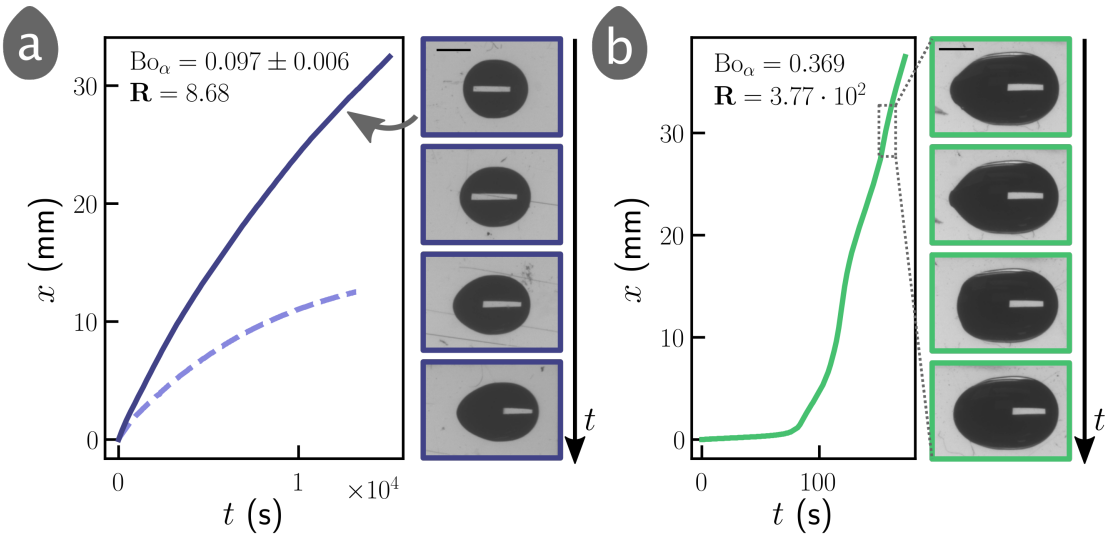

Figure 9.6: **Puzzling trajectories on SYLGARD™ 184 .** (a) Trajectories of two similar experiments. The system is {SYLGARD™ 184 ; U90}. The grey arrow points towards the trajectory for which we display top views of the droplet. The radius of curvature at the rear of the drop evolves all along the experiment. Scale bar: 2 mm. (b) Trajectory of the front of an oscillating drop. The system is {SYLGARD™ 184 ; G100}. We retrieve two speed regimes, just like [92, 126, 132]. The right panel displays top views of the droplets as the rear moves back towards the drop. Total time for the images: 6 s. Scale bar: 2 mm.

to adaptive wetting [141]. Moreover, the drop oscillates during the high-velocity regime: its leading and trailing edges oscillate in phase. The right panel displays a short moment of the trajectory, when the trailing part of the drop snaps back towards the drop. To our surprise, the back of the droplet becomes almost flat, in fashion similar to that of a bubble rising in a viscoelastic fluid [142]. Closer analysis seems also to indicate that a wave propagates along the back of the droplet and focuses at its tip.

As a conclusion, much work remains to be done to control the systems involving SYLGARD™ 184 . The issue here is to identify the set of properties of the gel that, once under control, ensure experimental reproducibility. SYLGARD™ 184 is a commercial kit, the formulation of which is known only partially. For example, besides PDMS, the material contains silica fillers that help increasing the elastic modulus. Moreover, the low amount of free chains may be an issue. Thus, the solution may be multiple: either add more free chains to the material so that droplet contamination is fast and hope that it will also screen possible interactions with the fillers and other material, or use a home-made gel, designed from carefully chosen base products.

9.3 Dip-coating of a soft surface

Another example of set-up allowing the study of contact lines, be they advancing or receding, relies on the motion of a plate in or out of a bath of liquid (Fig. 9.7). This configuration is usually known as dip-coating. From a fundamental point of view, this system has mostly been studied in two situations. In the first one, the liquid in the bath is in a state of complete wetting on the solid. In this case, the thickness h of the liquid film deposited on the moving plate depends on the velocity at which the latter is extracted from the bath, and it is described

theoretically by the Landau-Levich-Derjaguin (LLD) law [143]:

$$h \propto \ell_c Ca^{2/3} \tag{9.2}$$

where $\ell_c = \sqrt{\gamma/(\rho g)}$ is the capillary length.

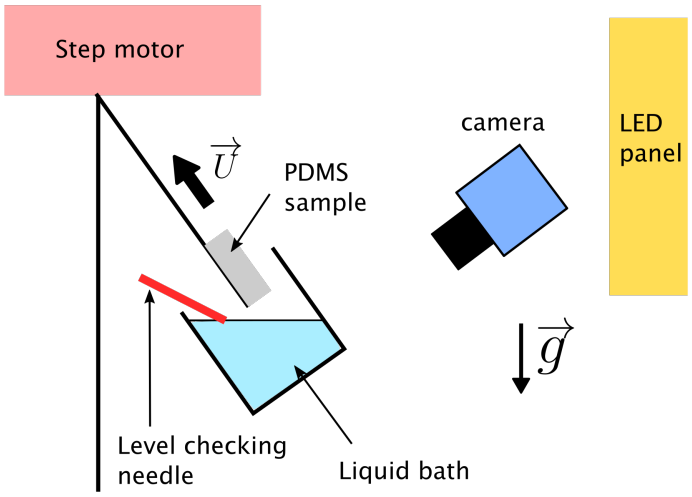

Figure 9.7: **An example of a dip-coating set-up similar to the one we used to run our experiments.** We remove a sample from a liquid bath. The liquid tank is inclined to improve visualization.

The other situation where the liquid only partially wets the substrate is relevant to us. In this situation, a liquid film is entrained only beyond a threshold velocity [78, 101, 144]. Not only is there a threshold for liquid entrainment, the shape of the film differs substantially from that of the LLD film (Fig. 9.8). The region of the contact line is separated from a LLD-like film by a much thicker front. Moreover, the contact line recedes from the edges of the substrate toward its center, taking a trapezoidal shape that ends forming a corner reminiscent of those observed behind running droplets.

I co-supervised an intern in Spring 2021, Lisa Kaufman, with whom we have started investigating receding contact lines on SYLGARD™ 527 in the context of dip-coating. In this part, I will give a first look at our preliminary results, and describe the next steps we will take soon.

The set-up we use is described in Fig. 9.7. Setting up this system for soft materials requires some care, in particular when handling gel samples. First, we have prevented ageing effects by enclosing the whole set-up in a box. Second, our PDMS samples are soft enough to sag under their own weight. We have solved this issue by adding a rigid and moveable piece of plastic at the bottom of the vessel we use to prepare the sample. We cut out the sample from the vessel and make sure to handle it *via* the plastic piece to limit stretch effects.

Once these steps are respected, experiments become reproducible. We test two fluids, G100 and U90. First, we find for all systems that there is indeed a threshold velocity beyond which a liquid film is entrained. Figure 9.9 depicts an example of entrainment. The contact line moves with the plate. We see that the top of the entrained film starts to recede early in the experiment, taking a shape similar to the trapeze observed in the rigid case. The vertices of the receding film take a slender shape and leave pearls behind them; to the best of our

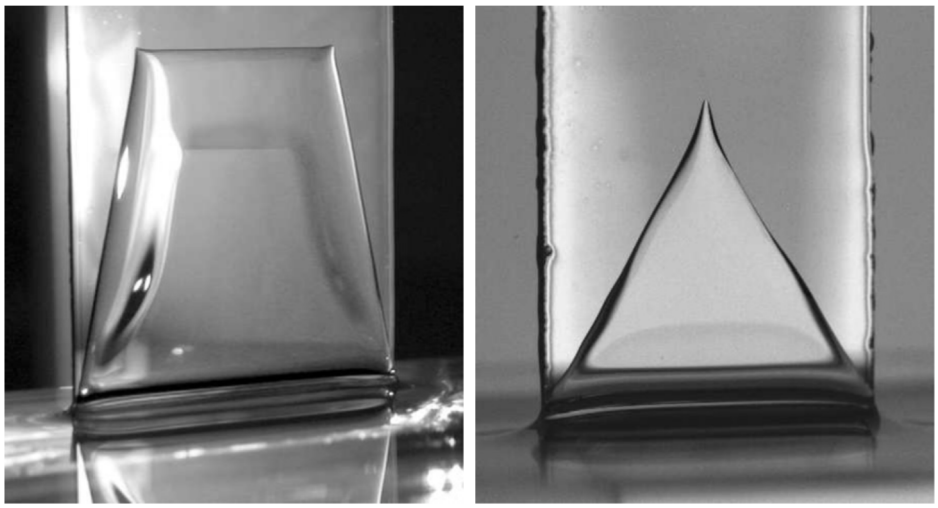

Figure 9.8: **Examples of films entrained in a dip-coating experiment where the liquid is in partial wetting on the solid.** A trapezoidal shape [144] (right) recedes and eventually forms a corner [78] (left).

knowledge, this instability of the vertices has not been reported in the case of the rigid substrate. The film goes on receding. In contrast to the rigid case, the corner is absent and the film ends up having a rectangular shape.

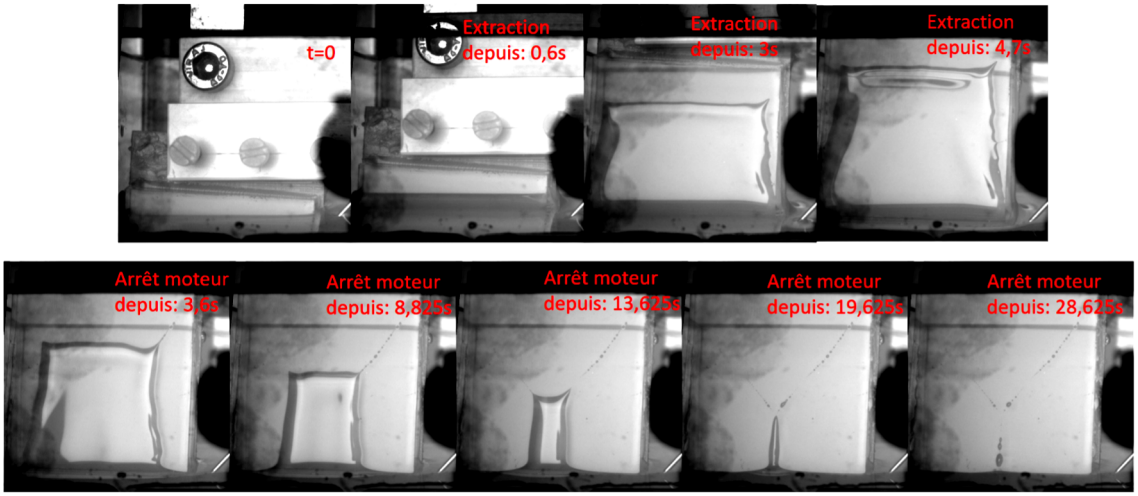

Figure 9.9: **Images of a film of G100 entrained by a moving plate of SYLGARD™ 527 .** As the trapeze recedes, its vertices become unstable. The film eventually takes a rectangular shape.

Increasing the viscosity of the liquid and switching to U90, the dynamics of the entrained film are slightly different. In particular, the receding film is rectangular straight away (Fig. 9.10). Again the vertices of the film form slender structures, and pearls are deposited.

Finally, our preliminary results suggest that the critical capillary numbers at which film entrainment occurs differ from the capillary numbers measured in the case of sliding droplets.

A lot of work remains to be done to characterize this system. First, the configuration that we use here does not provide access to contact angles at the contact line yet. This measurement will be useful to investigate what is the value of the angle at entrainement. Second, we would also benefit from a possibility to measure the thickness profile of the film. The needle depicted in Fig. 9.7 is supposed to be used as a proxy to this quantity, by tracking how its

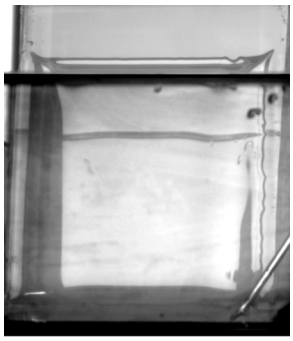

Figure 9.10: **A Rectangular receding film of U90 on SYLGARD™ 527 .**

reflection on the film is distorted by the height profile. Finally, we have hardly investigated the case $\mathbf{R} \sim 10^4$ and, once under control, running these experiments with stiff gels will also shed new light on this system.

Chapter 10

General conclusion

The literature is rich with investigations of the dynamics of wetting on soft substrates. Early, the significant role of energy dissipation in the solid was pointed out. Besides, the idea that capillarity of the solid needs to be accounted for to describe the statics and the dynamics of wetting is now a well-established fact. The work describes in this manuscript broadens the reach of our knowledge on these systems hopefully. To the best of our knowledge, a discussion of the effect of dissipation partition between the solid and the liquid is absent in the literature, and the work that we have performed and described here is a first step on this path.

Experimental work in this manuscript relies on droplets sliding on soft surfaces. The choice of sliding droplets is motivated by the desire to test the predictions of a recent model of soft wetting that extends the framework of elasiticity used to describe the solid to finite deformations. The same model also leaves the surface tension of the solid independent of strains. One of the purposes of this work is to show how far the model goes into describing carefully acquired data, and to eventally reach its limits. To do so, we need to be able to measure the contact angles between the solid-liquid and liquid-vapor interfaces on the receding and advancing contact lines. Doing so is easy on sliding droplets, as the line contour of the droplet on the substrate switches from advancing motion to a receding one as we move from the leading to the trailing edge of the droplet. The shapes and the dynamics of sliding also provide information on dissipation in a direct way, and the system offers at least two levels of analysis, at the scale of the droplet and at the scale of the contact line.

The guiding parameter of this study is a non-dimensional number, $\mathbf{R}$, that quantifies the dissipation partition in the system. In the limit $\mathbf{R} \to 0$, soft systems should be similar to those where droplets slide on rigid non-deformable substrates; viscous dissipation in the liquid should dominate the dynamics. Our experiments, while unable to reach the $\mathbf{R} = 0$ limit, show that this analogy is qualitatively valid even when $\mathbf{R} \sim 1$. In particular, we find a relation between the energy injected in the system and the energy dissipated that is akin to that of the rigid system, and droplet shapes compare very well, even showing cornered drops and a pearling transition beyond a threshold capillary number. Substantial differences with the rigid case arise when $\mathbf{R} \gg 1$. Droplet shapes remain more rounded up to the pearling transition, and the energy balance is dominated by dissipation in the solid.

The analysis of the dynamics at the scale of the contact line shows that the analogy between the rigid case and the soft one at $\mathbf{R} \sim 1$ is really qualitative. The dissipation in the solid still plays a significant role, in particular as a model of the relation between the dynamic contact angle and the velocity of the droplet that accounts for dissipation in the liquid only provides dubious estimates for parameters of the liquids such as their molecular size. Over-

all analysis of the data shows that the model we want to test is able to describe the data very well, with no free fitting parameter. Our theoretical framework describes the elastic response of the material up to order 2 in the strains, and this seems to be a sufficient level of non-linearity to describe the data. On the course of our comparison, we have unveiled some aspects of our experiments that the model had a hard time to capture, in particular with respect to the receding branch. In all cases, these discrepancies result either from a property of the liquids that we took note of *a posteriori*, such as a soap-like response, or from an unexpected oscillatory motion of the contact line the origin of which remains to be identified.

We discuss the conditions under which sliding droplets leave tiny droplets in their wake. The gels we use have little to no hysteresis. Besides, they contain significant amounts of free chains that are expected to smooth the surface of the gels. However, we observe that the pearling transition occurs at a critical capillary number for which the contact angle at the trailing edge of the droplet does not vanish, in contrast with our expectations. The latter was also reported in the case of a rigid substrate, and reasonably attributed at the time to possible effects of surface roughness and defects. These assumptions are difficult to justify here. Hence, while the critical capillary number is well predicted by the model, the observation of a finite angle at the pearling transition remains a puzzle, and more work is required to hopefully understand it. Besides, the path to the pearling instability depends on the dissipation ratio $\mathbf{R}$. While corners appear on the contour of droplets at low values of $\mathbf{R}$, the trailing edge of the droplets remains rounded with a radius of curvature of the same order of magnitude as the radius of the droplet at rest. Hence, even the possibility for the corner to exist is dependent on dissipation partition.

The focus on the trailing edge of droplets leads us to investigate the dynamics of receding contact lines in more detail. We provide insights into this question based on work in progess. The first idea is to compare how the shape of the droplet depends on the stiffness of the substrate. The idea is to test how the properties of the contact line, such as its ability to form corners, depend on the intrinsic elastocapillary length of the solid. This quantity is a decreasing function of the shear modulus of the solid. Our preliminary experiments show that the radius of curvature of the corners at the trailing edge of the droplet, when they exist, decreases with a decrease of the elastocapillary length. These experiments are still far from controlled, and extensive work remains to be done to characterize thoroughly our observations.

In the same vein, we have also investigated the dynamics of receding contact lines when the soft surface is extracted from a bath. These dip-coating experiments show that two regimes exist separated by a threshold velocity. The contact line remains in the vicinity of the surface of the liquid as long as the extraction velocity is below the entrainment threshold. When the latter is overcome, a film is entrained. However, the motion of the contact line is not homogeneous. Parts of the contact line close to the edges of the sample starts to recede with respect to the substrate during extraction: their velocity in the frame of the laboratory is smaller than that of the sample. We observe shapes that differ from the case of the rigid substrate. While the film becomes trapezoidal at early stages of recession, a rectangle is observed in the late stages. This rectangle is actually the only shape observed in the $\mathbf{R} \sim 1$ case, a surprising result as this system is supposed to be the closest to the rigid one. Again, a lot of work remains to be done, and some aspects of the entrained film such as its thickness profile and contact angles at the contact line must be measured to gather more insights into this problem. Moreover, going back to the rigid case with the liquids we use in these experiments might prove informative too.

Besides these short-term perspectives, this work points to some interesting prospects

with possibly different systems. One of these perspectives relies on the use of liquid-infused surfaces (LIS). Droplets moving on these surfaces are known to be surrounded by a ridge, similar in shape to the elastocapillary ridge of our systems. The presence of the layer is known to make these systems similar to non-wetting devices. The liquid infused at the surface of the solid, usually in a network of microscopic pillars, can dissipate energy. Our model also makes prediction for the dynamics of contact lines on viscous liquids, and LIS systems offer a nice platform to investigate the predictions of our model. A particular point of interest would be to investigate whether droplets sliding on LIS also experience a pearling transition, and measure the properties of the contact line at threshold.

Another prospect would be to synthesize soft elastomers with little to no free chains in their network. While such materials may be obtainable by mixing commercial kits in proportions far from the manufacturer's recommendation, this process is time-consuming, as free chains have to be removed by solvent extraction, an operation that takes at least a couple of weeks. Recent advances in polymer synthesis suggest that the soft networks almost free of free chains can be obtained by cross-linking reactive branched PDMS. Although this prospect requires mastering polymer chemistry, we think that this would be an interesting direction to take, as it would help the community sort out the origin of various observations made over the years as a function of the presence of free chains.

Chapter 11

Résumé en Français

Conformément aux règles de l'EDPIF et de l'université, nous résumons les travaux de cette thèse en langue française.

11.1 Introduction

Lorsque l'on dépose une goutte sur une surface solide, la capillarité du liquide tire sur le substrat au niveau de la ligne de contact, c'est-à-dire à l'endroit où les phases liquide, solide et le milieu ambiant (l'air dans notre cas) se rencontrent. Si le substrat est suffisamment mou, elle peut le déformer : il en résulte une déformation en forme de crête. En pratique, les substrats dits mous sont composés de polymères, ce qui leur confère des propriétés viscoélastiques. Lorsque le liquide se déplace, la ligne de contact va entraîner la crête, ce qui va coûter de l'énergie au système. Il y a maintenant deux sources de dissipation d'énergie pour le système : la viscoélasticité du substrat et la viscosité du liquide. L'étude de l'étalement d'un liquide sur un solide s'appelle le mouillage. Le cas particulier d'un solide déformable s'appelle l'élastomouillage.

La littérature regorge d'études sur la dynamique du mouillage sur des substrats mous. Très tôt, le rôle significatif de la dissipation d'énergie dans le solide a été mis en évidence. En outre, l'idée que la capillarité du solide doit être prise en compte pour décrire la statique et la dynamique du mouillage est maintenant un fait bien établi. Le travail décrit dans ce manuscrit élargit la portée de nos connaissances sur ces systèmes. A notre connaissance, la littérature ne discute pas comment la répartition de la dissipation énergétique entre le solide et le liquide affecte le système, et le travail que nous avons réalisé est un premier pas sur cette voie.

Le travail expérimental dans ce manuscrit repose sur le dévalement de gouttes sur des surfaces déformables. Ce choix est motivé par le désir de tester les prédictions d'un modèle récent d'élastomouillage qui prend en compte la théorie de l'élasticité non-linéaire pour décrire le solide à des déformations finies. Ce même modèle laisse la tension superficielle du solide indépendante des déformations, une hypothèse encore en discussion dans la communauté. Il laisse entendre que le rapport des deux sources de dissipation est un paramètre crucial du système, et régit la dynamique d'une ligne de contact. L'un des objectifs de ce travail est de montrer jusqu'où va le modèle pour décrire des données soigneusement acquises, et d'en déterminer les limites. Pour ce faire, nous devons être en mesure de mesurer les angles de contact entre les interfaces solide-liquide et liquide-vapeur sur des lignes de contact qui s'éloignent et qui avancent. Il est facile de le faire sur des gouttes qui glissent, car le contour de la goutte sur le substrat passe d'un mouvement d'avancée à un mouvement de

recul lorsque l'on passe de l'avant à l'arrière de la goutte. Les formes et la dynamique des gouttes fournissent également des informations sur la dissipation de manière directe, et le système offre au moins deux niveaux d'analyse, à l'échelle de la goutte et à l'échelle de la ligne de contact.

Le paramètre clé de cette étude est un nombre sans dimensions,

$$\mathbf{R} = \frac{\gamma\tau}{\eta l_s}$$

qui quantifie la répartition de la dissipation dans le système. Ce dernier compare la vitesse de relaxation visqueuse du liquide ($U_l = \gamma/\eta$ où γ et η sont la tension de surface et la viscosité dynamique du liquide) avec celle du substrat ($U_s = l_s/\tau$ où l_s est la taille caractéristique de la crête et τ le temps caractéristique de relaxation des polymères au sein du matériau). Dans la limite $\mathbf{R} \longrightarrow 0$, la crête relaxe extrêmement vite par rapport au liquide ; la dissipation visqueuse dans le liquide devrait dominer la dynamique et les systèmes mous devraient être similaires à ceux où les gouttelettes glissent sur des substrats rigides indéformables. Inversement, la crête relaxe extrêmement lentement par rapport au liquide dans la limite $\mathbf{R} \gg 1$; la dissipation dans le solide devrait dominer le bilan énergétique.

11.2 Protocole

Nous préparons des gels de silicone (PDMS) à partir de kits commerciaux. Il suffit d'en mélanger les deux parties, l'une contenant la base de polymères, l'autre contenant l'agent réticulant, pour enclencher la réaction de réticulation. Nous enlevons les éventuelles bulles introduites lors du mélange qui pourraient altérer les propriétés mécaniques du gel en plaçant ce dernier sous vide. Enfin, nous le laissons cuire toute une nuit à 65°C. Nous fabriquons des échantillons suffisamment épais, c'est à dire de taille millimétrique, pour éviter que le fond du récipient n'affecte nos résultats. La réticulation de nos gels n'est pas optimale, et une certaine quantité de chaînes dites « libres » ou « liquides » n'est pas liée au réseau élastique du matériau. Ces dernières sont susceptibles de modifier la dynamique de la goutte : dès lors que nous déposons une goutte de liquide sur le gel, les chaînes libres migrent vers cette dernière et la recouvrent d'un film. Lorsque toute la goutte est recouverte de chaînes libres, elle accélère soudainement. Le gel que nous utilisons contient 60 % de chaînes libres lorsque nous suivons la recette du fabriquant. Ainsi, nous n'observons qu'un seul régime de vitesse lorsque que les gouttes dévalent le substrat car la contamination est instantanée.

Notre montage expérimental est constitué d'un plan incliné en aluminium sur lequel repose le récipient contenant la couche de silicone. Nous y fixons deux caméras : l'une enregistre une vue de dessus de la goutte en mouvement tandis que l'autre capture une vue latérale. Ainsi, nous pouvons suivre la dynamique et la forme des gouttes lorsqu'elles dévalent le gel de silicone. Nous pouvons également mesurer les angles de contact dynamiques à l'avant et à l'arrière de la goutte. Les caméras se déplacent avec la plaque lorsque nous changeons l'inclinaison α, ainsi le substrat reste dans le plan focal de la caméra surplombant le montage, et reste horizontal pour la caméra latérale. La température et l'humidité de la pièce variant d'un jour à l'autre, nous vérifions la viscosité du liquide deux fois par jour à l'aide d'un viscosimètre capillaire. Le PDMS à l'état liquide forme un ménisque sur les parois du moule, obstruant ainsi la visualisation latérale une fois cuit. Lorsque nous voulons enregistrer une vue de côté, nous démoulons le gel de son récipient et découpons les bords à l'aide d'une lame de rasoir avant de replacer le gel sur un substrat rigide.

Nous inclinons toutes les expériences immédiatement, afin d'éviter que la déformation à la ligne de contact ne croisse entre le moment où nous déposons la goutte sur le gel et celui où nous inclinons ce dernier. Chaque goutte glisse sur une surface vierge de toute expérience, et suffisamment loin des précédentes expériences de sorte que les déformations antérieures n'affectent pas les mesures. Par ailleurs, nous avons identifié que nos gels vieillissent lorsqu'il sont exposés à la lumière. Les futures expériences d'élastomouillage devraient prendre en compte cet effet, jusque là non reporté dans la littérature du domaine. Nous contournons ce problème en gardant le couvercle sur les récipients (ce dernier filtre les rayons UV émis par les néons de la salle) et réalisons nos expériences sur des gels vieux d'un jour.

Nous avons par ailleurs mesuré la rhéologie de nos matériaux pour en extraire un module de cisaillement μ_0, un temps caractéristique de relaxation τ des chaînes de polymères au sein du gel et un exposant m pour le module de perte. Changer le rapport de dissipation en changeant le substrat s'avère compliqué : il est difficile de faire varier ces trois paramètres indépendamment. Par souci de simplicité, nous avons changé $\mathbf{R}$ en utilisant des liquides de différentes viscosités. Le nombre $\mathbf{R}$ explore quatre ordres de grandeur.

Cette description conséquente de nos protocoles illustre bien tout le soin à apporter aux expériences pour contrôler nos systèmes et obtenir des résultats reproductibles.

11.3 Résultats

Quel que soit $\mathbf{R}$, la forme des gouttes dépend de leur vitesse de dévalement. À basse vitesse, la goutte reste quasiment axisymétrique. Elle s'allonge à plus haute vitesse, et se déstabilise au-delà d'une vitesse critique. La goutte laisse alors de petites gouttelettes derrière elle : c'est l'instabilité de perlage (Fig. 11.1).

Nos expériences, bien qu'incapables d'atteindre la limite $\mathbf{R} = 0$, montrent une analogie entre le cas rigide et le cas $\mathbf{R} \sim 1$. En particulier, nous trouvons une relation entre l'énergie injectée dans le système et la dissipation qui est proche de celle du cas rigide, et les formes des gouttes se comparent très bien, montrant même des gouttes en coin à l'approche de la transition de perlage (Fig. 11.1). Des différences substantielles avec le cas rigide apparaissent lorsque $\mathbf{R} \gg 1$. Les formes des gouttes restent plus arrondies jusqu'à la transition de perlage (Fig. 11.1), et la dissipation dans le solide régit la dynamique de la goutte.

Cependant, l'analyse de la dynamique à l'échelle de la ligne de contact montre que l'analogie entre le cas rigide et le cas mou à $\mathbf{R} \sim 1$ est en fait qualitative. La dissipation dans le solide joue encore un rôle important : le modèle de Cox-Voinov, qui donne la relation entre l'angle de contact dynamique et la vitesse de la goutte en tenant compte uniquement de la dissipation dans le liquide, ne fournit que des estimations douteuses pour la taille d'une molécule de liquide. L'analyse globale des données montre que le modèle que nous voulons tester est capable de très bien les décrire, sans aucun paramètre d'ajustement libre. Notre cadre théorique décrit la réponse élastique du matériau jusqu'à l'ordre 2 des déformations, et cela semble être un niveau de non-linéarité suffisant pour décrire les données. Le modèle peine cependant à capturer certains aspects de nos expériences, en particulier la branche de reculée de certains systèmes. Dans tous les cas, ces divergences résultent soit d'une propriété des liquides que nous utilisons et dont nous avons pris note *a posteriori*, comme une réponse de type savon, soit d'un mouvement oscillatoire inattendu de la ligne de contact dont l'origine reste à identifier.

Par ailleurs, nous documentons la transition de perlage de plusieurs systèmes d'élastomouillage. La ligne de contact dépose un film de liquide sur le substrat lorsque l'angle de contact dynamique de reculée atteint une valeur seuil, d'environ 30° pour la plupart de

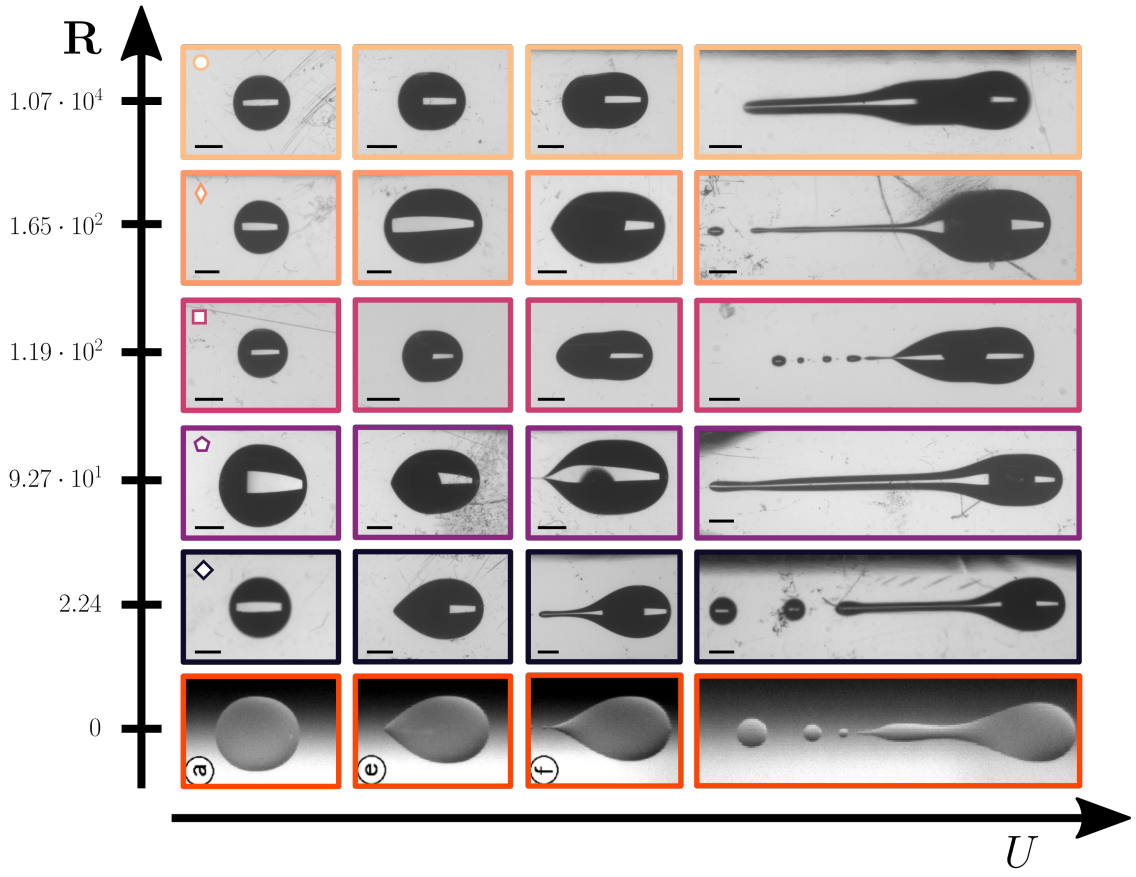

Figure 11.1: **Formes des gouttes dévalentes.** Plus la ligne est haute, plus la dissipation d'énergie dans le solide est importante par rapport à celle dans le liquide. La goutte dévale le substrat de plus en plus vite le long d'une ligne. La ligne du bas correspond au cas rigide (**R** = 0), c'est-à-dire à une goutte dévalant une plaque de verre (images reproduites à partir de [97]). Les formes à **R** = 2.24 sont comparables à celles du cas rigide. En revanche, les gouttes sont plus rondes et plus allongées à mesure que la dissipation dans le solide prends de l'importance. Barres d'échelle: 2 mm.

nos systèmes. Nous en dégageons les tendances suivantes : l'instabilité survient d'autant plus tôt que l'angle de contact d'équilibre est faible à rapport de dissipation **R** constant. Dans ce cas, cela réduit l'écart entre l'angle d'équilibre et l'angle critique. De la même manière, l'instabilité survient d'autant plus tôt que le rapport de dissipation est grand à angle d'équilibre constant. Dans ce cas, cela demande plus d'énergie d'atteindre une certaine vitesse, et l'angle dynamique correspondant est d'autant plus éloigné de sa valeur d'équilibre. Ainsi, on atteint la valeur seuil à des vitesses plus faibles dans ces deux cas.

Les gels que nous utilisons ont peu ou pas d'hystérése. De plus, ils contiennent des quantités importantes de chaînes libres qui sont censées lisser la surface des gels. Cependant, nous observons que la transition de perlage se produit à un nombre capillaire critique pour lequel l'angle de contact à l'arrière de la goutte ne disparaît pas, contrairement à ce qui était attendu. Un angle critique non nul a également été rapporté dans le cas d'un substrat rigide, et raisonnablement attribué à l'époque aux effets possibles de la rugosité et des défauts de la surface. Ces hypothèses sont difficiles à justifier ici. Par conséquent, bien que le nombre capillaire critique soit bien prédit par le modèle, l'observation d'un angle fini à la transition de perlage reste une énigme, et des travaux supplémentaires sont nécessaires pour espérer

comprendre ce phénomène.

En outre, la forme des gouttes proches de l'instabilité de perlage dépend du rapport de dissipation **R**. Alors que des coins apparaissent sur le contour des gouttes à de faibles valeurs de **R**, l'arrière des gouttes reste arrondi avec un rayon de courbure du même ordre de grandeur que le rayon de la goutte au repos dans le cas $\mathbf{R} \gg 1$. Par conséquent, la possibilité même de l'existence du coin dépend du rapport de dissipation.

Nous montrons aussi que la forme de la goutte dépend de la rigidité du substrat, à **R** constant. L'idée est de tester comment les propriétés de la ligne de contact, telles que ses capacités à former des coins, dépendent de la longueur élastocapillaire intrinsèque au solide. Cette quantité est une fonction décroissante du module de cisaillement du solide. Nos expériences préliminaires montrent que le rayon de courbure à l'arrière de la goutte diminue avec la diminution de la longueur élastocapillaire. Ces expériences sont encore loin d'être contrôlées, et un travail important reste à faire pour caractériser de manière approfondie nos observations.

11.4 Perspectives

Nous avons également étudié la dynamique des lignes de contact en reculée lorsque le gel est extrait d'un bain. Ces expériences de « dip-coating » montrent qu'il existe deux régimes séparés par une vitesse seuil. La ligne de contact reste à proximité de la surface du liquide tant que la vitesse d'extraction est inférieure au seuil d'entraînement. Un film est entraîné lorsque ce dernier est dépassé. Cependant, le mouvement de la ligne de contact n'est pas homogène. Les parties de la ligne de contact proches des bords de l'échantillon commencent à reculer par rapport au substrat pendant l'extraction : leur vitesse dans le référentiel du laboratoire est plus faible que celle de l'échantillon. Nous observons des formes qui diffèrent du cas du substrat rigide. Alors que le film devient trapézoïdal aux premiers stades de la récession, un rectangle est observé aux derniers stades. Ce rectangle est en fait la seule forme observée dans le cas $\mathbf{R} \sim 1$, un résultat surprenant puisque ce système est censé être le plus proche du cas rigide. Encore une fois, beaucoup de travail reste à faire, et certains aspects du film entraîné tels que son profil d'épaisseur et les angles de contact au niveau de la ligne de contact doivent être mesurés pour mieux comprendre ce problème. De plus, revenir au cas rigide avec les liquides que nous utilisons dans ces expériences pourrait également s'avérer instructif.

Outre ces perspectives à court terme, ce travail laisse entrevoir des perspectives intéressantes avec des systèmes différents. L'une de ces perspectives repose sur l'utilisation de surfaces imprégnées de liquide. On sait que les gouttes se déplaçant sur ces surfaces sont entourées d'une crête, de forme similaire à la crête élastocapillaire de nos systèmes. La présence de cette couche est connue pour rendre ces systèmes similaires aux dispositifs non mouillants. Le liquide qui imprègne la surface du solide, généralement dans un réseau de piliers microscopiques, peut dissiper de l'énergie. Notre modèle fait également des prédictions pour la dynamique des lignes de contact sur des liquides visqueux, et les systèmes imprégnés offrent une belle plateforme pour étudier les prédictions de notre modèle. Un point particulièrement intéressant serait d'étudier si les gouttes glissant sur de telles surfaces connaissent également une transition de perlage, et de mesurer les propriétés de la ligne de contact au seuil.

Une autre perspective serait de synthétiser des élastomères souples dont le réseau comporte peu ou pas de chaînes libres. Bien qu'il soit possible d'obtenir de tels matériaux en mélangeant des kits commerciaux dans des proportions éloignées des recommandations

du fabricant, ce processus prend beaucoup de temps, car les chaînes libres doivent être extraites par plusieurs bains de solvant, une opération qui prend au moins deux semaines. Les progrès récents dans la synthèse des polymères suggèrent que les réseaux souples presque exempts de chaînes libres peuvent être obtenus par réticulation de PDMS ramifié. Bien que cette perspective nécessite de maîtriser la chimie des polymères, nous pensons qu'il s'agit d'une direction intéressante à prendre, car elle aiderait la communauté à démêler l'origine des diverses observations faites au fil des ans en fonction de la présence de chaînes libres.

Bibliography

[1] "https://www.pinterest.com.au/pin/808607308074097256/."

[2] "https://www.biomimesis.fr/tag/effet-lotus/," 2013.

[3] N. A. Patankar, "Mimicking the lotus effect: influence of double roughness structures and slender pillars," *Langmuir*, vol. 20, no. 19, pp. 8209–8213, 2004.

[4] M. C. Reyssat, *Splendeur et misère de l'effet lotus*. PhD thesis, Université Pierre et Marie Curie-Paris VI, 2007.

[5] C. Page, "How aircraft deal with the dangers of snow and ice," 2019.

[6] "https://nettoyer-une-tache.ooreka.fr/astuce/voir/652341/tissu-deperlant."

[7] M. Sokuler, G. K. Auernhammer, M. Roth, C. Liu, E. Bonacurrso, and H.-J. Butt, "The softer the better: fast condensation on soft surfaces," *Langmuir*, vol. 26, no. 3, pp. 1544–1547, 2010.

[8] amàco / films du lierre, "https://www.youtube.com/watch?v=1manbrtsi58," Licence Creative Commons : BY + NC + ND.

[9] S. Andrieu and P. Müller, *Les Surfaces Solides: Concepts et Méthodes*. EDP Sciences, 2012.

[10] P.-G. De Gennes, F. Brochard-Wyart, D. Quéré, *et al.*, *Capillarity and wetting phenomena: drops, bubbles, pearls, waves*, vol. 336. Springer, 2004.

[11] R. D. Schulman, M. Trejo, T. Salez, E. Raphaël, and K. Dalnoki-Veress, "Surface energy of strained amorphous solids," *Nature communications*, vol. 9, no. 1, pp. 1–6, 2018.

[12] J. P. Mercier, G. Zambelli, and W. Kurz, "Thermodynamics - Atomic origin of elasticity," in *Introduction to Material Science*, p. 127, Paris: Elsevier, 2002.

[13] R. Shuttleworth, "The surface tension of solids," *Proceedings of the physical society. Section A*, vol. 63, no. 5, p. 444, 1950.

[14] K. McLoughlin, C. Szeto, T. Duncan, and C. Cohen, "End-linked poly (dimethylsiloxane) elastomer structure: 2h-nmr transverse dephasing data compared to predictions of statistical and thermodynamic models," *Macromolecules*, vol. 29, no. 16, pp. 5475–5483, 1996.

[15] J. S. Rowlinson and B. Widom, *Molecular theory of capillarity*. Courier Corporation, 2013.

[16] P.-G. De Gennes, F. Brochard-Wyart, and D. Quéré, *Capillarity and Wetting Phenomena - Drops, Bubbles, Pearls, Waves*. New York: Springer-Verlag, 1st ed., 2004.

[17] T. Young, "Iii. an essay on the cohesion of fluids," *Philosophical transactions of the royal society of London*, no. 95, pp. 65–87, 1805.

[18] A. Dupré and P. Dupré, *Théorie mécanique de la chaleur*. Gauthier-Villars, 1869.

[19] J. Joanny and P.-G. De Gennes, "A model for contact angle hysteresis," *The journal of chemical physics*, vol. 81, no. 1, pp. 552–562, 1984.

[20] J. J. Bikerman, *Contributions to the Thermodynamics of Surfaces*. The Author, 1961.

[21] J. Bikerman, "Surface energy of solids," *physica status solidi (b)*, vol. 10, no. 1, pp. 3–26, 1965.

[22] G. Lester, "Contact angles of liquids at deformable solid surfaces," *Journal of Colloid Science*, vol. 16, no. 4, pp. 315–326, 1961.

[23] G. Lester, "Contact angles of liquids on organic solids," *Nature*, vol. 209, no. 5028, pp. 1126–1127, 1966.

[24] L. Chen, E. Bonaccurso, T. Gambaryan-Roisman, V. Starov, N. Koursari, and Y. Zhao, "Static and dynamic wetting of soft substrates," *Current opinion in colloid & interface science*, vol. 36, pp. 46–57, 2018.

[25] C. Extrand and Y. Kumagai, "Contact angles and hysteresis on soft surfaces," *Journal of colloid and interface science*, vol. 184, no. 1, pp. 191–200, 1996.

[26] J. Andrade, R. King, D. Gregonis, and D. Coleman, "Surface characterization of poly (hydroxyethyl methacrylate) and related polymers. i. contact angle methods in water," in *Journal of polymer science: Polymer symposia*, vol. 66, pp. 313–336, Wiley Online Library, 1979.

[27] A. Carré, J.-C. Gastel, and M. E. Shanahan, "Viscoelastic effects in the spreading of liquids," *Nature*, vol. 379, no. 6564, pp. 432–434, 1996.

[28] M. Shanahan and P. De Gennes, "Equilibrium of the triple line solid/liquid/fluid of a sessile drop," in *Adhesion 11*, pp. 71–81, Springer, 1987.

[29] R. Pericet-Camara, G. K. Auernhammer, K. Koynov, S. Lorenzoni, R. Raiteri, and E. Bonaccurso, "Solid-supported thin elastomer films deformed by microdrops," *Soft Matter*, vol. 5, no. 19, pp. 3611–3617, 2009.

[30] S. J. Park, B. M. Weon, J. San Lee, J. Lee, J. Kim, and J. H. Je, "Visualization of asymmetric wetting ridges on soft solids with x-ray microscopy," *Nature communications*, vol. 5, no. 1, pp. 1–7, 2014.

[31] G. Pu and S. J. Severtson, "Characterization of dynamic stick-and-break wetting behavior for various liquids on the surface of a highly viscoelastic polymer," *Langmuir*, vol. 24, no. 9, pp. 4685–4692, 2008.

[32] G. Pu, J. Ai, and S. J. Severtson, "Drop behavior on a thermally-stripped acrylic polymer: influence of surface tension induced wetting ridge formation on retention and running," *Langmuir*, vol. 26, no. 15, pp. 12696–12702, 2010.

[33] G. Pu and S. J. Severtson, "Water evaporation on highly viscoelastic polymer surfaces," *Langmuir*, vol. 28, no. 26, pp. 10007–10014, 2012.

[34] Q. Xu, L. A. Wilen, K. E. Jensen, R. W. Style, and E. R. Dufresne, "Viscoelastic and poroelastic relaxations of soft solid surfaces," *Physical Review Letters*, vol. 125, no. 23, p. 238002, 2020.

[35] M. Zhao, F. Lequeux, T. Narita, M. Roché, L. Limat, and J. Dervaux, "Growth and relaxation of a ridge on a soft poroelastic substrate," *Soft matter*, vol. 14, no. 1, pp. 61–72, 2018.

[36] R. Pericet-Cámara, A. Best, H.-J. Butt, and E. Bonaccurso, "Effect of capillary pressure and surface tension on the deformation of elastic surfaces by sessile liquid microdrops: an experimental investigation," *Langmuir*, vol. 24, no. 19, pp. 10565–10568, 2008.

[37] R. W. Style, R. Boltyanskiy, Y. Che, J. Wettlaufer, L. A. Wilen, and E. R. Dufresne, "Universal deformation of soft substrates near a contact line and the direct measurement of solid surface stresses," *Physical review letters*, vol. 110, no. 6, p. 066103, 2013.

[38] G. H. Fredrickson, A. Ajdari, L. Leibler, and J. P. Carton, "Surface modes and deformation energy of a molten polymer brush," *Macromolecules*, vol. 25, no. 11, pp. 2882–2889, 1992.

[39] D. T. Wu, G. H. Fredrickson, J.-P. Carton, A. Ajdari, and L. Leibler, "Distribution of chain ends at the surface of a polymer melt: Compensation effects and surface tension," *Journal of Polymer Science Part B: Polymer Physics*, vol. 33, no. 17, pp. 2373–2389, 1995.

[40] D. Long, A. Ajdari, and L. Leibler, "Static and dynamic wetting properties of thin rubber films," *Langmuir*, vol. 12, no. 21, pp. 5221–5230, 1996.

[41] D. Long, A. Ajdari, and L. Leibler, "How do grafted polymer layers alter the dynamics of wetting?," *Langmuir*, vol. 12, no. 6, pp. 1675–1680, 1996.

[42] L. Limat, "Straight contact lines on a soft, incompressible solid," *The European Physical Journal E*, vol. 35, no. 12, pp. 1–13, 2012.

[43] M. Zhao, *Mouillage sur gels mous*. PhD thesis, Paris Sciences et Lettres (ComUE), 2017.

[44] M. Zhao, J. Dervaux, T. Narita, F. Lequeux, L. Limat, and M. Roché, "Geometrical control of dissipation during the spreading of liquids on soft solids," *Proceedings of the National Academy of Sciences*, vol. 115, no. 8, pp. 1748–1753, 2018.

[45] J. Dervaux and L. Limat, "Contact lines on soft solids with uniform surface tension: analytical solutions and double transition for increasing deformability," *Proceedings of the Royal Society A: Mathematical, Physical and Engineering Sciences*, vol. 471, no. 2176, p. 20140813, 2015.

[46] F. E. Neumann and A. Wangerin, *Vorlesung über die Theorie der Capillarität*. BG Teubner, 1894.

[47] R. W. Style and E. R. Dufresne, "Static wetting on deformable substrates, from liquids to soft solids," *Soft Matter*, vol. 8, no. 27, pp. 7177–7184, 2012.

[48] J. Dervaux and L. Limat, "Contact lines on soft solids with uniform surface tension : Analytical solutions and double transition for increasing deformability," *Proc. R. Soc. A*, vol. 471, p. 20140813, 2015.

[49] A. Pandey, B. Andreotti, S. Karpitschka, G. Van Zwieten, E. Van Brummelen, and J. Snoeijer, "Singular nature of the elastocapillary ridge," *Physical Review X*, vol. 10, no. 3, p. 031067, 2020.

[50] A. Marchand, S. Das, J. H. Snoeijer, and B. Andreotti, "Contact angles on a soft solid: From young's law to neumann's law," *Physical review letters*, vol. 109, no. 23, p. 236101, 2012.

[51] Q. Xu, K. E. Jensen, R. Boltyanskiy, R. Sarfati, R. W. Style, and E. R. Dufresne, "Direct measurement of strain-dependent solid surface stress," *Nature communications*, vol. 8, no. 1, pp. 1–6, 2017.

[52] K. E. Jensen, R. Sarfati, R. W. Style, R. Boltyanskiy, A. Chakrabarti, M. K. Chaudhury, and E. R. Dufresne, "Wetting and phase separation in soft adhesion," *Proceedings of the National Academy of Sciences*, vol. 112, no. 47, pp. 14490–14494, 2015.

[53] M. van Gorcum, B. Andreotti, J. H. Snoeijer, and S. Karpitschka, "Dynamic solid surface tension causes droplet pinning and depinning," *Physical review letters*, vol. 121, no. 20, p. 208003, 2018.

[54] M. Van Gorcum, S. Karpitschka, B. Andreotti, and J. Snoeijer, "Spreading on viscoelastic solids: are contact angles selected by neumann's law?," *Soft matter*, vol. 16, no. 5, pp. 1306–1322, 2020.

[55] M. E. R. Shanahan and P. G. de Gennes, "L'arête produite par un coin liquide près de la ligne triple de contact solide/liquide/fluide," *C. R. Acad. Sci. Paris*, vol. 302, pp. 517–521, 1986.

[56] N. Lapinski, Z. Liu, S. Yang, C.-Y. Hui, and A. Jagota, "A surface with stress, extensional elasticity, and bending stiffness," *Soft Matter*, vol. 15, pp. 3817–3827, May 2019.

[57] B. Nicolas, J. Anand, S.-M. Katrina, H. Stefanie, S. Robert, and D. Eric, "Surface tension and the strain-dependent topography of soft solids," *arXiv preprint arXiv:2104.10578*, 2021.

[58] H. Wu, Z. Liu, A. Jagota, and C.-Y. Hui, "Effect of large deformation and surface stiffening on the transmission of a line load on a neo-Hookean half space," *Soft Matter*, vol. 14, no. 10, pp. 1847–1855, 2018.

[59] R. Masurel, M. Roché, L. Limat, I. Ionescu, and J. Dervaux, "Elastocapillary ridge as a noninteger disclination," *Physical review letters*, vol. 122, no. 24, p. 248004, 2019.

[60] Z. Liu, K. E. Jensen, Q. Xu, R. W. Style, E. R. Dufresne, A. Jagota, and C.-Y. Hui, "Effects of strain-dependent surface stress on the adhesive contact of a rigid sphere to a compliant substrate," *Soft Matter*, vol. 15, pp. 2223–2231, Mar. 2019.

[61] X. Liu, J. Liu, S. Lin, and X. Zhao, "Hydrogel machines," *Materials Today*, Jan. 2020.

[62] J. Dervaux, M. Roché, and L. Limat, "Nonlinear theory of wetting on deformable substrates," *Soft Matter*, 2020.

[63] R. Ablett, "Xxv. an investigation of the angle of contact between paraffin wax and water," *The London, Edinburgh, and Dublin Philosophical Magazine and Journal of Science*, vol. 46, no. 272, pp. 244–256, 1923.

[64] D. Bonn, J. Eggers, J. Indekeu, J. Meunier, and E. Rolley, "Wetting and spreading," *Reviews of modern physics*, vol. 81, no. 2, p. 739, 2009.

[65] J. H. Snoeijer and B. Andreotti, "Moving contact lines: Scales, regimes, and dynamical transitions," *Annu. Rev. Fluid Mech.*, vol. 45, no. 1, pp. 269–292, 2013.

[66] C. Huh and L. E. Scriven, "Hydrodynamic model of steady movement of a solid/liquid/fluid contact line," *J. Colloid Interface Sci.*, vol. 35, no. 1, pp. 85–101, 1971.

[67] R. Cox, "The dynamics of the spreading of liquids on a solid surface. part 1. viscous flow," *Journal of Fluid Mechanics*, vol. 168, pp. 169–194, 1986.

[68] J. Eggers, "Hydrodynamic theory of forced dewetting," *Physical review letters*, vol. 93, no. 9, p. 094502, 2004.

[69] P.-G. De Gennes, "Wetting: statics and dynamics," *Reviews of modern physics*, vol. 57, no. 3, p. 827, 1985.

[70] T. D. Blake and K. J. Ruschak, "Wetting: static and dynamic contact lines," in *Liquid film coating*, pp. 63–97, Springer, 1997.

[71] N. Le Grand, A. Daerr, and L. Limat, "Shape and motion of drops sliding down an inclined plane," *Journal of Fluid Mechanics*, vol. 541, p. 293, 2005.

[72] O. Voinov, "Hydrodynamics of wetting," *Fluid dynamics*, vol. 11, no. 5, pp. 714–721, 1976.

[73] E. Rio, *Gouttes, Flaques et Arches sèches: des lignes de contact en présence d'un écoulement.* PhD thesis, Université Pierre et Marie Curie-Paris VI, 2005.

[74] N. Le Grand-Piteira, *Ruissellement avec effets de mouillage: Gouttes et Méandres sur un plan incliné.* PhD thesis, Université Paris-Diderot-Paris VII, 2006.

[75] R. Herbaut, *Dynamique des liquides sur substrat froid, avec solidification.* PhD thesis, Université Sorbonne Paris Cité, 2019.

[76] J. H. Snoeijer, "Free-surface flows with large slopes: Beyond lubrication theory," *Phys. Fluids*, vol. 18, p. 021701, Feb. 2006.

[77] E. Rio, A. Daerr, B. Andreotti, and L. Limat, "Boundary conditions in the vicinity of a dynamic contact line: experimental investigation of viscous drops sliding down an inclined plane," *Physical review letters*, vol. 94, no. 2, p. 024503, 2005.

[78] G. Delon, M. Fermigier, J. H. Snoeijer, and B. Andreotti, "Relaxation of a dewetting contact line. part 2. experiments," *Journal of Fluid Mechanics*, vol. 604, pp. 55–75, 2008.

[79] A. Carré and M. E. Shanahan, "Viscoelastic braking of a running drop," *Langmuir*, vol. 17, no. 10, pp. 2982–2985, 2001.

[80] M. Shanahan and A. Carré, "Viscoelasticity and kinetics of wetting on rubber," *The Journal of Adhesion*, vol. 57, no. 1-4, pp. 179–189, 1996.

[81] M. E. Shanahan and A. Carre, "Anomalous spreading of liquid drops on an elastomeric surface," *Langmuir*, vol. 10, no. 6, pp. 1647–1649, 1994.

[82] A. Carré and M. E. Shanahan, "Direct evidence for viscosity-independent spreading on a soft solid," *Langmuir*, vol. 11, no. 1, pp. 24–26, 1995.

[83] S. Karpitschka, S. Das, M. van Gorcum, H. Perrin, B. Andreotti, and J. H. Snoeijer, "Droplets move over viscoelastic substrates by surfing a ridge," *Nature communications*, vol. 6, no. 1, pp. 1–7, 2015.

[84] R. Chasset and P. Thirion, "Viscoelastic relaxation of rubber vulcanizates between the glass transition and equilibrium," *Rubber Chemistry and Technology*, vol. 39, no. 4, pp. 870–880, 1966.

[85] J. G. Curro and P. Pincus, "A theoretical basis for viscoelastic relaxation of elastomers in the long-time limit," *Macromolecules*, vol. 16, no. 4, pp. 559–562, 1983.

[86] S. Park, J. Bostwick, V. De Andrade, and J. Je, "Self-spreading of the wetting ridge during stick-slip on a viscoelastic surface," *Soft Matter*, vol. 13, no. 44, pp. 8331–8336, 2017.

[87] J. Gerber, T. Lendenmann, H. Eghlidi, T. M. Schutzius, and D. Poulikakos, "Wetting transitions in droplet drying on soft materials," *Nature communications*, vol. 10, no. 1, pp. 1–10, 2019.

[88] T. Kajiya, A. Daerr, T. Narita, L. Royon, F. Lequeux, and L. Limat, "Advancing liquid contact line on visco-elastic gel substrates: stick-slip vs. continuous motions," *Soft Matter*, vol. 9, no. 2, pp. 454–461, 2013.

[89] T. Kajiya, P. Brunet, L. Royon, A. Daerr, M. Receveur, and L. Limat, "A liquid contact line receding on a soft gel surface: dip-coating geometry investigation," *Soft Matter*, vol. 10, no. 44, pp. 8888–8895, 2014.

[90] S. Karpitschka, A. Pandey, L. A. Lubbers, J. H. Weijs, L. Botto, S. Das, B. Andreotti, and J. H. Snoeijer, "Liquid drops attract or repel by the inverted cheerios effect," *Proceedings of the National Academy of Sciences*, vol. 113, no. 27, pp. 7403–7407, 2016.

[91] R. Lhermerout, H. Perrin, E. Rolley, B. Andreotti, and K. Davitt, "A moving contact line as a rheometer for nanometric interfacial layers," *Nature communications*, vol. 7, no. 1, pp. 1–6, 2016.

[92] A. Hourlier-Fargette, A. Antkowiak, A. Chateauminois, and S. Neukirch, "Role of uncrosslinked chains in droplets dynamics on silicone elastomers," *Soft Matter*, vol. 13, no. 19, pp. 3484–3491, 2017.

[93] K. Smith-Mannschott, Q. Xu, S. Heyden, N. Bain, J. H. Snoeijer, E. R. Dufresne, and R. W. Style, "Droplets sit and slide anisotropically on soft, stretched substrates," *Physical Review Letters*, vol. 126, no. 15, p. 158004, 2021.

[94] R. W. Style, Y. Che, S. J. Park, B. M. Weon, J. H. Je, C. Hyland, G. K. German, M. P. Power, L. A. Wilen, J. S. Wettlaufer, *et al.*, "Patterning droplets with durotaxis," *Proceedings of the National Academy of Sciences*, vol. 110, no. 31, pp. 12541–12544, 2013.

[95] "https://www.freeimages.com/fr/photo/rain-drops-on-car-glass-1555448."

[96] T. Podgorski, *Ruissellement en conditions de mouillage partiel*. PhD thesis, Université Pierre et Marie Curie-Paris VI, 2000.

[97] T. Podgorski, J.-M. Flesselles, and L. Limat, "Corners, cusps, and pearls in running drops," *Physical review letters*, vol. 87, no. 3, p. 036102, 2001.

[98] I. Peters, J. H. Snoeijer, A. Daerr, and L. Limat, "Coexistence of two singularities in dewetting flows: Regularizing the corner tip," *Physical review letters*, vol. 103, no. 11, p. 114501, 2009.

[99] R. Lhermerout, *Mouillage de surfaces désordonnées à l'échelle nanométrique*. PhD thesis, PSL Research University, 2016.

[100] J. H. Snoeijer, E. Rio, N. Le Grand, and L. Limat, "Self-similar flow and contact line geometry at the rear of cornered drops," *Physics of Fluids*, vol. 17, no. 7, p. 072101, 2005.

[101] T. D. Blake and K. J. Ruschak, "A maximum speed of wetting," *Nature*, vol. 282, no. 5738, pp. 489–491, 1979.

[102] I. Peters, "Drops sliding down an inclined plane," Master's thesis, University of Twente, 2007.

[103] G. K. Seevaratnam, L. M. Walker, E. Ramé, and S. Garoff, "Wetting by simple room-temperature polymer melts: Deviations from Newtonian behavior," *Journal of Colloid and Interface Science*, vol. 284, pp. 265–270, Apr. 2005.

[104] J. D. Ferry, *Viscoelastic properties of polymers*. John Wiley & Sons, 1980.

[105] P.-G. De Gennes and P.-G. Gennes, *Scaling concepts in polymer physics*. Cornell university press, 1979.

[106] A. Rudin and P. Choi, *The elements of polymer science and engineering*. Academic press, 2012.

[107] M. Rubinstein, R. H. Colby, *et al.*, *Polymer physics*, vol. 23. Oxford university press New York, 2003.

[108] F. Luo, T. L. Sun, T. Nakajima, T. Kurokawa, Y. Zhao, K. Sato, A. B. Ihsan, X. Li, H. Guo, and J. P. Gong, "Oppositely charged polyelectrolytes form tough, self-healing, and rebuildable hydrogels," *Advanced materials*, vol. 27, no. 17, pp. 2722–2727, 2015.

[109] J. P. Gong, Y. Katsuyama, T. Kurokawa, and Y. Osada, "Double-network hydrogels with extremely high mechanical strength," *Advanced materials*, vol. 15, no. 14, pp. 1155–1158, 2003.

[110] H. Fan and J. P. Gong, "Fabrication of bioinspired hydrogels: challenges and opportunities," *Macromolecules*, vol. 53, no. 8, pp. 2769–2782, 2020.

[111] R. W. Style, R. Boltyanskiy, B. Allen, K. E. Jensen, H. P. Foote, J. S. Wettlaufer, and E. R. Dufresne, "Stiffening solids with liquid inclusions," *Nature Physics*, vol. 11, no. 1, pp. 82–87, 2015.

[112] L. R. G. Treloar, "The physics of rubber elasticity," 1975.

[113] P. Mazurek, S. Vudayagiri, and A. L. Skov, "How to tailor flexible silicone elastomers with mechanical integrity: a tutorial review," *Chemical Society Reviews*, vol. 48, no. 6, pp. 1448–1464, 2019.

[114] Y. Hu and Z. Suo, "Viscoelasticity and poroelasticity in elastomeric gels," *Acta Mech. Solida Sin.*, vol. 25, no. 5, pp. 441–458, 2012.

[115] T. D. C. Company, "SYLGARD 527 Silicone Dielectric Gel," no. 11, p. 3, 2017.

[116] G. Company, "Reactive_silicones - Gelest, Inc.," 2016.

[117] G. C. Lisensky, D. J. Campbell, K. J. Beckman, C. E. Calderon, P. W. Doolan, R. M. Ottosen, and A. B. Ellis, "Replication and compression of surface structures with polydimethylsiloxane elastomer," *Journal of Chemical Education*, vol. 76, no. 4, p. 537, 1999.

[118] P. Cancouët, S. Pernin, G. Hélary, and G. Sauvet, "Functional polysiloxanes. ii. neighboring effect in the hydrosilylation of poly (hydrogenmethylsiloxane-co-dimethylsiloxane) s by allylglycidylether," *Journal of Polymer Science Part A: Polymer Chemistry*, vol. 38, no. 5, pp. 837–845, 2000.

[119] L.-H. Cai, T. E. Kodger, R. E. Guerra, A. F. Pegoraro, M. Rubinstein, and D. A. Weitz, "Soft Poly(dimethylsiloxane) Elastomers from Architecture-Driven Entanglement Free Design," *Adv. Mater.*, vol. 27, no. 35, pp. 5132–5140, 2015.

[120] K. Takamura, H. Fischer, and N. R. Morrow, "Physical properties of aqueous glycerol solutions," *Journal of Petroleum Science and Engineering*, vol. 98, pp. 50–60, 2012.

[121] D. Company, "UCON lubricant datasheet."

[122] S.-A. Company, "Peg-ran-ppg datasheet."

[123] A. Daerr and A. Mogne, "Pendent_drop: an imagej plugin to measure the surface tension from an image of a pendent drop," *Journal of Open Research Software*, vol. 4, no. 1, 2016.

[124] J. Juuza, "Surface tension measurements of viscous materials by pendant drop method: Time needed to establish equilibrium shape," in *Macromolecular Symposia*, vol. 384, p. 1800150, Wiley Online Library, 2019.

[125] J. Château, É. Guazzelli, and H. Lhuissier, "Pinch-off of a viscous suspension thread," *Journal of Fluid Mechanics*, vol. 852, pp. 178–198, 2018.

[126] A. Hourlier-Fargette, J. Dervaux, A. Antkowiak, and S. Neukirch, "Extraction of silicone uncrosslinked chains at air–water–polydimethylsiloxane triple lines," *Langmuir*, vol. 34, no. 41, pp. 12244–12250, 2018.

[127] J. Schindelin, I. Arganda-Carreras, E. Frise, V. Kaynig, M. Longair, T. Pietzsch, S. Preibisch, C. Rueden, S. Saalfeld, B. Schmid, J. Y. Tinevez, D. J. White, V. Hartenstein, K. Eliceiri, P. Tomancak, and A. Cardona, "Fiji: An open-source platform for biological-image analysis," *Nat. Methods*, vol. 9, no. 7, pp. 676–682, 2012.

[128] O. Burri, 2017.

[129] M. J. Owen and P. J. Smith, "Plasma treatment of polydimethylsiloxane," *Journal of adhesion science and technology*, vol. 8, no. 10, pp. 1063–1075, 1994.

[130] K. Efimenko, W. E. Wallace, and J. Genzer, "Surface modification of sylgard-184 poly (dimethyl siloxane) networks by ultraviolet and ultraviolet/ozone treatment," *Journal of colloid and interface science*, vol. 254, no. 2, pp. 306–315, 2002.

[131] F. Zheng, C. He, P. Fang, J. Wang, B. Xiong, K. Wang, F. Liu, X. Peng, X. Xu, Z. Xu, *et al.*, "The surface structure of uv exposed poly-dimethylsiloxane (pdms) insulator studied by slow positron beam," *Applied surface science*, vol. 283, pp. 327–331, 2013.

[132] A. Hourlier-Fargette, *Soft interfaces: from elastocapillary snap-through to droplet dynamics on elastomers*. PhD thesis, Paris 6, 2017.

[133] B. A. Puthenveettil, V. K. Senthilkumar, and E. Hopfinger, "Motion of drops on inclined surfaces in the inertial regime," *Journal of Fluid Mechanics*, vol. 726, pp. 26–61, 2013.

[134] D. Company, "UCON lubricant safety datasheet," 2017.

[135] H. Matsuura and T. Miyazawa, "Intrachain force field and normal vibrations of polyethylene glycol," *Bulletin of the Chemical Society of Japan*, vol. 41, no. 8, pp. 1798–1808, 1968.

[136] H. Leonhard, "Experiments on tipstreaming." 1996.

[137] J. Eggers, "Nonlinear dynamics and breakup of free-surface flows," *Reviews of modern physics*, vol. 69, no. 3, p. 865, 1997.

[138] C. D. Eggleton, T.-M. Tsai, and K. J. Stebe, "Tip streaming from a drop in the presence of surfactants," *Physical review letters*, vol. 87, no. 4, p. 048302, 2001.

[139] J. M. Montanero and A. M. Ganán-Calvo, "Dripping, jetting and tip streaming," *Reports on Progress in Physics*, vol. 83, no. 9, p. 097001, 2020.

[140] V. G. Levich and V. S. Krylov, "Surface-tension-driven phenomena," *Ann. Rev. Fluid Mech.*, vol. 1, pp. 293–316, 1969.

[141] W. S. Y. Wong, L. Hauer, A. Naga, A. Kaltbeitzel, P. Baumli, R. Berger, M. d'Acunzi, D. Vollmer, and H.-J. Butt, "Adaptive Wetting of Polydimethylsiloxane," *Langmuir*, June 2020.

[142] A. Belmonte, "Self-oscillations of a cusped bubble rising through a micellar solution," *Rheologica Acta*, vol. 39, pp. 554–559, Nov. 2000.

[143] L. Landau and B. Levich, "Dragging of a Liquid by a Moving Plate," in *Dynamics of Curved Fronts*, pp. 141–153, 1988.

[144] J. H. Snoeijer, G. Delon, M. Fermigier, and B. Andreotti, "Avoided critical behavior in dynamically forced wetting," *Physical review letters*, vol. 96, no. 17, p. 174504, 2006.